Padova University, Padova, Italy

Department of Information Engineering

Ph.D. School in Information Engineering

Section: *Bioengineering* - Cycle: *XXXI*

The simultaneous PET/MRI to investigate the role of glucose metabolic consumption on brain functional architecture

Headmaster of the school: Prof. Andrea Neviani

Coordinator: Prof. Giovanni Sparacino

Supervisor: Prof. Alessandra Bertoldo

PhD candidate: Alessandro Palombit

To Alice

The simultaneous PET/MRI to investigate the role of glucose metabolic consumption on brain functional architecture

ABSTRACT

The human brain performances and computational potential relies on an intricate structure designed to share information between specialised areas. This exchange is thought to be either locally and globally optimized for best performances under the constraints posed by the physical communication structure and available energy.

Borrowing concepts from the machine learning literature, these principles can be reframed considering the brain as a mixture of cost functions, dynamically optimised lifelong but flawed in pathology.
At least one of these cost functions, needs to describe the energy balance of the brain, locally adapted to sustain specific functions but overall shaping the entire brain functional connectivity (FC) organisation to satisfy unknown energy consumption constraints.

In this thesis we investigate in-vivo the association defined by this energy-based cost function. In particular, the brain's connectivity structure will be assessed together with the glucose metabolism to understand which network topological features are metabolically supported using experimental approaches based on functional Magnetic Resonance Imaging (fMRI) and Positron Emission Tomography (PET).

We then assessed the feasibility of state-of-the-art fMRI methods evaluating their impact over single-subject FC. Particular emphasis was de-

voted to the role of noise in different experimental conditions affecting the experimental repeatability of FC measures.

A novel structural imaging approach based on Magnetic Resonance Fingerprint (MRF) combined with synthetic MRI is finally proposed to overcome current brain cortex delineation limitations in motion-prone settings to offer a better support for subsequent FC analyses.

The contributions presented in this dissertation encourage the application of single-subject FC measures providing consistent and eventually biologically supported network features enabling a more confident clinical usage when in tandem to the metabolism.

Misurazione simultanea PET/MRI per investigare il ruolo del metabolismo del glucosio sull'architettura funzionale del cervello

SOMMARIO

Le prestazioni del cervello umano ed il suo potenziale computazionale dipendono da una complessa struttura di comunicazione ottimizzata per condividere informazioni tra aree funzionalmente specializzate.
Tale struttura si ritiene essere sia localmente che globalmente ottimizzata per garantire massime prestazioni considerati i vincoli di efficienza ed energetici associati all'infrastruttura.

Considerando il problema computazionale e di comunicazione sia risolto tramite l'ottimizzazione di un insieme di funzioni di costo, adattate dinamicamente durante tutta l'esistenza dell'individuo, offre un sistema tanto flessibile quanto fragile rispetto a condizioni patologiche.
Almeno una di queste funzioni di costo dovra descrivere il bilancio energetico cerebrale. Ovvero descrivere in modo esplicito quali proprieta della rete vanno ottimizzate al contempo minimizzando il consumo energetico necessario.

In questa tesi viene investigata in-vivo l'associazione inferita da questa funzione di costo. In particolare verra studiato quali proprieta topologiche della struttura di connettivita sono supportate dal metabolismo del glucosio mediante un approccio sperimentale basato su risonanza magnetica funzionale (fMRI) e tomografia ad emissione di positroni (PET).

A seguire e' stata valutata la fattibilita' di tecniche fMRI allo stato nell'arte

ponendo particolare attenzione all'effetto di diverse variabili sperimentali sulla consistenza delle strutture di rete identificate a livello di singolo soggetto in base alle diverse condizioni di rumore introdotte.

Viene infine proposto un'approccio di acquisizione ed elaborazione di immagini strutturali basato su Magnetic Resonance Fingerprint (MRF) ed MRI sintetica atta a superare i limiti di delineazione della corteccia cerebrale causati dal movimento con il fine ultimo di migliorare il supporto strutturale sul quale sono svolte le successive analisi funzionali.

Il contributo di questa tesi e' volto ad individuare metodiche fMRI a singolo soggetto che forniscano misure ripetibili e consistenti della struttura di connettivita cerebrale di ogni soggetto ponendo le basi per una confidente applicazione clinica della metodologia, in particolare qualora considerata assieme a misure del metabolismo del glucosio cerebrale.

Contents

Any sufficiently advanced technology is indistinguishable from magic.

Arthur C. Clarke

1 Introduction and Motivation

According to a natural selection principle, the survival of any biological organism depends upon a tight performance-cost trade-off which delineate the ability and flexibility of different species within their natural environment. Even accounting for some adaptability during its life cycle, the general performances of each organism are archetypally defined by a single controller organ: the brain.

The human brain is a complex structure enclosed within the skull bone and meninges made up of many billions of specialized cells, called respectively neurons or glial supporting cells. These cells are so well organized and stereotypically related to the underlying vasculature, to deserve a specific designation that describes single processing components, the neuro vascular unit (McConnell et al., 2017).

Neurons are inter-connected by thousands of links (referred as synapses), responsible not only for an important information integration mechanism but also for the actual information exchange, whose strength is dynamically modulated to support higher level functions such as the adaptation or memory.

This modulation mechanism can provide strong connections when a tight coupling is needed between the activity of inter-connected neurons as well as links several orders of magnitude weaker, entailing a non-sparse communication structure at microscopic level (Panzeri et al., 2015).
However, its challenging to explain the functional role of such a broad spectrum of connection strengths at this low spatial scale in support of higher level cognitive functions.

Availing of appropriate experimental approaches, in the last 20 years neuroscientists shifted to higher level assessments. They noticed a tendency of brain neurons to cluster together when its functionally convenient. Therefore, from a functional perspective they were able to divide the whole brain in functionally discrete areas, characterized by a common functional role as well as similar cellular structural architecture, structure, etc. At the highest spatial level, clusters of neurons contained within the brain cortex (the outermost layer of the brain), were then subdivided in discrete areas or lobes, each credited for a specific function as thinking, voluntary actions or the processing of external stimuli.
The communication among such high level cortical structures (or areas) was found to be mediated by direct or indirect connections whose biological significance is still unclear regarding an information exchange or integration perspective. A central role in this perspective is offered by basal ganglia, a cluster of structures strategically positioned at the brain's center thought to mostly mediate the information exchange among multiple distal brain areas (Hwang et al., 2017).

This information exchange needs to be carried out quickly and with minimal resource requirements to guarantee the brains control capabilities and support high level cognitive functions. A failure of this communication system results in a loss of functionality that affects the whole organism as well as higher cognitive functions. Some examples of psychiatric and non-psychiatric conditions recently associated with altered brain connectivity from healthy subjects includes Epilepsy (Chiang et al., 2015), Stroke (Tsai et al., 2014), Alzheimers disease (Grothe et al., 2017) and Schizophenia (Sheffield and Barch, 2016).

The current view of the brain as a communication system arose almost 40 years ago with the seminal work of Legendy (Legéndy, 1975) which opened a research field per se denoted as brain connectivity specifically devoted to the study of the topological structure of the brain seen as a set of interconnected and functionally homogenous areas. Still, the experimental method used to determine whether different brain areas are connected or not is critical. A variety of approaches were proposed based on the association principle considered, from the electrical (e.g. electroencephalography, EEG or magnetic (e.g. magneto-encephalography, MEG (Hämäläinen and Ilmoniemi, 1994)) activity to the local metabolism with imaging tools as Magnetic Resonance Imaging (MRI) (Fox et al., 2005) or Positron Emission Tomography (PET) (Friston et al., 1996).

MRI can non-invasively represent soft tissues with high spatial resolution by delivering images with flexible contrast, ultimately dependent upon the magnetic properties of the imaged object. This tool allowed to simultaneously study the brains anatomical structure as well as many physiological functions such as its blood flow and metabolic supply. The popularity of MRI for neuroscience application stems from its capability of providing images sensitive to the local blood oxygenation level (BOLD (Ogawa et al., 1990)) by means of dedicated experiments referred as functional MRI measures (fMRI).

The underlying principle of fMRI depends upon the tight neuro-vascular coupling previously introduced: the local neural activity yields measurable hemodynamic variations (by means of temporally unstable blood oxygenation), ultimately making fMRI a relatively inexpensive and non-invasive indirect neural activity biomarker (Logothetis et al., 2001).

While physicists exploit the spatio-temporal correlations in MRI to accelerate the experimental data collection (see Chapter 2), neuroscientists make use of series of brain MRI images based on BOLD contrast to non-invasively monitor the temporal evolution of neural activity in a spatially resolved fashion (Logothetis et al., 2001). This activity was found to be spatially consistent to the structure of neuronal networks without the application of explicit stimuli (spontaneous neural activity), hinting to a

flexible brain organization with, however, a common organization basis.

Seminal approaches for connectivity were tightly dependent upon the specific experimental approach used and suffered from an unclear interpretation framework. Recent connectivity definitions are instead based on the co-activation between hemodynamic activity profiles in different brain areas. This led to the concept of functional connectivity (Friston et al., 1996) as statistically significant relationship between brain dynamics across different areas.

Generalizing the idea of functional connectivity to the whole brain level to offer a more comprehensive explanation of brain pathology or psychiatric phenomena, the study of the brain connectivity was then reframed as the problem of accurately mapping its functional networks (Smith et al., 2011) and use powerful formal tools to provide clearer interpretations (e.g. with graph modelling techniques).
As detailed in Chapter 3, such mapping process requires a criteria to define discrete functional areas (or nodes) and a metric that measures their activity similarity or eventually the information directionality. The aim of such association is to attribute a connectivity strength to all network links, generalizing the cellular network (whose connectivity is synaptically-mediated) idea exposed in this Chapter to a general functional network.

However, any of the previously described communication mechanism needs to be biologically supported. Brains communication structure is subject from the cellular level up, to the biological constraints of having a structural communication support (e.g. axons) which needs to be maintained and fueled. Brains energy consumption relies upon very efficient metabolic processes requiring adequate supply of glucose and oxygen delivered by the vasculature, needed to run synapses or for housekeeping. These processes can be characterized by monitoring the usage of molecular glucose, for example by means of PET that also enabled in-vivo monitoring of other functional processes such as neuroreceptor binding, protein deposition, etc. (Vlassenko and Mintun, 2012).

The amount of molecular energy required to keep the running connections active is disproportionately high as compared to housekeeping

functions and most of this energy is not spent to support the processing of external information, rather to sustain the connectivity among cortical neurons, reported as intrinsic synaptic activity.

This view was experimentally validated finding that the additional energy required by the brain to answer to external stimuli is extremely small compared to the ongoing energy requirements (Raichle, 2006), highlighting that the intrinsic communication activity accounts for most of the brain energy budget.

Based on an cost principle, Bullmore et al., (Bullmore and Sporns, 2012) offered a clearer perspective on the brains functional connectivity structure, suggesting that the actual network organization could be dynamically adapted to minimize material and metabolic costs while providing favorable topological properties (i.e. maintaining a high-performance communication system). Estimated brain networks were found to have high topological efficiency and organized in well-defined modules (Meunier et al., 2010) whose connectivity efficiency is further enhanced by a backbone of central network areas, strategically positioned for example to cut the topological distance among network nodes or maintain the connectivity among different modules (connector hubs). According to the authors, adapted topological patterns are governing the functional connectivity hierarchical structure but to date, no clear experimental demonstration is explicitly corroborating the idea.

Another cost perspective was offered by Marblestone et al., (Marblestone et al., 2016), integrating ideas borrowed from machine learning literature of artificial neural networks. Considering the brain communication structure as a computational system, its performances could be described by a set of dynamically optimized cost functions in the machine learning sense. These functions are distinct across brain areas and could be shaped as well by the development or by learning processes which correspond to the cost optimization. With their work, these authors provided an interpretation framework where the connectivity among distal areas is formulated as an optimization problem. This optimization adapts pre-defined network architectures (e.g. templates) to solve different com-

putational problems posing additional constraints. As an example, such constraints could be based on the energetic cost of such an optimal network therefore the energetic demand acts like the regularization term in a traditional optimization problem.

Taken together, these ideas formally support the relation between energy metabolism and topological features of the brains network connectivity. However, there is limited literature about the experimental method to use for functional connectivity evaluation neither strong and biologically-supported evidence toward specific network structures. This knowledge limitation considered within the exposed energetic framework makes the energy metabolism a perfect candidate to shed light on biologically plausible architecture or discard unlikely network features that lacks a biologically accepted interpretation.

Centering this introduction on the brain connectivity using fMRI and energy metabolism using PET, there is consistent evidence toward the benefits of collecting both types of data not only from the same subjects but possibly also simultaneously. In fact, often the connectivity measures as well as brains metabolism is characterized at group level for example averaging the connectivity structure of many subjects resulting in a lower sensitivity to the underlying network organization or similarly to subjective metabolic features which could be indicative of individual network organizations.

While extensive evidence is available that describes the functional communication to energy metabolism relation at microscopic (cellular level) and meso-scale, limited evidence is available for such a relation between the intrinsic connectivity and energy metabolism at macroscopic scale. Even less applications can be found to make use of these ideas in neuropathology, where only Scherr et al., (Scherr et al., 2018) explicitly studied together the metabolic and connectivity impairments of Alzheimer's disease patients.

Nonetheless, the combination of functional connectivity with energy metabolism has the potential to enable more concrete brain network fea-

ture discovery motivating more focused modelling efforts as from multimodal brain connectivity descriptions. The aim of this thesis is to study whether brain network organizational can be associated to the underlying energy metabolism. Experimental limitations encountered will demand for the investigation of the impact of different experimental variables on the estimated brains organization to promote consistent usage of state-of-the-art fMRI tools for FC in hybrid PET/MRI scanners. Moreover, current limitations encountered in structural MRI will be tackled by developing a novel structural imaging framework that enforce on the comparability potential of quantitative MRI and the flexibility of synthetic MRI within a generalized framework to minimized the manual interventions and scanner protocol tuning needs.

1.1 Thesis Contributions and Outline

- **Chapter 1** (current Chapter) provides an introductory overview and motivation for the studies described in this dissertation.

- **Chapter 2** introduces the fundamental principles of MRI and its application for relaxometry and fMRI. The fundamental principles of PET imaging were also delineated concluding with a description of hybrid scanners for simultaneous PET/MRI applications.

- **Chapter 3** presents a description of fMRI-based functional connectivity, modelling approaches and graphical methods to investigate network structures. Functional connectivity confounds and experimental approach will be discussed highlighting the limitations for single subject estimates. Am overview of brain glucose metabolism will be given describing its experimental assessment with PET and discussing current results obtained combining functional connectivity to glucose metabolism.

- **Chapter 4** studied the relation between brain network architecture and energy metabolism in resting state condition. Relevant brain topological features, derived from fMRI data, were regionally associated to the glucose metabolism described by PET using literature-available data to evaluate whether structural network features are biologically supported at macroscopic level with graph theory methods. The purpose and contribution of this chapter is to demonstrate the existence of a link between connectivity structure as identified in resting state condition to the underlying glucose metabolism, that is not clearly determined over all brain areas while becomes significant over central brain network nodes that regulate the brain communication performances. The implemented analysis will also be discussed to highlight current methodological limitations motivating the experimental improvements described in subsequent Chapters 5 and 6.

- **Chapter 5** builds upon the experimental limitations of functional connectivity encountered to study both theoretically and experimentally the reliability of single subject functional connectivity measures during a protocol optimization task, loosely aimed at delivering state-of-the-art functional connectivity protocols for PET/MRI scanners. The purpose and contribution of this chapter was to demonstrate the sensitivity of functional connectivity measures to the experimental covariate provided by the fMRI imaging sequence both from a signal to noise and actual functional connectivity structure perspective and also evaluate whether these parameters actually impact the topological structure estimated over single subjects.

- **Chapter 6** presents a novel framework for robust brain cortical segmentation using quantitative MRI (qMRI) based on Magnetic Reso-

nance Fingerprint (MRF) approaches combined with synthetic MRI (synMRI) for arbitrary contrast generation. Current structural imaging approaches collect one (or more) high resolution images subsequently processed to segment the brain cortex, used as structural support for functional connectivity analysis. The idea was to perform qMRI instead of collecting single-contrast images and rely on synMRI to generate contrasts simpler to segment, less motion prone within a flexible modular framework structure. We focused on MRF for T1 estimation to synthesize standard T1-w images and T2* as additional source of contrast useful to disentangle brain and meninges, often source of segmentation errors to be manually corrected for accurate FC analysis. The framework is proposed along with preliminary results regarding the MRF sequence implementation and encountered limitations.

- **Chapter 7** summarizes the dissertation contributions discussing the perspectives of studied topics.

2
Background

2.1 Principles of Magnetic Resonance Imaging

Magnetic Resonance Imaging (MRI) entitle an imaging modality based on the experimental manipulation and observation of the behaviour of particles in a magnetic field, specifically referred in the case of atom nuclei elements as Nuclear Magnetic Resonance (NMR). NMR was first investigated in 1946 by Bloch (Bloch et al., 1946) and Purcell (Purcell et al., 1946), awarded with The Nobel prize for physics in 1952. NMR techniques naturally evolved to MRI with the introduction of spatial encoding introduced by Lauterbur (Lauterbur, 1973) and Mansfield (Mansfield and Grannell, 1973), as well awarded with The Nobel prize for Medicine in 2003 as recognition for this in-vivo and non-invasive technique imaging modality of soft tissues created.

2.1.1 Spin properties and NMR experiment

The physical phenomenon which underlies NMR and MRI is based on the dynamic interaction between nuclear spins subjected to an externally applied magnetic field. A pool of spins at the thermal equilibrium in such a magnetic field can be then perturbed by a radiofrequency (RF) pulse, specifically designed to drive the spin pool dynamic in order to potentially generate measurable responses (Haacke et al., 1999).

At the thermal equilibrium, the spin populations are unbalanced, resulting in a macroscopic magnetization M_0 coherent with the external B_0. Such magnetization can be described as a vector in a reference system fixed with the laboratory or moving with same angular frequency of the spins (precession at *Larmor* frequency) as: $M_0 = (M_x, M_y, M_z)$.

Within a general B_0, **M** is not necessarily parallel to B_0, but can also contain transversal components of magnetization equivalently represented as:

$$\begin{aligned} M_{\parallel} &= M_z \\ M_{\perp} &= M_x + i \cdot M_y \end{aligned} \tag{2.1}$$

2.2 Radio Frequency pulses

The macroscopic static component of the magnetisation M_0 from a pool of spin isochromats to be investigated needs to be able to generate measurable signals. One way to detect magnetization evolution is making use of *NMR* phenomena. Superimposing a magnetic field B_1 generally referred as radiofrequency (RF) pulse, having at least one component orthogonal to B_0, the spin evolution can be altered to precess around the $B_t = B_0 + B_1$ field with same angular frequency. If B_1 field is also played at Larmor frequency (γ) of the nuclei of interest, only the spins of interest are forced to also precess coherently in phase, building a net magnetization component in the transverse plane. As the B_1 pulse is generated in the transversal B_0 plane, only two components are needed to completely

identify its dynamic as:

$$\mathbf{B(t)_1} \;=\; \mathbf{B_{1,t}} e^{j\omega_{RF} t} \;=\; (B^+_{1,x}, B^+_{1,y}) \tag{2.2}$$

Formally, the precession motion can be described, in steady state and no relaxation involved, as due to the off-resonance contributors (ΔB_0, zero in case of the exactly prescribed B_0) and the RF field B_1^+ (decomposed in $B^+_{1,x}, B^+_{1,y}$):

$$\frac{d}{dt} \cdot \begin{pmatrix} m_x \\ m_y \\ m_z \end{pmatrix} = \gamma \begin{pmatrix} 0 & \Delta B_0 & -B^+_{1,y} \\ -\Delta B_0 & 0 & B^+_{1,x} \\ B^+_{1,y} & -B^+_{1,x} & 0 \end{pmatrix} \cdot \begin{pmatrix} m_x \\ m_y \\ m_z \end{pmatrix} \tag{2.3}$$

let us to model in the time domain the evolution of a single magnetisation element (*isocromat*) and, based on the magnetisation behaviour reported in the following, tailor RF pulse to emphasize or suppress specific features of the sample.

Once a transversal magnetisation component is defined, contributions from each spatial location will process coherently in phase in the transversal plane, inducing a measurable current in appropriate RF receive coil elements (e.g. loop coils). After the application of a pulse of finite duration (*tp*), the relative angle (flip angle, α) between B_0 and M can be evaluated based on B_1 profile as:

$$\alpha \;=\; \gamma B(\tau)_1 \cdot d\tau \;=\; \gamma B_1 \cdot tp \tag{2.4}$$

In practice, the flip angle associated with an RF pulse is spatially dependent based on the features of both the pulse and investigated sample. As a consequence, applications where precise flip angle is needed request additional effort in ensuring an appropriate pulse usage or external measurement of the effective flip angle amplitude for correction purposes as requested in quantitative MRI.

2.3 MAGNETIC RESONANCE SIGNAL

The dynamics of the macroscopic magnetization M originating from an ensemble of spin isochromats under and after an RF pulse application can be described by the *Bloch* equations (Bloch et al., 1946). In a rotating frame at *Larmor* frequency respect to the fixed (laboratory) reference, the *Bloch* equations take the form:

$$\frac{d}{dt} \cdot \begin{pmatrix} m_x \\ m_y \\ m_z \end{pmatrix} = \begin{pmatrix} -\frac{1}{T_2} & \gamma \Delta B_0 & -\gamma B_{1,y}^{+} \\ -\gamma \Delta B_0 & -\frac{1}{T_2} & \gamma B_{1,x}^{+} \\ \gamma B_{1,y}^{+} & -\gamma B_{1,x}^{+} & -\frac{1}{T_1} \end{pmatrix} \cdot \begin{pmatrix} m_x \\ m_y \\ m_z \end{pmatrix} + \begin{pmatrix} 0 \\ 0 \\ \frac{m_0}{T_1} \end{pmatrix} \tag{2.5}$$

with ΔB_0 the off-resonance field, T_1 the longitudinal relaxation rate, T_2 transverse relaxation rate, M_0 the equilibrium magnetization and $B_{1,x}$, $B_{1,y}$ referring to the RF components respectively along x- or y-axis of the rotating frame. From *Bloch* equations, two fundamental mechanisms govern magnetization evolution.

The longitudinal relaxation (T_1 $[s]$) is related to the spin-lattice interaction consisting of energy exchange between spins and its chemical surroundings (lattice) that describes the recovery of the longitudinal magnetization component toward the thermal equilibrium. The transversal relaxation process (T_2 $[s]$) accounts for spin-spin interaction phenomena consisting of energy exchange between spins which ultimately introduces phase incoherence and describes the decay of transversal magnetization component.

The signal measured during an NMR experiment after repeated application of tailored RF pulses, termed *free induction decay* (FID), can be modelled adding on top of reversible T_2 relaxation phenomena for transversal magnetization, all irreversible transverse coherence loss as T_2^* relaxation time:

$$\frac{1}{T_2^*} = \frac{1}{T_2} + \frac{1}{T_2'} \tag{2.6}$$

where the effect of additional relaxation due to local field inhomogeneities (departures from B_0 existant in the imaged object during the relaxation period) can be often approximated as:

$$\frac{1}{T_2'} = \gamma + \cdot \Delta B_0 \tag{2.7}$$

2.4 Measurement of relaxation

The measurement of these relaxation constants is fundamental to characterize chemical and in-vivo tissue properties. A standard method to measure T_1 relaxation (Tofts, 2003) of a sample require an experiment termed *Inversion Recovery* (IR) schematically depicted in Figure 2.4.2 while the longitudinal relaxation process governed by such T_1 relaxation constant is described in 2.4.1 for brain tissues.

This consist in the application of an RF pulse to invert the magnetization, flip angle homogeneous and near π, then after a pause time (inversion time, T_I) during which the longitudinal magnetization recovers, a second RF pulse is played to create a transverse magnetization with amplitude related with the longitudinally recovered one that is finally measured (readout). The *Block* equations can be simplified to:

$$S(t) = \rho \cdot (1 - 2 \cdot e^{\frac{-T_I}{T_1}}) \tag{2.8}$$

where ρ represents a scaling factor which incorporates the spin density (proton density) and possible inhomogeneity effects of the flip angle or receive scaling effects. From this experiment an estimate of T_1 value can be obtained by measuring the signal with multiple T_I values and fit the signal equation.

Conversely, to assess the transversal relaxation decay (T_2) (Tofts, 2003), the longitudinal magnetization is nulled (90 deg. pulse), after a defined amount of time (T_E), the transversal one is measured as example in Fig-

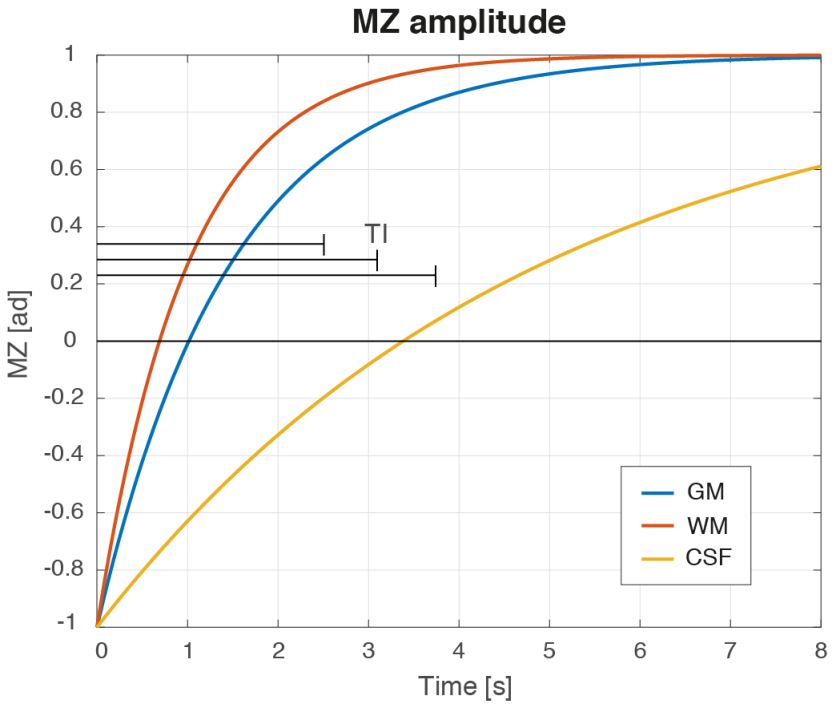

Figure 2.4.1: T_1 recovery of longitudinal magnetisation (M_z) after IR pulse in gray matter (GM), white matter (WM) and cerebro-spinal fluid (CSF). Inversion time for image readout is reported as T_I.

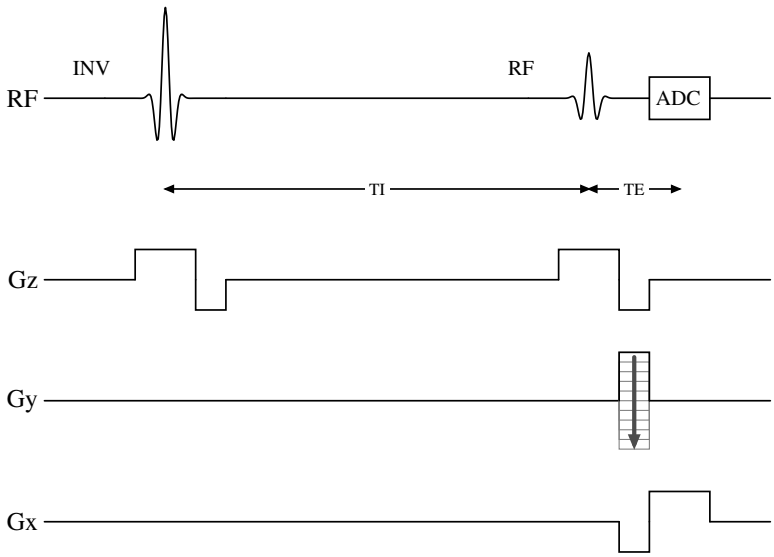

Figure 2.4.2: IR sequence example for T_1 measurements as by (Bernstein et al., 2004).

ure 2.4.3.

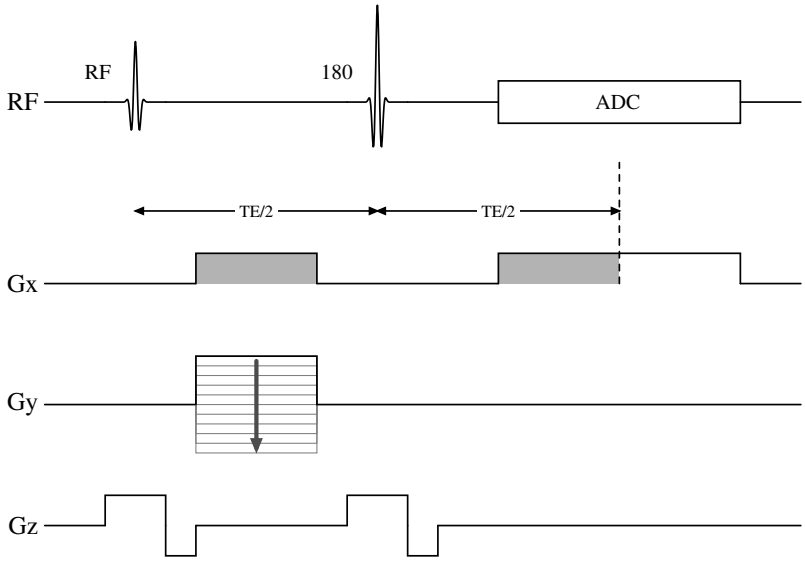

Figure 2.4.3: SE sequence example for T_2 measurements as by (Bernstein et al., 2004).

In such an experiment and no off-resonance effects ($\Delta B_0 = 0\ T$) the *Block* equations can be simplified regarding the transversal magnetisation component to:

$$M_{\perp}(T_E) = M_0 \cdot e^{-\frac{T_E}{T_2} - i\gamma \Delta B_0 T_E} \tag{2.9}$$

Repeating the measurement for an appropriate range of T_E values and fit the equation on magnitude will provide a T_2 estimate following the evolution of transversal decay depicted in Figure 2.4.4 for brain tissues. When the experiment is performed in a sample with a locally inhomogeneous B_0 with dephasing contributions not recovered (e.g. with ad hoc refocusing pulses), a T_2^* decay with similar behavior will occur but characterized by shorter time constant compared to T_2 based on the local field inhomogeneity strength (ΔB_0).

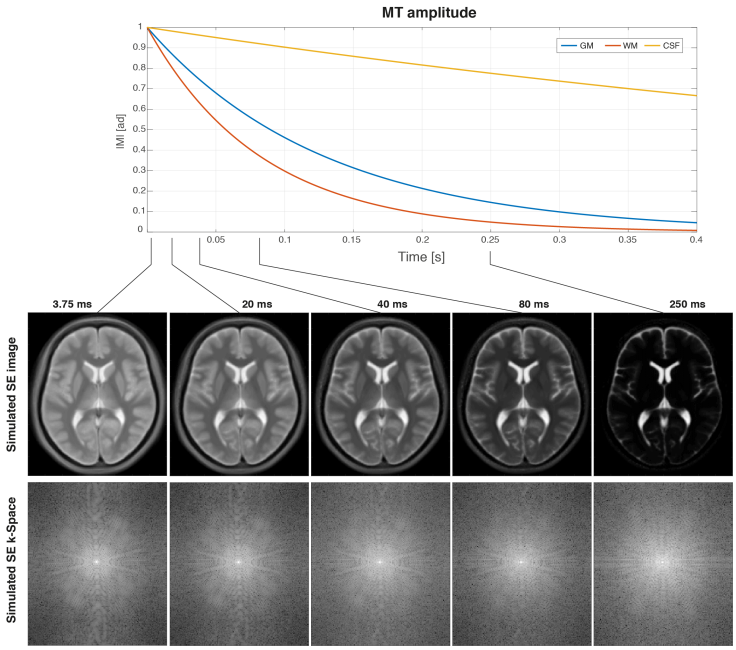

Figure 2.4.4: T_2 recovery of transversal magnetisation (MT) after a saturation RF pulse in gray matter (GM), white matter (WM) and cerebro-spinal fluid (CSF).

2.5 Extended Phase Graphs (EPGs)

The reference method to describe the macroscopic magnetization evolution of single *isochromats* is based on *Bloch* equations. However, despite the availability of simplified solvers (e.g. rotation operator algorithm (Haacke et al., 1999)), solving these equations for spin ensembles with randomly distributed phases quickly becomes numerically intractable and eventually not even of interest in the general case where we are only interested in the echo amplitude and timing.

An alternative approach to describe the dephasing of a spin ensemble under a variety of experimental conditions is given by the *extended phase graph* (EPG) framework (Hennig, 1991; Weigel, 2015). EPG model describe the phase of the spin isochromats ensemble with Fourier sets in order to simplify the description of precession motion in terms of phase accumulation in configurations states that combined provide a convenient description of the echo generation. The configuration states are

defined as the spatial Fourier decomposition of the transversal $M_{\perp} = (M_x, M_y)(r)$ and longitudinal magnetization $M_z(r)$ inside a sample. Each Fourier term will define the phase-frequency content by linear superposition:

$$\begin{array}{lll} M_+(r) & = M_x(r) + iM_y(r) & = \int_V F_+(k) \cdot e^{-ikr}\, d^3k \\ M_-(r) & = M_x(r) - iM_y(r) & = \int_V F_-(k) \cdot e^{ikr}\, d^3k \\ M_z(r) & & = \int_V Z(k) \cdot e^{ikr}\, d^3k \end{array} \tag{2.10}$$

where the magnetisation components can be interpreted as the sum of complex spatial harmonics (F_+, F_-, Z) previously referred as *configuration states* at different wave vectors *k* that represents the spatial frequency domain of the sample:

$$k(t) = \gamma \int_0^t G(t')dt' \tag{2.11}$$

The effect of magnetic field gradients, RF pulses, relaxation and more complex phenomena (e.g. diffusion, motion, etc.) in the Fourier domain of configuration states is computationally simpler requiring only matrix calculations. To describe a spin pool behaviour, the relaxation features (T_1, T_2), spin density (ρ), diffusion properties and kinetic rate of exchange to (model magnetization transfer) can be accounted for describing the magnetization evolution under known RF and gradient waveforms applied (Weigel, 2015).

2.6 Pulse sequences application and contrast

The application of magnetic field gradients to encode the spatial information content of an object with radiofrequencies in the MR spectrum is the basis of MRI and find a natural formalism into Fourier encoding (Haacke et al., 1999). To collect spatially encoded samples, a convenient strategy often used regard the superposition of magnetic field gradients able to

provide linear field variation on top of the main one (B_0) as:

$$B(r,t) \;=\; B_0 + G(t)\cdot r \tag{2.12}$$

where the amplitude and duration of these gradients ($G(t)$) is carefully designed to provide an adequate range precession frequency (ω) across the imaged object:

$$\omega(r,t) \;=\; \omega_0 + \gamma G(t)\cdot r \tag{2.13}$$

and/or spatially-dependent phase variations (ϕ) in the sample:

$$\phi(r,t) \;=\; \gamma \int_0^t G(t^{'})\cdot r dt^{'} \tag{2.14}$$

Integrating along the volume of interest the sample spin contributors, the expected MR signal, neglecting inhomogeneity (ΔB_0) and receive sensitivity effects (B_1^-), should be proportional to:

$$m(t) \;=\; \gamma \int_V \rho(r) e^{i\phi(r,t)} dr \tag{2.15}$$

where $\rho(r)$ depicts the local spin density or proton density. The same equation can be rewritten highlighting the role of gradients (G) and indexing the frequency locations $k(t)$:

$$m(t) \;=\; \gamma \int_V \rho(r) e^{ik(r,t)\cdot r} dr \tag{2.16}$$

The previous equation can be inverted through an inverse *Fourier transform* to obtain the $\rho(r)$ from measured k-space data. This inversion maps frequency to image domain directly if data is collected over a regular sampling grid (Fast Fourier Transform, *FFT*) or non-uniform sampling grid (Non Uniform Fast Fourier Transform, *NUFFT*).

2.6.1 Pulse sequence example

This principle is implemented in the *gradient echo* pulse sequence (Bernstein et al., 2004) consisting of an RF excitation pulse followed by a signal

readout along with two or more imaging gradient lobes responsible for the creation of the recalled echo. A first gradient lobe de-phase the spin pool (pre-phasing lobe) while a second linearly recovers the spin phase (first half of the lobe) and de-phase them again (second half). Recalled echo is seen as an induced voltage in the receive coils that is converted, via an analog to digital converter (ADC), to MR sampled signal inserted into proper k-space positions. An example of data collection with this approach is reported in Figure 2.6.1.

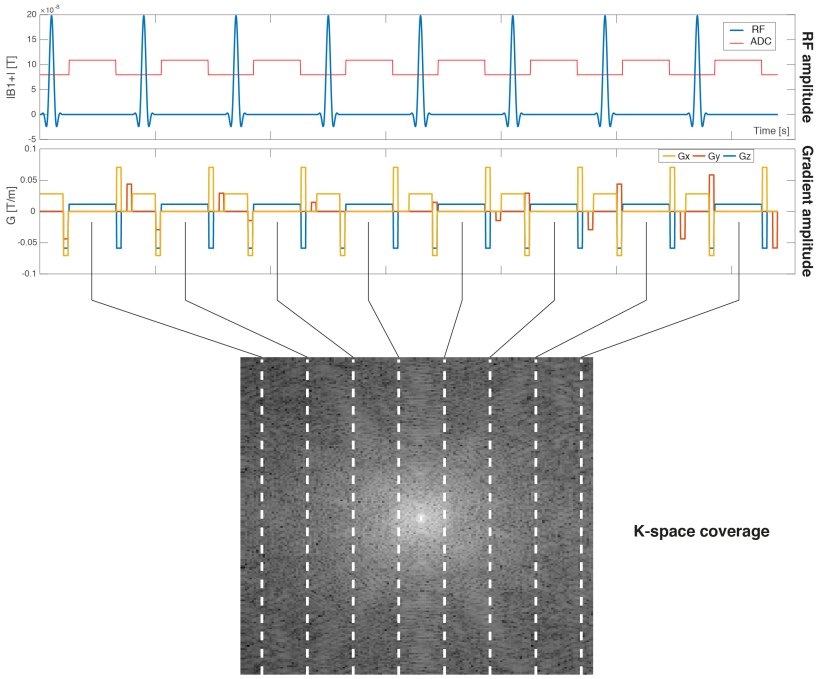

Figure 2.6.1: Example of gradient echo sequence with k-space lines covered to fill the acquisition matrix which discretize the full k-space.

2.6.2 Imaging k-space trajectories

The example in figure 2.6.1 report a typical 2D sequence diagram (3D encoding follows by phase encoding the k_z direction) with gradients tailored to follow a linear path in the k-space where the x-gradient (G_x) span the k_x coordinate (lines) while y-gradient (G_y) event introduce phase offsets that correspond to vertical k-space shift along k_y direction, needed to

cover adjacent lines. Such a k-space filling scheme (sampling trajectory) is referred as *cartesian*. Other trajectories proposed to achieve higher sampling efficiency and robustness to motion are shown in Figure 2.6.2 (see (Bernstein et al., 2004) for reference).

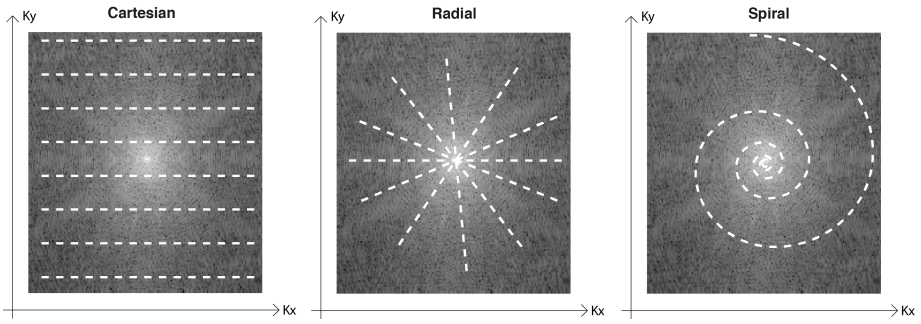

Figure 2.6.2: Examples of k-space trasversal patterns: Cartesian (left), Radial (middle), Spiral (right)

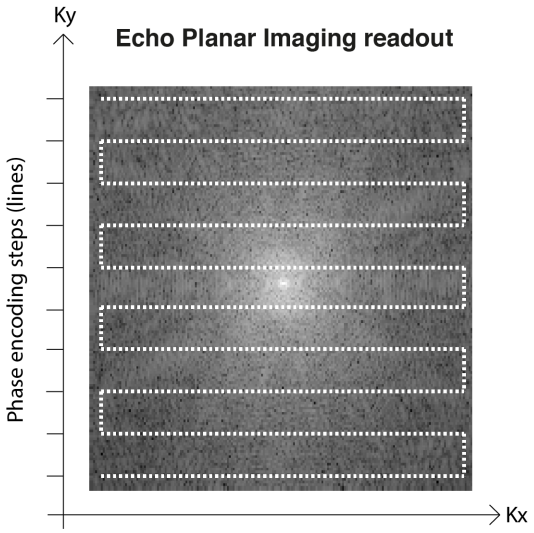

Figure 2.6.3: EPI sequence k-space pattern measured after a single shot.

Acquiring k-space data following zig-zag pattern after a single (or few) RF excitations is referred as *Echo Planar Imaging* (EPI) (Haacke et al., 1999) for example shown in Figure 2.6.3 with cartesian-like pattern. This readout technique is very convenient for its data collection speed, ultimately

modulated by the number of k-space lines that can be consequentially acquired (echo train length - ETL). The actual ETL is however instrinsically limited by the T_2^* (see Figure 2.6.4) which modulates the decaying signal amplitude introducing T_2^* blurring effects.

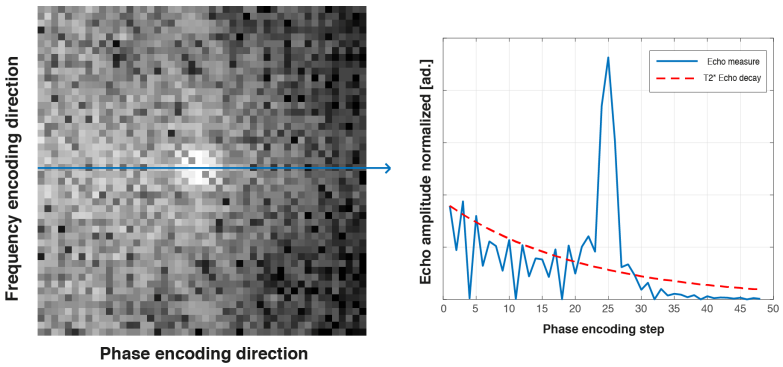

Figure 2.6.4: EPI signal distortions by T_2^* effects.

To limit T_2^* blurring, instead of collecting a single long EPI readout after each shot (single-shot EPI), the k-space can be filled after multiple RF excitations (multi-shot EPI), of interest in extended field of view (FOV) applications. Rapid gradient slew rate required for fast imaging involve less precise k-space traversal caused by gradient delays resulting in intensity ghosts. An enhanced sensitivity to off-resonance and motion effects is also affecting the EPI readout causing potential signal dropout and geometrical distortion while this sensitivity could be well employed for T_2^* imaging.

2.6.3 Data undersampling

When high resolution and/or large FOV are prescribed, k-space data collection for each slice can be a time-consuming process that introduces motion sensitivity and related artefacts ultimately limiting the achievable voxel size. Popular strategies to cope with under-sampling effects are based on sensitivity encoding (*SENSE*) (Pruessmann et al., 1999) or Generalized Auto-calibrating Partially Parallel Acquisition (*GRAPPA*) (Griswold et al., 2002) to lower the data sampling need while maintaining ad-

equate overall image quality in MRI scanners equipped with phased array coils able to measure spatially redundant signals (Pruessmann et al., 1999), a feature exploited during the reconstruction to cope with missing k-space points.

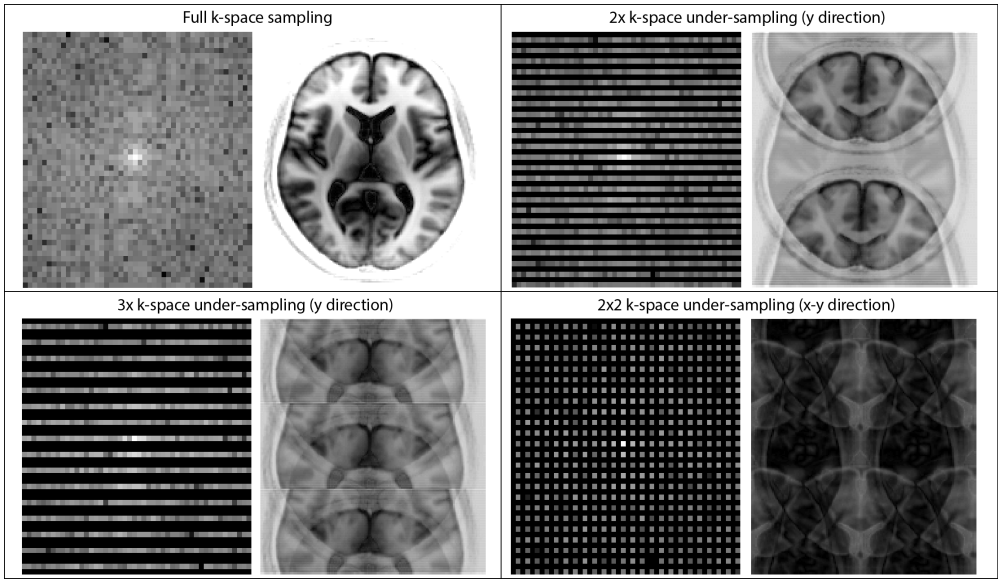

Figure 2.6.5: k-space undersampling effects and associated zero filled k-space (downsampled for representation purposes)

SENSE resolve the spatial aliasing due to undersampling providing a combination of single-coil images within a full FOV solving a linear inverse problem:

$$P = S \cdot I \Rightarrow I = (S^H \cdot \Psi^{-1} \cdot S)^{-1} S^H \cdot \Psi^{-1} \cdot P \tag{2.17}$$

where P accounts for the partial FOV aliased images, S the sensitivity coefficient of each measurement receive coil, Ψ for the noise covariance matrix between coil elements (hardware, loading effects, etc.) and I the full FOV unaliased image of each image voxel. Instead, in *GRAPPA* omitted k-space locations are estimated by interpolators (kernel functions) before the image reconstruction. Kernel functions are identified from a set of fully sampled lines typically encompassing the center of k-space (au-

tocalibration lines, ACS) and used to estimate omitted k-space positions assuming their generalizability to outer k-space locations.

2.6.4 MULTIBAND IMAGING

Recent technical improvements made also available methods to accelerate even the slice dimension of the prescribed multi-slice volume (see Figure 2.6.6). These methods are based on multiband RF excitations (Moeller et al., 2010) played to excite and acquire multiple slice locations simultaneously encoded by a slice selection gradient instead of traditional GRE-EPI RF played at a single specific frequency band.

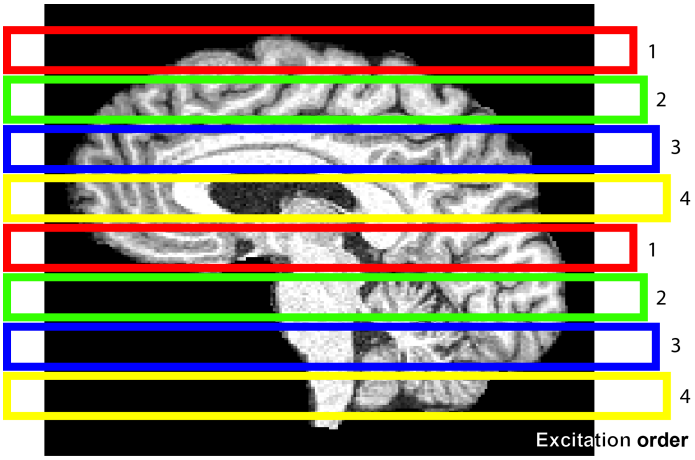

Figure 2.6.6: T1w image with multiple excited slices (2x) and slice scan ordering along a saggital brain slice prescribing 2D axial slices.

From the signal equation (Haacke et al., 1999), each receive coil channel will sample a linear combination of signals obtained from multiple slice locations weighted by its coil sensitivity profile. Consistent reconstruction quality (i.e. successful unfolding of simultaneously excited 2D slices) was obtained with a convenient phase offset between each pulse aimed, through a Fourier transform perspective, to spatially shift the excited slice associated to each RF pulse band with a different amount (Setsompop et al., 2012). The scan time advantage is directly proportional to the number of slices that can be simultaneously excited. However, the

slice ill-posedness associated to the slice un-aliasing process intrinsically elevates the reconstruction *g-factor* (Setsompop et al., 2012) also depending on the RF excitation performance and receive coil configuration available which affecting overall the unfolding capabilities.

A recent reconstruction approach by (Setsompop et al., 2012) named *slice-GRAPPA* employ the reference data (pre-scan calibration) in a GRAPPA-like linear framework to fit distinct kernel sets (one for each simultaneously excited) subsequently used to fit k-space positions of different slices to effectively unfold superimposed contributions while limiting spurious signal leakage effects (Cauley et al., 2014) among simultaneously excited slices.

2.7 Functional MRI

Thanks to its peculiar T_2^* sensitivity, the GRE sequence found a wide variety of applications (Bernstein et al., 2004) where the collected images can conveniently depict objects based on their T_2^* differences. This sensitivity enabled to probe in-vivo the temporal variability of the local blood oxygenation, extensively used as image contrast mean for functional brain activation. This association derive from the pioneering studies that led in 1993 to the concept of *blood oxygenation level dependent* (BOLD) contrast, later found to be a reliable metabolic correlate to neuronal activity (Ogawa et al., 1990). The *BOLD* contrast is based on the idea that different levels of blood oxygen concentration provide significant differences of magnetic susceptibility in a sample.

Ogawa (Ogawa et al., 1990) found that physiological variations of blood oxygenation levels were strong enough to provide measurable T_2^* fluctuations. Following the original idea that the neural activity and cellular metabolism are correlated with changes in blood flow first empirical evidence arose relating the action potential response of neuron cells and later the local *electrical field potential* (LFP) (Logothetis, 2002) on groups of neurons briefly stimulated to the hematic activity.

Considered its biological relation to the oxygen and blood flow the

question about the metabolic contributions that explain the *BOLD* signal arose quickly in the neuroscience community which tried to estimate the metabolic demand associated with neural activity finding that at least blood flow could be driven by excitatory post-synaptic activity processes.

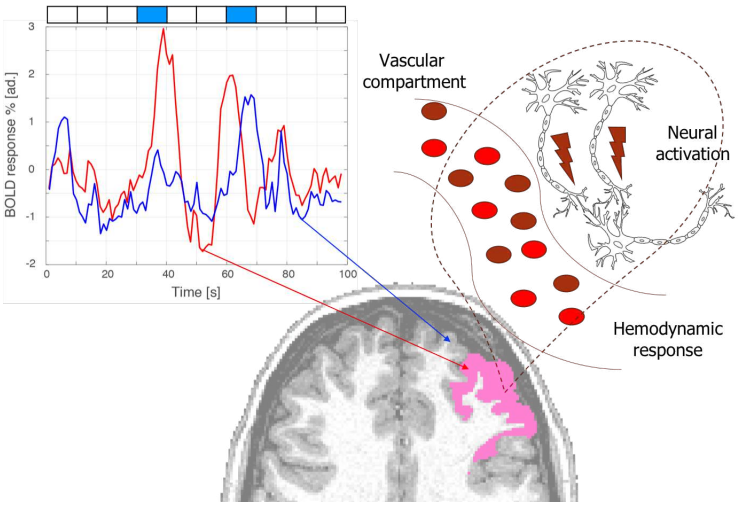

Figure 2.7.1: BOLD response as determined from a task administration to activate the brain cortical area depicted in purple in the structural image overlay in trasparency. Focus on the local vasculature response is reported depicting the elicited neural response and resulting hemodynamic response involving an unbalanced Hb content responsible for T_2^* variations, measurable in voxels whose traces are reported for example in the box on the left (typical BOLD response dynamics, z-scored).

For these reasons, the temporal tracking of BOLD contrast fluctuations is among the most commonly used methods for brain functional mapping and functional connectivity (FC) (Biswal et al., 1995a) under task or spontaneous conditions (see Figure 2.7.1) based on low spatial resolution GRE images. Temporal sampling frequency should be adequate to describe BOLD signal contrast variations (Lindquist et al., 2009), found to interest the frequency range of 0.01 to 0.1 Hz and spatial range of few mm.

2.8 Positron Emission Imaging principles

Positron Emission Tomography methods add a fundamental feature that often is confounded in MRI: the biological specificity and interpretation.

The significance of this methodology stems from the pioneering studies of the cerebral blood flow at whole brain scale (due to technical limitations progressively passed) that also combined arteriovenous sampling to further refine the biological meaning of tracked biological process removing all others substrates and confound metabolites paving the way to our current understanding of the relationship between substrate delivery and utilization in the human brain. Currently PET is an in-vivo functional imaging technique able to assess the quantitative distribution of a positron-emitting radionuclide (Sokoloff et al., 1977a). The radioactive decay of known as unstable isotopes, referred as radionuclides (e.g. 18-F, 15-O, etc.), results in the generation of measurable photons (see Figure 2.8.1).

The spatial distribution of decaying isotopes can be then reconstructed with tomographic image tools (Valk, 2004), to depict the in-vivo distribution of an injected radiopharmaceutical. The sampling performances of current PET systems are a tradeoff between spatial resolution (typically 2 to 5 mm) and temporal resolution (typically minutes).

PET radionuclides are especially suited, for their chemical resemblance, to the normal constituents of biological molecules (Phelps, 2004), thus they can be combined to substances known to participate to specific metabolic pathways. Safe application on human subjects was cleared as the radioactive nature of these isotopes has a decay constant of minutes (15-O = 2 min) to hours (18-F = 110 min) making them practical for in-vivo imaging of blood flow, cerebral glucose and oxygen transport and utilization.

However, radiopharmaceuticals can be chemically unstable and provide functional variability depending on the location and dose, therefore to disentangle the biological pathways followed by these substances by appropriate mathematical models of the PET tracer and biological system

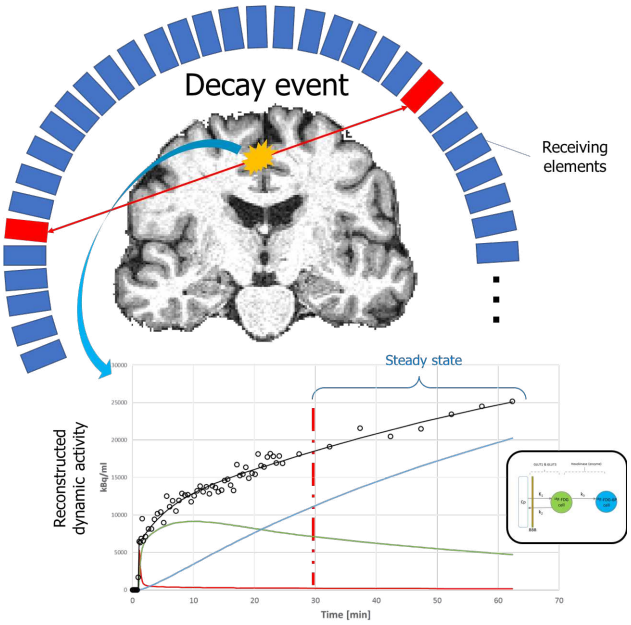

Figure 2.8.1: PET experiment consisting of tracer injection, measurement and reconstruction of local activity as dynamic process with physiological information regarding the biological tracer pathways.

(Sokoloff et al., 1977a).

The simplest characterisation, often used in clinical application for its simplicity, require the calculation of the tracer concentration in a region of interest, defined as a single-frame acquisition of the average PET activity (sum of the raw counts) from the region. Normalizing this quantity by the injected dose and anthropometric characteristics of the subject (e.g. weight, body surface area, the standardized uptake value (SUV) (Keyes, 1995) is obtained. SUV consist in a semi-quantitative index useful for its general applicability but limited from an interpretation point of view from the lack of a specific model for the tracer kinetic (Keyes, 1995).

2.8.1 Integrated PET/MRI Scanners

In-vivo MRI and PET imaging offer non overlapping information and opposite limitations: PET can investigate a wide range of physiological, pathological and biological processes with high specificity but low spatial resolution while MRI provides high spatial resolution for both structural

and functional characterization. Therefore, an imaging system capable of simultaneous PET and MRI measurement can enforce the spatial accuracy and relaxation-based contrast of MRI with the metabolic contrast and quantitative information about the underlying tissue of PET. However, the advantages of combining PET and MRI go beyond the spatial localization improvements obtained using MRI in place of CT, requiring innovative solutions to solve the technical challenges associated with the interference between these two modalities (Jung et al., 2016).

This technological effort initiated two commercially available and approved by Food and Drug Administration human PET-MRI scanners introduced after 2010 and capable of simultaneous PET and MRI imaging respectively from Siemens Healthcare (Biograph mMR; Siemens Healthcare Sector, Erlangen, Germany) and General Electric Healthcare (Signa PET/MR; GE, Waukesha WI, USA) (Ladefoged et al., 2017).

Despite the effort in using PET-transparent materials, PET-MRI scanner nonetheless suffer from an appreciable activity attenuation even considered the relatively high energy of the annihilation radiation. This attenuation can be corrected estimating the attenuating path followed by photons along different structures (human body, scanner bed, RF hardware, etc.) before impacting on the receiving detectors and reversing the estimated attenuation on the activity before or during the PET image reconstruction stage.

The development of robust methods for attenuation correction has been a major challenge in PET/MRI that promoted a rapid evolution of standard correction methods (Catana, 2017) for example atlas-based or MR-derived tissue segmentations (Martinez-Moller et al., 2009; Muzic and Di-Filippo, 2014) (with assumed attenuation coefficient). A significant jump is due to the application of deep learning methods to learn the spatial distribution of the attenuation (Liu et al., 2018a) with results approaching standard CT-derived attenuation maps.

A fundamental difference that marks the advent of PET/MRI compared to traditional PET is however the development of PET reconstruction methods able to exploit the anatomical information to enhance the

reconstruction accuracy extracting spatial anatomical priors derived from atlases or, more interestingly, from the MRI images themselves (Ehrhardt et al., 2016). Joint probabilistic models for estimation of PET activity (Hwang et al., 2018) has been proposed for PET/MRI scanners exactly because of the inherent spatial alignment between PET and MRI data without subject repositioning. The PET reconstruction can also make use of motion estimates provided by MRI (or the PET data itself) to correct for motion effect increasing the effective PET spatial resolution and eventually lowering the injected dose (Kang et al., 2015).

Simultaneous acquisition of PET and MRI data allows maximal temporal correlation between functional and anatomical information from both modalities, combining MRI-derived anatomical and function data and PET-derived biologically specific and quantitative information about the tissue function. This offer special opportunities where the timing and spatial accuracy are critical such as in cardiology, stroke, neurodegenerative disorders, oncology or brain assessment (Catana, 2017).

3

Methods to study and integrate functional connectivity and energy metabolism

Considering the variety of clinical applications based either on alterations of the brain organisation structure or local glucose metabolism, very few studies studies tried to connect such alterations using multi-modal measures. This chapter describes the state of the art methods for FC and metabolic analysis reporting experimental approaches and important results associating these two modalities.

3.1 Functional Connectivity

3.1.1 Introduction: evolving definitions and relation to brain connectome

Based on the idea of functional connectivity as functional association between areas, many different experimental approaches based on *brain*

hemodynamic alterations were designed to directly, e.g. with Near Infrared Spectroscopy (NIRS), or indirectly, e.g. with fMRI through the BOLD contrast (Glover, 2011) extended by also probing the joint perfusion as sampled with Arterial Spin Labeling (ASL) approaches (Steketee et al., 2015), fundamental to provide dynamic functional activity measures to be associated in order to defined the brains FC.

Given the advantage of non-invasive in-vivo sampling with both high spatial and temporal resolution, *fMRI*-based methods soon gained prominence in literature. Historically BOLD-fMRI (Bandettini et al., 1993) have found early application in functional connectivity (fcMRI)(Biswal et al., 1995b; Friston, 2011) to the point that have recently become a popular non-invasive method to probe inter-area association based on statistical dependence measures. Two macroscopic areas are said to be functionally connected (Friston, 2011) when they exhibit a significant association based on the correlation between BOLD signals (see Figure 3.1.1 for an example).

While interesting connectivity results can be obtained during a task activation experiment aimed at identifying co-activating brain groups of areas (*functional networks*), much of the FC literature has been devoted in fMRI to the analysis of the resting-state brain condition starting from the seminal work of Biswal et al. (Biswal et al., 1995b). This observation was soon extended reporting (Beckmann et al., 2005) that many different systems actually co-exist in the brain and are distinguishable from each other due to their relatively different hemodynamic behavior which results in the possibility of measuring consistently different activity time courses.

Numerous studies found a complex organization system of different networks, referred as *resting state networks* (RSN) (Sporns, 2013) present even under non-physiologic conditions (e.g. anaesthesia or pathology) and consistent across subjects (Thomas Yeo et al., 2011). Recent applications found interesting similarities in organization structure among connectomes derived from rs-fMRI and task-fMRI (Gordon et al., 2017), enhancing the experimental robustness while offering a more extensive val-

idation (e.g. by means of independent PET measures).

Considering the existence of such network structures, continuously maintained even at rest (as supported by many metabolic studies (Raichle, 2006)), the brain is believed to be continuously engaged in some sort of conscious (e.g. reasoning processes) or subconscious activities (e.g. learning) but always set to react to external stimuli. This operational burden is the basis of the high human brain metabolic demand to be justified from the connectome organization perspective rather than only from cellular scale considerations. Multi-modal MRI provided connectome estimates by similarity of local anatomical measures such as the cortical thickness (Evans, 2013) while FDG-PET measurements correlated across subjects provided the concept of metabolic connectivity (Di and Biswal, and Alzheimer's Disease Neu, 2012).

When it comes to experimentally define functional connectomes based on fMRI measures, two fundamental steps are required: delineate areas of interest (functionally discrete brain areas) and correlated their associated activity profile (as a probe for their connectivity). From a *graph theory* perspective (van den Heuvel et al., 2009) where a graph is a formal object defined by a set of nodes and a description of the interconnections among them, delineated areas basically consist in the functional nodes of the graph (i.e. brain network) while their interconnections are defined according to the association degree among areas (i.e. their functional connectivity).

The process of generating a functionally meaningful set of functional brain areas in rs-fMRI literature is referred to *parcellation*. Previous parcellation techniques were based on putative anatomical landmarks (Desikan et al., 2006). Recent approaches shifted toward defining areas according to their presumed associated brain function to maximize the local coherence of measured signal (Gordon et al., 2016) providing more functionally homogeneous areas. However, these consist in hard parcellation approaches where the set of parcels is derived from the group- to the subject- level traditionally through accurate registration processes.

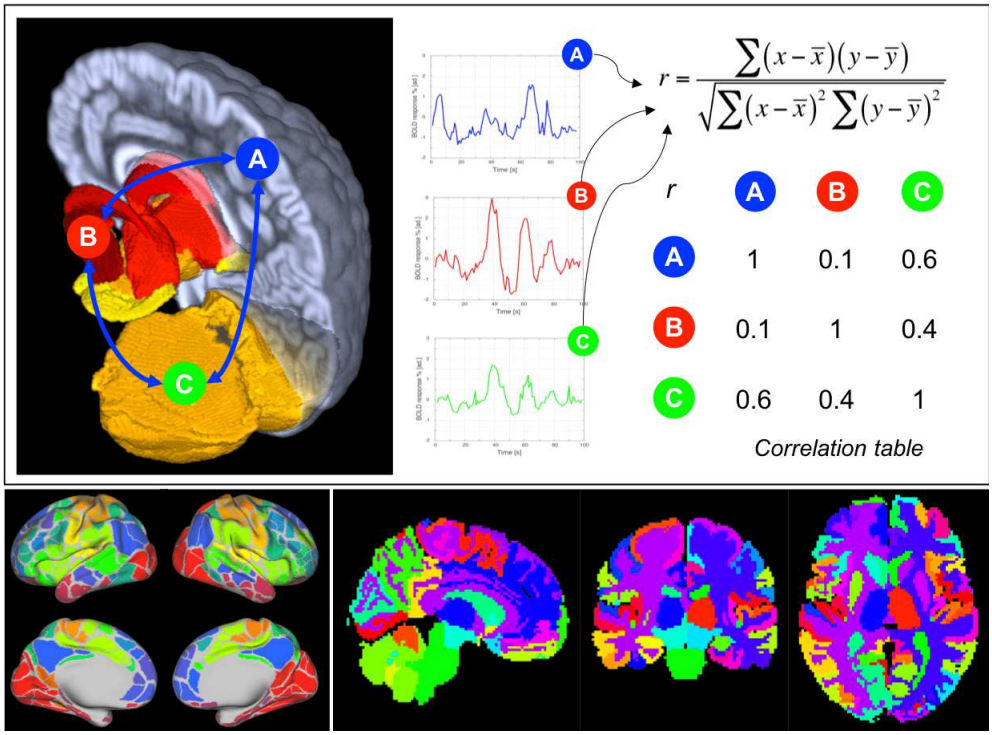

Figure 3.1.1: Computing functional connectivity. *Top-Left)* Resting state functional MRI (rs-fMRI) signals are averaged within three functional parcels (indexed as A, B, C). The associated average signals are Pearson cross-correlated generating an individual correlation matrix *Top-Right)* from the pairwise, parcel-to-parcel correlations corresponding to edge strength of the functional connectivity matrix. *Bottom-Left)* Representation in overlay to an inflated cortical surface mesh of functionally delineated parcels (according to Gordon-Lauman atlas) colored according to the belonging network. *Bottom-Right)* Volumetric sagittal, coronal, axial views of an anatomical atlas (MALF atlas) colored according to the parcel indexing (not by functional network).

A successful methods for the analysis and parcellation was the *independent component analysis* (ICA) which was the first used in literature to isolate a set of coactivated areas in resting state, referred as RSN, whose connectivity defines the basis for the identification of anatomically distinct but functionally interconnected networks later subject of extensive investigation(Beckmann et al., 2005).

The role and processing structure of the brain at rest, represented through these networks, have been linked to fundamental human cognitive and emotional performances (Greicius et al., 2003) while sharply disrupted in pathologic conditions (Fox, 2010; Whitfield-Gabrieli et al., 2009). Previous studies based on resting state FC were able to associate a lower connectivity level (ipo-connectivity) between networks to pathological state in patients affected by schizophrenia or significantly altered from healthy controls as observed in Alzheimer disease (Grothe et al., 2017) or Schizophrenia (Zhu et al., 2017).

Regardless of the delineation principle, when defined on large scale (low spatial resolution, up to dozens), functional areas and their connectivity describe network-level connectivity while fine brain parcellations (higher spatial resolution, up to hundreds) by describing the interaction of finer functional units may reveal which nodes or sub-networks are actually driving the RSN-level connectivity (e.g. possibly seen with lower resolution parcellations).

3.1.2 Practical FC and modelling approaches

Once a parcellation scheme has been defined, each parcels fMRI dynamic (typically obtained by averaging the rs-fMRI signals of all voxels part of the parcel) will represent the subject response during the resting state experiment as for example depicted in Figure 3.1.2. Then, the full set of all possible pairwise interactions among parcels (i.e. FC) could be summarized in a $N_{parcels}xN_{parcels}$ matrix (often referred as FC matrix) where each correlation will correspond to a network edge (connection among two nodes), altogether representing the subjects functional connectome

during that resting state experiment.

Often the association among parcels is based on *Pearson linear correlation* (Friston, 2011) or similar point-wise measures such as the cosine similarity (Shen et al., 2012) boiling down the entire process of FC identification to an iterative detection of a set of dependent correlations (because of the RSN-structure existence), possibly highlighting the statistically significant ones (e.g. significantly non-zero correlations between associated dynamics).

The operational simplicity of this correlation and its straightforward interpretation justified its large use in fMRI literature but produced an entire literature field of issues to be addressed to achieve genuine representation of the brain networks (note that we still lack from a suitable ground truth).

Partial correlation can instead disentangle the association between two parcels while simultaneously conditioning on all the others, generalizing to all nodes this requires the knowledge of a full sample covariance matrix. Null partial correlation inform if the two parcels to be conditionally independent under Gaussian conditions that are not met in practical rs-fMRI conditions, resulting in the need of regularized schemes such as based on L1-sparsity to account for noise propagation (Smith et al., 2011). The need for careful regularization could lower its statistical power resulting of limited applicability in the typical experiment consisting of a limited number of time points finally limiting its applicability.

It worth noting that many other methods are available to measure (Friston, 2011) and pre-process the fMRI data in order to remove confounds (more carefully described in a later section), but the critical step resides in the method used to infer each connection, possibly influencing all network analysis and derived features, however few studies focused on the reliability of detected structures to essentially validate available methods, a major theme of this thesis.

While the distinction between direct and indirect has been studied by Smith et al. (Smith et al., 2011) who proposed functional model identification based on partial correlation to provide more physiologically

meaningful structures rather than refined covariance descriptions, more complex models were proposed based on Granger causality (Deshpande and Hu, 2012), Dynamic Causal Models (Friston, 2011), Structural Equation Modelling (McIntosh and Gonzalez-Lima, 1994), Bayesian Networks (Ramsey et al., 2010) or time-series Non-Gaussianity (Hyvärinen and Smith, 2013) to simultaneously deal with the edge existence as well as its directionality (introducing the causality notion). Moreover, as there is some consensus about the majority of brain connections as bi-directional (Markov et al., 2014a), sparse methods to infer unidirectional edges may be not appropriate.

3.1.3 Network theory: describing the brains network organisation

The notion of nodes and connections yet considered naturally falls into the context of graph theory (Stam and Reijneveld, 2007) providing to the brain researchers complementary information to task-fMRI experiments. By its very nature, a graph $G = (V, E)$ will consist in a set of nodes (or vertices V with fixed cardinality $[M]$, unique node labelling (cardinal) and fixed ordered set), interpreted as parcelled brain areas, functional parcels or ICA components, and their connectivity represented as edges E (with associated weights contained in a dedicated adjacency square matrix $A[MxM]$) overall describing the complete graph structure. We consider in this context only undirected graph, requiring the adjacency matrix to be as well symmetrical ($A = A^T$).

As the parcellation increase its functional specialization offering progressively detailed views about the brain, the number of nodes whose connectivity is being investigated increase significantly. From this perspective graph theory (Fornito et al., 2013) offers a much needed means to examine the overall structure of the brain network in terms of simple features and abstract concepts (Rubinov and Sporns, 2010) considering the network as a whole rather than as a group of integrated/segregated RSN and describing the information exchange and processing implemented

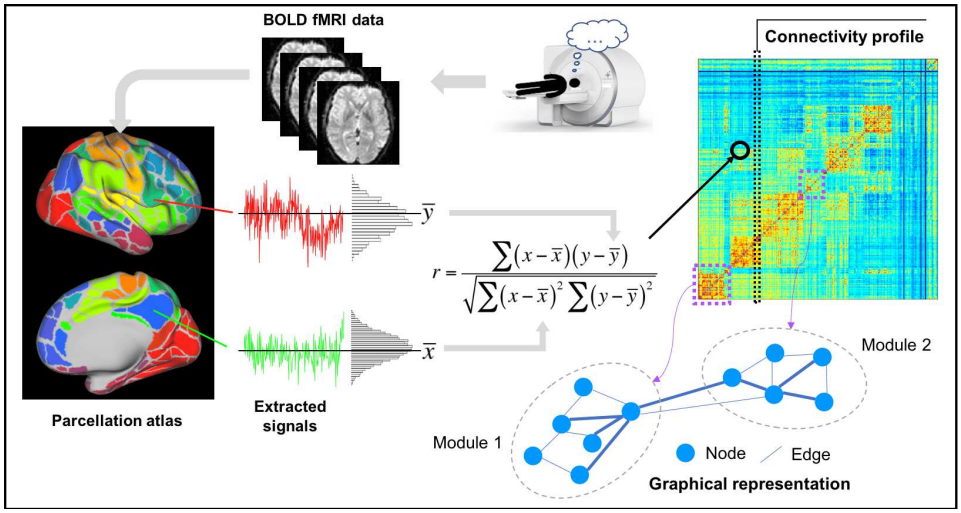

Figure 3.1.2: *Typical pipeline for a connectivity analysis up to the brain network representation.* Starting from a resting state fMRI experiment (top-center, typically collecting at least 12 minutes worth of data), fMRI volumes are pre-processed (filtered, motion corrected, confound regressed, etc.) then parcelled according to a chosen atlas or parcellation method (center-left). The average signal dynamic in each parcel is then Pearson cross-correlated to the dynamic of all other parcels' in order to define a complete FC matrix (center-right). Single rows (or columns by symmetry) of the FC will represent how each node (a.k.a. parcel) is connected to all other nodes in the network (*connectivity profile*), that is represents its relation with the neighborhood. Each FC matrix, considered as an adjacency matrix, can be then represented as a graph structure (bottom-right) and its features then studied according to graph theory tools.

by the brain (Bullmore and Sporns, 2009).

At this level, many strategies were proposed to remove spurious connections. Typically the weakest weights are simply discarded if under a predefined cut-off threshold based on statistical considerations or a predefined sparsity level. This problem could be discussed within the network estimation process, here reported to highlight the unsolved need for precision measures to the connections weights for confident estimation of reliable networks.

3.1.3.1 Noise propagation in FC estimates

Here we show how theoretically the noise propagates though the FC and play an important role in defining its amplitude as well as introducing possible biases related to the spatial inhomogeneity of noise and experimentally how this effect can provide a connectivity loss at single-subject level. The predicted echo signal amplitude at the prescribed time (t) could be described during a GRE experiment as:

$$s\left(t\right) = \ s_0\left(t\right) \ \ e^{-R_2^*(t)\,\mathrm{T}_E} + n\left(t\right)$$

where $s_0\left(t\right)$ accounts for the initial transversal magnetisation, $T_E\ [ms]$ the time passed from the RF excitation (echo time) and $n\left(t\right)$ describes the superimposed noise term, zero-mean and temporally uncorrelated Gaussian distributed.

Considering the linear approximation of such a model proposed in (Liu, 2017), the actual signal variability in the time domain is the variable of interest during a typical fMRI experiment concerned on the signal variability, rather than its absolute value:

$$\frac{\Delta s\left(t\right)}{s\left(0\right)} = \ \frac{\Delta s_0\left(t\right)}{s_0\left(0\right)} \ - \Delta R_2^*(t) \ \mathrm{T}_E + \frac{n\left(t\right)}{s\left(0\right)}$$

respectively describing: the fluctuations of measured signal as contributions from the relative transversal magnetisation difference from the experiment beginning (unstable longitudinal relaxation contributions, slice

cross-talk, motion, in-flow, etc), the temporal fluctuations of transversal relaxation decay (susceptibility differences related to the hemodynamic BOLD response involving unbalanced oxygen and/or blood flow and/or volume local content, instability of ΔB_0 due to scanner instabilities or respiration, etc) and the relative noise contribution.

In fMRI literature the noise contributors to this model have been often described by means of two metrics: the image signal-to-noise ratio (SNR_0) and temporal SNR (tSNR) whose relationship has been formally established in the noise model (Krüger and Glover, 2001). Such a model distinguishes the variability from thermal and physiological origin under linear superposition assumption.

The former noise source was assumed as temporally and spatially (across voxels) uncorrelated Gaussian noise with zero mean and σ_0^2 variance (assumed to be stationary across space, i.e. homogeneously distributed across voxels) while the latter as a zero-mean process spatially uncorrelated with and Gaussian distribution characterized by σ_P^2 temporal variance (not necessarily temporally uncorrelated) which accounts for BOLD-like (σ_{NB}^2) and non-BOLD-like (σ_{NB}^2) contributors as previously described by (Liu, 2017).

According to the Kruger et al. (Krüger and Glover, 2001) noise model, the thermal noise variability (σ_0^2) is independent to the signal level (additive noise, dependent on hardware losses, field conditions and imaged sample) while the physiological noise variability (σ_P^2) is linearly dependent over the actual signal level $s\,(t)$ (modulating noise) according to a proportionality constant (λ tissue-dependent): $\sigma_P \propto \lambda\, s\,(t)$ demonstrating how better receive hardware sensitivity (higher B_0 and flip angle, denser receive coil array, larger voxels or limited image acceleration) actually explain the improved BOLD signal sensitivity over the noise (σ_{NB}^2), unfortunately accompanied by higher sensitivity to non-BOLD sources of variability (σ_{NB}^2).

Within this framework SNR_0 can be determined as the voxel-wise ratio between the locally measured signal $s\,(t)$ (averaged in time) and the overall thermal noise standard deviation (σ_0).

Instead, the tSNR measure had been defined as the ratio of the locally measured signal $s(t)$ (averaged in time) and the total standard deviation of the measured signal ($\sigma_t = \sqrt{\sigma_0^2 + \sigma_P^2}$). These noise measures were analytically associated as:

$$tSNR = \frac{\text{SNR}_0}{\sqrt{\sigma_0^2 + \sigma_B^2 + \sigma_{\text{NB}}^2}} = \frac{\text{SNR}_0}{\sqrt{1 + \lambda^2\,\text{SNR}_0^2}}$$

From this relation, two asymptotic scenarios can be distinguished:

1) Small SNR_0 negligible $\text{SNR}_0^2\ \lambda^2\,\text{SNR}_0^2 \ll 1 : tSNR \cong \text{SNR}_0$

2) High $\text{SNR}_0\ \lambda^2\,\text{SNR}_0^2 \gg 1 : tSNR \cong \frac{1}{\lambda}$

The first scenario can be achieved under thermal noise regime requiring $\sigma_0^2 > \sigma_P^2$ that is measured signal variability contribution mostly defined by the statistical features of the thermal noise, nonetheless favourable by adequately balancing the benefits of thermal noise regime (noise assumption of spatial uncorrelation more valid) to the actual noise amplitude level which should not completely obscure the BOLD contribution.

The second scenario highlights a substantial dependence of the tSNR by the tissue-specific signal variability rather than the actual image noise (SNR_0) typically reporting progressively lower values from white to grey matter and CSF directly associated to the physiological signal variability of these tissues with strong dependence over the average signal according to (Krüger and Glover, 2001).

Specifically, under this noise regime ($\sigma_0^2 < \sigma_P^2$), providing higher SNR_0 by means of lower noise figure by better receive hardware or lower spatial resolutions not necessarily improves the tSNR.

Note that, in this case the usually costly enhancement related to hardware improvements, do not guarantee any improvements in terms of BOLD signal sensitivity described in terms of BOLD contrast to noise ratio (CNR_B) once the main field strength (B_0) and voxel size are defined in (Wald and Polimeni, 2017) by:

$$\mathrm{CNR}_B = \frac{\Delta R_2^*}{R_2^*}\,\mathrm{tSNR}$$

with ΔR_2^* relative to the baseline R_2^* describing the BOLD effect of interest to measure reportedly modulated only by the local tSNR suggesting in agreement with (Wald and Polimeni, 2017) a more favourable framework for fMRI measurement to be attained under thermal noise regime simultaneously limiting spurious spatial correlation effects non related to the BOLD activity.

This relation appoints the ability of an fMRI experiment to detect small BOLD signal changes mostly upon the actual tSNR amplitude nonetheless providing a sensitivity lower bound for the detection of the co-activation of putative brain areas. This suggest that in general it make sense to have highest possible tSNR but not necessarily this needs to be achieved through higher SNR_0 depending on the actual noise regime prescribed, entailing experimental optimisation scenarios that could as well feature less performing hardware for example making use of lower main field or less dense receive array coil (neglecting other acquisition advantages as parallel imaging) potentially with limited penalty in terms of fMRI measurement quality.

The actual noise regime existing in a given experimental setting could be practically be inferred evaluating the ratio of local thermal (σ_0) to physiological noise (σ_P) variabilities. Considering previous formulations and assumptions this measure can be however conveniently determined from the SNR_0 and tSNR as (Wald and Polimeni, 2017):

$$\frac{\sigma_P}{\sigma_0} = \sqrt{\left(\frac{\mathrm{SNR}_0}{\mathrm{tSNR}}\right)^2 - 1}$$

this ratio had been reported to be remarkably related to the flip angle (Krüger and Glover, 2001),main field strength and voxel volume by (Triantafyllou et al., 2005) while later accounting for the noise correlation across receiving elements of the array (Triantafyllou et al., 2011) or accounting for physiological noise scaling effects (Triantafyllou et al., 2006).

Nonetheless, it has been suggested (Wald and Polimeni, 2017) that the actual noise regime could be inferred by observing the spatial distribution in the imaged sample of the tSNR. It had, in fact, observed that under thermal noise regime the tSNR pattern should follow the spatial appearance of the array coil receive sensitivity profile (thus similar to the SNR_0 pattern with monotonical decay moving away from the coil elements), while under physiologically dominated noise the appearance should entail neat brain tissue separation and ranking of tSNR according to the voxel content.

Building upon previous assumptions, the physiological noise contributions over the total signal variability is stable once the main field and signal defining elements (B_0, flip angle, voxel size, T_E, T_R) are set in agreement with (Triantafyllou et al., 2011). Considering experimental protocols (i.e. fMRI sequence settings) with these parameters matched, should entail acquisitions affected by similar physiological noise content, while other sequence parameters (not modulators of the signal amplitude) like the image acceleration, would instead only control the propagation of thermal noise to the measured signal. In this case, the tSNR measure is a direct probe of thermal noise propagation.

Despite the extensive work of dedicated literature, fMRI denoising is still not completely effective (Bright et al., 2017), requiring researchers to consider the variability in residuals as associated to the thermal noise propagation (with variance described by the σ_0^2 term in previous modelling notations) and physiological noise variability (σ_P^2) of both neural (BOLD-like) or non-neural (confounds not completely removed) origin.

Under Gaussian assumptions, the physiological noise would as well been considered Gaussian distributed, linearly superimposing as:

$$\varepsilon(t) = P(t) + T(t)$$

where the time-course of fMRI signal residuals can be decomposed as $P(t)$ physiological contributions Gaussian distributed with zero-mean and temporal covariance structure summarized by means of outputs from

an AR(p) model (of appropriate order p (Arbabshirani et al., 2014)) whereas $T(t) = T$ describes the thermal noise content Gaussian distributed with zero mean and temporally uncorrelated variance σ_0^2. Both of these sources correspond to stationary random processes consistent with noise models previously discussed. Considering the GLM residuals obtained from two putative brain areas as: $\epsilon_1 = P_1 + T_1$ and $\epsilon_2 = P_2 + T_2$ (dropping the time index for notation simplicity and assuming in general different distribution variances by areas), their Pearson linear correlation is defined as:

$$r = \frac{E\left[\epsilon_1 \cdot \epsilon_2\right]}{\sqrt{\text{Var}\left(\epsilon_1\right)} \cdot \sqrt{\text{Var}\left(\epsilon_2\right)}} = \frac{E\left[(P_1 + T_1) \cdot (P_2 + T_2)\right]}{\sqrt{\sigma_{P,1}^2 + \sigma_{0,1}^2} \cdot \sqrt{\sigma_{P,2}^2 + \sigma_{0,2}^2}}$$

Assuming linearity principle and under Gaussian distribution hypothesis (zero-mean) the previous definition could be reframed after some term rearrangements as:

$$r = \frac{E\left[P_1 \cdot P_2\right]}{\sigma_{0,1}\sqrt{1 + \left(\frac{\sigma_{P,1}}{\sigma_{0,1}}\right)^2} \cdot \sigma_{0,2}\sqrt{1 + \left(\frac{\sigma_{P,2}}{\sigma_{0,2}}\right)^2}}$$

Highlighting that the Pearson linear correlation is directly dependent on the covariance between physiological noise contributors ($P_1,\ P_2$) in the two areas while inversely dependent over the thermal noise standard deviation amplitudes ($\sigma_{0,1},\ \sigma_{0,2}$) and a factor directly related to the $\frac{\sigma_{P,i}}{\sigma_{0,i}}$, that is the locally delivered physiological-to-thermal noise ratio.

This equation suggests that the actual connectivity between two brain areas depends on their local thermal noise scaling ($\sigma_{0,1},\ \sigma_{0,2}$). In turn, the latter depends on the spatial pattern of thermal noise propagation (i.e. the SNR_0) which under parallel imaging conditions could be highly non-homogeneous (SNR_0 further restrained by the g-factor (Breuer et al., 2009)) nonetheless introducing a non-trivial modulation of the actual functional connectivity between two brain areas based on their spatial position across the array sensitivity profile.

Interestingly, the above measure of connectivity is also locally dependent on the achieved noise regime of both areas. Under global thermal

noise regime, the correlation would still be potentially modulated by the SNR_0 pattern while under physiologic noise regime is mostly dependent on the actual physiological variability of the two areas thus purposely modulated more by the actual BOLD variability scaling.

While the experimental acquisition choices could significantly help in reducing the sensitivity of functional connectivity measures from the spatial correlation, the deliberate propagation of thermal noise should be carefully accounted for in functional connectivity studies because, as opposed to task-fMRI, the local noise content is important as much as the difference of noise behaviour across areas (spatial pattern dependence).

3.1.4 FC TOPOLOGICAL FEATURES

To describe the interaction of a node with its surroundings, graph theory offer summary metrics to study the efficiency and hierarchical structure of the identified network, its *connectivity density* (local clustering of nodes), its *small-worldness* features or the existence of few highly-connected nodes which support the network efficiency.

These features could be determined by means of measures like the *clustering coefficient*, node *degree* or *strength*, various notions of *centrality* or *modularity* and whole-graph features like the *characteristic path length* and the *global efficiency*, for a more extensive list of available features see (Guimerà and Nunes Amaral, 2005; Rubinov and Sporns, 2010), in the following only few relevant ones will be described. Observing the neighborhood of all nodes together could instead shed light on the distribution of connections of the graph.

This is reported by the node degree as number of edges in which a node is involved, or strength (also referred as degree centrality (Junker et al., 2006)) of the same node by adding the weights of its neighboring connections. Repeating the evaluation for all nodes (summing the adjacency matrix rows or columns) report to a distribution of degrees on all nodes. A conceptual extension of the *strength* is offered by the *Eigenvector Centrality* (EC) (Zuo et al., 2012) which measures whether strong connections

typically involve similar nodes with strong connections, accounting for indirect pathways as measured by the first eigenvector decomposition of the FC matrix.

The (N-)neighbours of a network node are the nodes that can be reached by crossing at most N edges over the adjacency matrix starting from the node of interest. The clustering coefficient of a node (measuring the local connectivity density) express how the neighbors of a node are interconnected themselves (forming a closed triangle or cycle) indicating the local connectedness degree or figuratively the connection density around such a node.

$$\mathrm{DEG}_i = \sum_{j=1}^{N} \widetilde{\mathrm{FC}}_{\mathrm{ij}} \tag{3.1}$$

$$\mathrm{STR}_i = \sum_{j=1}^{N} \mathrm{FC}_{\mathrm{ij}} \tag{3.2}$$

$$\mathrm{EC}_i = \frac{1}{\lambda_1}\,\mathrm{FC}\;\mu_1 = \frac{1}{\lambda_1}\sum_{j=1}^{N} \mathrm{FC}_{\mathrm{ij}}\;\mu_1\left(j\right) \tag{3.3}$$

$$CC = \frac{1}{n}\sum_{i\in N}\mathrm{CC}_i = \frac{1}{n}\sum_{i\in N}\frac{2t_i}{k_i\left(k_i-1\right)} \tag{3.4}$$

$$d_{\mathrm{ij}} = \sum_{\mathrm{FC}_{\mathrm{uv}}\;\in\,\mathrm{g}_{i\leftrightarrow j}} \mathrm{FC}_{\mathrm{uv}} \tag{3.5}$$

$$L = \frac{1}{n}\sum_{i\in N} L_i = \frac{1}{n}\sum_{i\in N}\frac{\sum_{j\in N, j\neq i} d_{\mathrm{ij}}}{n-1} \tag{3.6}$$

$$SW = \frac{C/C_{\mathrm{rand}}}{L/L_{\mathrm{rand}}} \tag{3.7}$$

where FC here plays the role of the adjacency matrix for clarity of representation: DEG_i represents the degree of node *i*, $\widetilde{\mathrm{FC}}_{\mathrm{ij}}$ the binarized FC matrix connecting node *i* and *j*; STR_i the node strength of node *i*, EC_i the eigenvector centrality of node *i*, λ_1 the first eigenvalue deriving from the decomposition of the FC matrix and μ_1 the associated eigenvector, CC_i

the clustering coefficient of the node i within the neighborhood N with t_i edges within such neighborhood of k_i nodes ($k_i\left(k_i-1\right)/2$ represents the total number of all possible edges) while d_{ij} measure the path length as weighted (topological graph-distance) distance across a path g of edges and L the characteristic path length over N paths of distance d_{ij} among each node i, j (average distance across all possible paths in the graph, also referred as graph diameter), necessary to define the small-worldness SW as ratio of the average CC observed to the CC of a CC_{rand} random equivalent network normalized to the characteristic path length L observed as compared to a L_{rand} random equivalent network.

To describe the nodal centrality, graph theory offers many metrics (e.g. *betweeness*, ...) describing how central a node is based on how many shortest path (of minimal edges crossed or with minimal/maximal total weights of edge crossed) between other nodes pass through the one of interest.

$$\text{BC}_i = \sum_{\forall j,k \neq i} \frac{\sigma_{j \leftrightarrow k,i}}{\sigma_{j \leftrightarrow k}} \tag{3.8}$$

where $\sigma_{j \leftrightarrow k}$ is the number of existent shortest paths from node *j* to node *k* while $\sigma_{j \leftrightarrow k,i}$ correspond to the number of shortest paths passing through the node *i*.

To understand if a node hierarchy exist in the graph that effectively organizes groups of nodes and shape their connectivity at different organization levels, the concept of clustering can be extended to identify groups of nodes with favored connectivity among them compared to others introduced by the notion of *modularity* ((Newman, 2006)) and a sharedness notion dedicated to modular structure describing the strength of participation of a node to the belonging module rather than others (participation coefficient). This metric suggests whether the links of a node are uniformly distributed across all modules rather than are mostly connect-

ing nodes within the same module (Guimerà and Nunes Amaral, 2005).

$$Q = \sum_{u \in M} \left[e_{\text{uu}} - \left(\sum_{v \in M} e_{\text{uv}} \right)^2 \right] \tag{3.9}$$

$$\text{PAR}_i = 1 - \sum_{s=1}^{N} \left(\frac{k_{\text{is}}}{k_i} \right)^2 \tag{3.10}$$

where: Q represents the modularity measure of such graph with a module definition M (i.e. fixed set of modules which segregates all the nodes), e_{uu} the number of within-module edges and e_{uv} the number of between-module edges; PAR_i represents the participation coefficient of node i with k_{is} the total number of edges of node i within the module s while k_i represents the degree of node i (total number of edges interested by node i).

Within this framework it is even clearer the critical role of accurate network modelling at the lower level through careful estimation of the FC matrices because the abstraction layer added by graph modeling could make it challenging to evaluate meaningful results from confounds for example related to spurious edges (Smith et al., 2013b). For an in-depth discussion of graph theory tools refer also to (Wang et al., 2010).

3.1.4.1 Brains network organisation principles associated to the energetic budget

The graph-based approach in brain network analysis has been applied to characterize the global network organization. Many works found substantial topological reorganizations of the brain communication system in response to different states, age (Vidal-Piñeiro et al., 2014), administered task or modulated by stimulation (Fox et al., 2012).

As for economic and social networks, the brain, specifically in resting condition, is organized following a small-world network topology (van den Heuvel et al., 2008). This structure features a high local clustering (high clustering coefficient) and low path length (travel distance between any couple of nodes) (Watts and Strogatz, 1998). This means that

brain communication structure relies on specialized (segregated modules) and distributed information processing for its functioning while balancing the information transfer efficiency and the wiring cost of operating such a network. Nonetheless many brain pathologies were found to sharply alter this balance and property falling into the concept of "connectivity pathologies".

In this context two cost contributions can be distinguished: the cost of wiring and the cost of operating the network (Achard and Bullmore, 2007). Brain wiring cost are due to the fact that brain networks are spatially embedded in a finite volume (intra-cranial space) constraining the density of neurons and shaping their connectivity medium (axon form and size factors, ultimately related to their communication efficiency) and maximal information travel distance. The accepted principle underlying this cost, is assumed to be an increasing function of the wiring volume represented by the amount of neuronal axons to be energetically sustained. Moreover, GM neurons tend to have myelinated axons for long connections with increasingly sparse long-range fashion compared to GM neurons, a sharp phenomenon observing the brain of different animal species whose brain to body size relation was found to follow an allometric scaling law. This was biologically confirmed in mammalian with an increased probability of synaptic connections between closer cells (Kaiser et al., 2009) and similarly, at mascroscopic scale the distance between two brain areas was found to be inversely correlated to both anatomical and functional connectivity (Meier et al., 2016).

3.2 Models for energy metabolism

Glucose is the major energy substrate of the brain, tightly regulated under physiological conditions, although abruptly altered by a variety of pathologies such as stroke, epilepsy and dementia where it is also indicative of cellular loss patterns. The following introduction is based on the work of Magistretti et al. (Magistretti and Allaman, 2015) about the energy utilization at cellular level while the neuroscience perspective was

drawn from Raichle et al. (Raichle, 2006).

Glucose is responsible for the production of energy through different metabolic pathways (i.e. chemical processes): glycolysis and oxidative phosphorylation. Interestingly, the energy budget entailed by these glucose metabolism pathways is adapted to the body condition. For example, a substrate involved in fueling brain activities such as the lactate, typically accounts for 8 to 10% of the energy requirements but can be physiologically up-regulated to 20-25% under prolonged physical activity (Matsui et al., 2017).

Quantitatively, the amount of energy required by the brain under normal condition was found around 20% of the total body energy (Raichle and Gusnard, 2002) despite the weight ratio to the body is around 2%. Consistently, the metabolic processes are fueled also by an amount of oxygen estimated around the 20% of the total oxygen consumption in the body. Overall, around 80% of total energy is attributed to glutamate-mediated neurotransmission while 15% to the resting potential maintenance as confirmed in-vivo by means of Magnetic Resonance Spectroscopy (MRS) targeting glutamate usage. This budget is dominated by neuron cells (80% of the brain energy requirements) while supporting cells of the central nervous system (glial cells that make up nearly half of the brain volume and outnumber the neurons) account for 10 to 15% of the consumption.

3.2.1 The 18F-Fluoro-Deoxy-Glucose (FDG) tracer

While the principle underlying fMRI measurement of neural activity has been covered in the previous Chapter, its biological specificity and hence interpretability is reported to be still limited (Turner, 2016).
While widespread tracing the dynamics of oxygen consumption (local cerebral metabolic rate of oxygen or $CMRO_2$) has been limited by the technical difficulties, the measurement of glucose is currently one of the most clinically prescribed exams to study brain metabolic alterations. The traced molecule consists in the deoxy-glucose labelled by the 18-F

radioisotope (18F-FDG) that is meant to mimic the role of glucose while crossing the BBB and during the phosphorylation but then accumulates without participating any further to the metabolic pathways (Sokoloff et al., 1977b).

The current standard model for cerebral glucose metabolism traced by FDG is derived from the three compartment kinetic model proposed by (Bertoldo et al., 1998; Sokoloff et al., 1977b).

Assumptions underlying this model require a steady state glucose system (see Figure 3.2.1) for the duration of the experiment (often 45-120 minutes (Lucignani et al., 1993)), injected bolus under tracer hypothesis not able to perturb this state implying fixed kinetic parameters governing the glucose exchange between compartments and homogeneous tissue metabolic response in the sampled volume (Bertoldo et al., 1998). The standard uptake value (SUV), corrected for weight or body surface area, plasmatic glucose level and injected dose, provides the experimentally simplest semi-quantitative measure when the investigation is focused on FDG variations rather than the rate constants (Hamberg et al., 1994b).

Careful experimental design further allowed Vlassenko et al. (Vlassenko et al., 2006) to appreciate a measurable FDG uptake increase (+28%) in-vivo after visual stimulation even with very short (compared to the FDG dynamic with time scale around one hour) visual stimulation paradigms of 5 min of FDG uptake compared to previous task application (Friston et al., 1996).

Although simple, the SUV biological interpretation is less clear than compartmental modeling or graphical methods. Considering a steady state uptake period that avoid unstable vascular circulation of the FDG (0-15 minutes post-injection) and measuring the activity at least after 40 minutes post-injection (Sokoloff et al., 1977b) for tracer equilibrium would provide an index consistently associated to CMRGlu (Hamberg et al., 1994b).

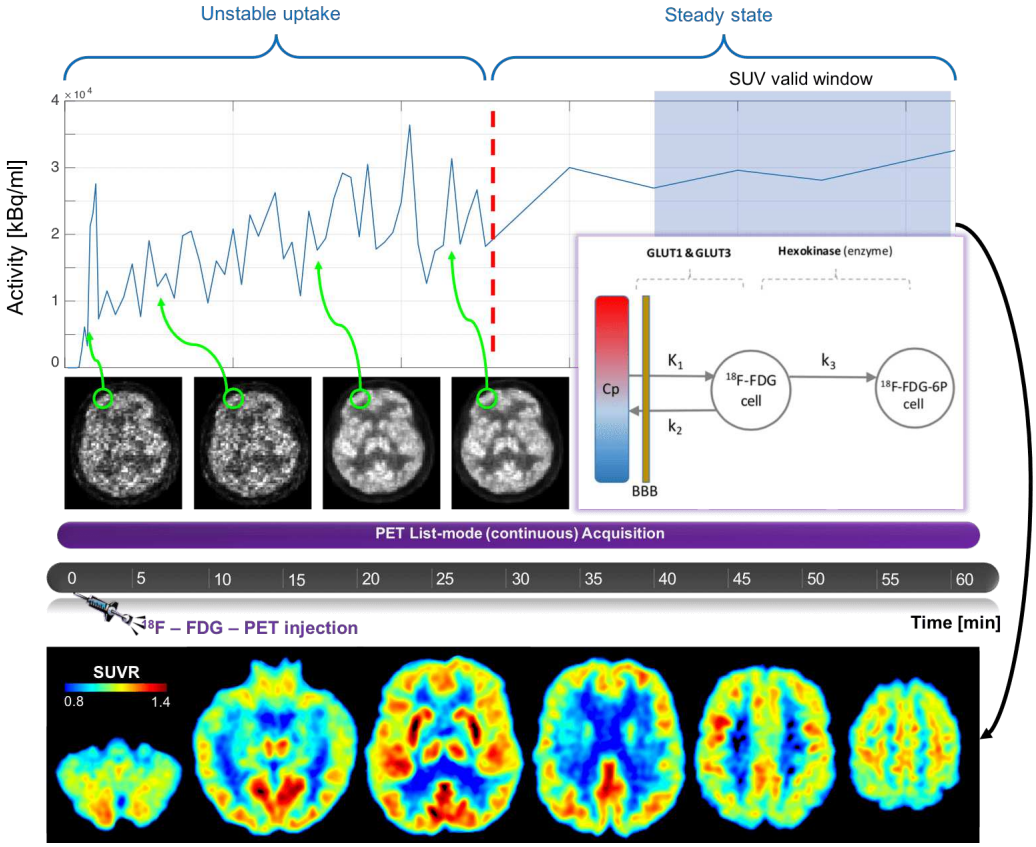

Figure 3.2.1: *Dynamic activity measured during a PET experiment.* After the venous injection of Fluorodeoxyglucose labeled with 18-F (FDG), the activity [kBq] can be collected continuously (list mode scan) for the 60-minutes' duration of the experiment. According to a non-uniform time grid (finer at the beginning while coarse after 30/40 minutes) the measured activity [kBq/ml] can be 3D reconstructed in associated volumes as depicted in figure. After an initially increasing activity period (region dependent, 30-40 minutes in average), the dynamic activity reaches a stable trend (steady state period) where the standard uptake value can be calculated by summation of the activity in the desired frame normalized by injected dose [Bq] and usually body weight [Kg]. The dynamic trend can be modelled according to the 3K compartmental model depicted in the right box. The SUV relative to the cerebellum has been obtained from the 40-60 min window of the dynamic activity curve and reported in the bottom section for a set of transversal slices encompassing the whole brain SUVR distribution for a typical healthy subject (M, 56 yrs).

The SUV, often referenced to a pre-determined brain area or the global uptake (referred as SUVR), could be suitable for studies based on FDG contrast differences to monitor FDG variations caused by pathology, pharmacological treatment and sensory-motor tasks not expected to alter globally the FDG balance of the brain again without offering a biologically clear and quantitative information (Hamberg et al., 1994b).

3.3 Brain network organisation and glucose metabolism together: hybrid PET-MRI scanners

Previous studies reported a significant intra-subject variability affecting FC-fMRI and FDG-PET (Cecchin et al., 2017).
This variability stems from the nature of fundamental brain processes such as the metabolism, neuronal activity that are both space and time dependent therefore independent experimental methods aimed at describing the functional activity (or coactivity in FC) and metabolism need to necessarily probe the brain under matched physiological conditions for an unbiased matching.

Quantitatively these sources of variability have been estimated in healthy subjects as high as 10% of coefficient of variation (CV) of local CMRGlu (Maquet et al., 1990) while the scan-rescan variability has been reported typically in the order of 10% of CMRGlu (intra-subject) or typically less than 20% between-subjects. Even if not statistically significant, the average CMRGlu cortical variability has been estimated in $7.9 \pm 15.5\%$, comparatively at the same order of magnitude of intra-subject variability, testifying how the CMRGlu variability can certainly reach and potentially mask physiological differences of metabolism between brain areas.

Likewise, FC based on BOLD contrast can be severely affected by any modifying aspect of cerebral hemodynamic response such as perfusion alterations, age, sex, respiratory characteristic or motion content variability. To note is that the impact on FC also depends on the cognitive and behavioral state of the subject during the measurement where the intra-subject variability can explain, in a typical fMRI experiment, between

40 and 60% of the total observed variance (as the sum of the within-subject and between-subject variability) (Chen et al., 2015). Moreover, scan-rescan reliability of fMRI measures as well as network-level connectivity was found under 0.6 in terms of intra class correlation coefficient (ICC) (Chen et al., 2015).

Indirect interaction between these confound can also happen as recent literature results reported a close relationship between the pattern of perfusion and structural RSNs alterations in the default mode or executive control networks (Liang et al., 2012) while ipo-perfusion has been previously associated to a decreased FC amplitude.

Preclinical studies on small animals (Wehrl et al., 2013) made first use of the simultaneous approach to demonstrate partially, although, limitedly consistent pattern of task-evoked fMRI activity and FDG-PET in rats.

The relation between metabolism and brain functional organization was soon explored in healthy humans by (Aiello et al., 2015) who observed a limited similarity between spatial patterns of functional and glucose metabolism through voxel-wise correlation analysis. Specifically, the fMRI local connectivity based on regional homogeneity (ReHo) and the amplitude of low frequency fluctuations (ALFF) (Lv et al., 2018) were found to be significantly associated (Spearmans $\rho > 0.7$ over significant voxels) to FDG-PET derived glucose consumption while network-level features such as the degree of centrality were less clearly explained in terms of metabolism leaving open questions on how the BOLD response depends on oxygen demand variability or local glucose consumption.

Based on an often hypothesized relation between local neuronal activity and functional coupling in neural computational modeling, (Riedl et al., 2014) investigated the local relationship between neural activity (probed by FDG-PET) and connectivity observing an increased glucose metabolism in the visual system and the salience network (corresponding to cingulate and insular cortex) correlated with the spatial pattern of increased connectivity across areas within such networks.

Refined modelling of local functional connectivity in terms of density

(lFCD) (Tomasi et al., 2013) lead to additional evidence about the FC relation to changes of glucose metabolism across brain states.

Despite the incomplete literature agreement, first clinical application of the concept has been proposed by (Tahmasian et al., 2016) who successfully employed FC voxel-wise degree centrality along with glucose metabolism to enhance the classification of Alzheimer disease from Frontotemporal-lobar degeneration patients as compared to the separate modalities.

4

The relation between resting-state functional connectivity and glucose metabolism

4.1 Introduction

Thus far, neuroscientists demonstrated that the brains communication across macroscopic, functionally homogeneous areas, is an highly efficient structure for information exchange whereas graph-based modelling of such a network, revealed an active balance maintained between functional segregation and information integration across multiple brain areas (Deco et al., 2015; Sporns, 2013) leading to the late concept of functional connectivity (FC) (Friston, 2011).

Many of these studies, based on the temporal covariance exhibited by the blood-oxygen-level-dependent (BOLD) signal in different brain areas, revealed the existence of interacting whole-brain functional networks whose altered connectivity pattern has been observed in a wide

range of pathologies (Dennis and Thompson, 2014; Woodward and Cascio, 2015), often associated to sharp metabolic alterations as in dementia (Peraza et al., 2014) and Alzheimer's disease (Scherr et al., 2018).

As described a previous Chapter, the brain energy demand is remarkably related to its functional operation. However, the spatial variability of brains glucose metabolism has received limited attention under physiologic conditions (i.e. healthy subjects) while much more emphasis has given to its focal alterations during pathology.
To cover this neglect, the brains glucose metabolism and physiologic significance of its spatial variability was here considered on a macroscopic scale and from the functional perspective ot investigate the eventual association among relevant functional network features and the underlying glucose metabolism.

4.2 Materials and Methods

4.2.1 Data and Imaging protocols

A dataset of 28 healthy subjects was assembled merging 11 subjects (8 males, 3 females; 52.2 10.4 years) as from (Riedl et al., 2014) (referred as: dataset A - Munich) and 17 (6 males, 11 females; 64.7 7.9 years) from (Aiello et al., 2015) (referred as: dataset B - Naples). All subjects were scanned in eyes-open condition simultaneously collecting 18F-FDG-PET (30 minutes post-injection with at least 10 minutes of saturated list mode), rs-fMRI data (at least 7.6 minutes, TR approx. 2 s, voxel-size 3 to 4 mm), and a structural image (1mm isotropic voxel).

4.2.2 Data Analysis

Considered the similar age range and 18F-FDG-PET/fMRI imaging protocol, all subjects were identically pre-processed to obtain local glucose metabolism measures (18F-FDG-PET data) and FC measure (rs-fMRI data) implementing a processing pipeline similar to (Glasser et al., 2013).

4.2.2.1 Structural image pre-processing

Structural T1w images were corrected for field bias (Tustison et al., 2010), skull stripped as in (Tustison et al., 2013), and segmented into gray/white matter and cerebrospinal fluid. A second stage of intensity normalisation was then applied by estimating the intensity bias from the segmented white matter. The final brain mask was obtained applying the routine antsBrainExtraction (ANTs) (Tustison et al., 2013) whereas cortical surface delineation and region segmentation was obtained running Freesurfer (recon-all volume and surface reconstruction pipelines (Dale et al., 1999; Fischl et al., 1999)on bias field corrected T1w image.

Manual editing of the cortical surfaces obtained from the pial and white matter segmentations was performed to correct for gross delineation errors. Pial and white matter surfaces were finally resampled over the fs_LR surface mesh, provided in the Conte69 atlas (a surface mesh of 164,000 nodes, symmetrically distributed in hemispheric correspondence, that was subsequently down sampled to 32000) to define the cortical representation space ($32k\_fs\_LR$) used in this study. The Gordon-Laumann (GL) functional atlas (Gordon et al., 2016) was applied to parcel $32k\_fs\_LR$ (defined by approx. 32000 mesh vertices) surface meshes into 333 cortical regions, integrated with 18 gray matter subcortical regions as provided by FreeSurfer.

The spatial distance among macroscopic brain regions was evaluated by means of Euclidean distance (ED) (Supekar et al., 2009), obtained in each subject, between the parcels centre-of-mass, which was then normalised by the ED median value across parcels in each subject, and then averaged across subjects to provide a normalized group-wise measure of inter-areal distance.

4.2.2.2 Functional image pre-processing

The first four images of each fMRI run were discarded to avoid non-equilibrium effects of magnetization. The volumes were then corrected for slice timing differences (Jenkinson et al., 2012; Smith et al., 2004) and

motion (mcflirt, FSL with normcorr cost function and 12 degrees of freedom) in reference to the median volume. An EPI reference image suitable for co-registration to the structural one was then obtained with ANTs (Avants et al., 2011). An affine registration was estimated with flirt tool of FSL between this EPI template and the processed T1w image, which was used to resample the segmentations of subcortical regions, WM and CSF (nearest neighbour approach) from T1w to EPI space.

A number of nuisance regressors were then removed from the fMRI timeseries: motion and first order derivatives, the first five components obtained by principal component analysis that explained 70% variance (with decreasing explained variance order and typically in all subjects) of WM and CSF fMRI signals (*compcor* (Behzadi et al., 2007)) and cosine high-pass filter basis (frequency cut-off = 0.009 Hz). Confound-regressed fMRI timeseries were finally resampled over the $32k_fs_LR$ surface mesh (flirt routine, FSL; connectome workbench tools (Marcus et al., 2011)). The resampled data was averaged across surface mesh nodes corresponding to the same parcel as defined by the GL atlas.

The parcels were grouped in networks: visual (VIS), retro-splenial-temporal (RSPT), sensory-motor hand (SMH) and mouth (SMM), auditory (AUD), cingulo-opercular (CON), ventral attention (VAN), dorsal attention (DAN), salience (SAL), cingulo-parietal (CP), fronto-parietal (FPN), default mode (DMN), and unassigned regions (None). The subcortical (SUB) regions, as provided in FreeSurfer T1w space (Fischl et al., 2002), included bilateral Caudate, Putamen, Accumbens, Pallidum, Amygdala, Hippocampus, Thalamus, Ventral diencephalon, Cerebellum cortex. Overall, 333 functional time courses for cortical parcels and 18 for subcortical regions were obtained for each subject (total n=351). Weakly represented parcels or consisting of less than 10 mapped voxels (Gordon et al., 2016) were discarded obtaining 347 usable parcels in each subject.

The BOLD spectral content was quantified by the amplitude of low frequency fluctuations (ALFF), i.e. the power of the signal within [0.01, 0.1] Hz band), and the fractional ALFF (fALFF), i.e. the power within the low frequency range [0.01, 0.1] Hz, divided by the total power in the entirely

detectable frequency range. The local signal coherence was measured with the Regional Homogeneity (ReHo) (Song et al., 2011), computed as Kendalls coefficient of concordance (Kendall, 1938) for the signal between each voxel and its neighboors. These BOLD signal metrics were defined in each parcel and averaged across subjects.

4.2.2.3 FC ESTIMATION AND GRAPH ANALYSIS

Functional connectivity (FC) matrices were obtained by Pearson's cross-correlation of the 347 fMRI time series, subsequently Fisher z-transformed. Motion-corrupted time points of each fMRI run were identified by frame-wise displacement (FD) (Power et al., 2014), and discarded before FC estimation using an FD threshold of 0.3 mm. FC matrices from subjects in dataset A and B were averaged and compared, then combined for analysis across datasets. For graph computations, FC matrices (van Wijk et al., 2010) were binarized by preserving only connections with associated weights above the 80^{th} percentile of FC weight distribution, corresponding to a sparsity level of 20%.

The adjacency structure described by each FC matrix was summarized by its formal topological properties using routines part of the Brain Connectivity Toolbox (BCT) (Rubinov and Sporns, 2010) as implemented in Matlab (ver. 2016b, The Mathworks, Natick, MA). The connectivity of each node can be represented (Sporns et al., 2007) by the number of its discrete connections (node degree, DEG), and the sum of FC weights of all nodal connections (node strength, STR). To measure a nodes centrality we used the eigenvector centrality (EC) and (Lohmann et al., 2010) betweenness centrality (BC) (Freeman, 1977). Local connectivity structure (Rubinov and Sporns, 2010) was also explored using the clustering coefficient (CC) and the local efficiency (LE) metrics.

Brain networks are organised in modules. Here the modularity structure was either defined according to putative RSNs (i.e. atlas derived (Gordon et al., 2016)) or identified by optimising the Newman's modularity (Girvan and Newman, 2002; Newman, 2006) using the Louvains

approach (Blondel et al., 2008; Rubinov and Sporns, 2010; Sporns and Betzel, 2016) implemented in BCT (Rubinov and Sporns, 2010).
Such an optimisation was separately carried out over a range of module resolutions ($\gamma = 0.9 - 1.75$) to encompass different network organisation levels in order to detect possibly different glucose metabolic interactions at different organisation scales. Given the modularity structure, the participation coefficient (PAR) (Guimerà and Nunes Amaral, 2005) was finally used to measure the proportion of each node's connections that are part of the same module or that are part of different modules; finally, the versatility coefficient (VER) (Shinn et al., 2017) measured how strongly a node was affiliated to a specific module as compared to other modules.

4.2.2.4 PET DATA PROCESSING

18F-FDG-PET images in saturated list mode were resampled in T1w space (flirt, FSL) and normalized by the whole-brain 18F-FDG average uptake (Byrnes et al., 2014), obtaining a relative standard uptake value (SUVR) image for each subject. SUVR images were sampled over the cortical surface ($32k\_fs\_LR$), and mean SUVR values for each cortical (atlas-derived (Gordon et al., 2016)) and subcortical (previously delineated) parcels were obtained. The impact of partial volume effect (PVE) on 18F-FDG-PET data was evaluated separately defining the parcel SUVR value as the 50^{th}, 75^{th} or 90^{th} percentile of the SUVR distribution and meant to provide parcel-representative SUVR values variably affected by PVE. Further analysis and considerations regarding SUVR will consider parcel values obtained by sampling the local SUVR distribution at the 90^{th} percentile, observed to be the most robust estimate across subjects that minimized PVE.

4.2.2.5 DATASETS COMPARISON ANALYSIS

To establish the agreement of SUVR and FC estimates provided by the two dataset, we performed a paired comparison, separately for 18F-FDG-PET and fMRI data whose results are summarized the supplementary

section 4.6.1. The 18F-FDG-PET agreement consisted in a linear regression analysis to check the consistency of SUVR across corresponding parcels between the two datasets, separately carried out considering age and sex covariates prior to the intra-dataset averaging. The statistical significance of such a difference was investigated with a paired two-tail t-test (0.05 level, Bonferroni corrected across parcels), separately performed by varying the cortical sampling depth of the parcel SUVR to highlight PVE issues for dataset agreement.
The agreement between fMRI measures in the two dataset was performed to ensure similar BOLD signal properties and FC structural consistence. Spectral and local homogeneity of BOLD signal (ALFF, fALFF, ReHo) (Aiello et al., 2015) were compared at the group level with a linear regression analysis across corresponding parcels. The inter-subject variability of these measures was evaluated intra- and inter-dataset with the coefficient of variation (CV%), defined as the standard deviation divided by the average across subjects in percent.
The similarity at the parcel level of the FC matrices in the two groups of subjects was determined by linear regression analysis and statistical comparison (Wilcoxons rank sum, 0.05 significance level) of pairwise parcel FC weights. Since there is limited data in the literature on the similarity of FC matrices in different groups of subjects, we examined this issue by computing similarity in randomly split datasets (1000 permutations), and evaluating linear agreement level by the amount of variability accounted for (R^2).

4.2.2.6 Metabolic consumption of different RSNs

Since RSNs form an important organizational feature of fMRI FC, we first tested if different networks show different metabolic consumption. This was tested with a non-parametric ANOVA (Kruskal-Wallis test on median SUVR differences, 0.05 significance level) after averaging within each network across parcels. Post-hoc comparisons were carried out between pairs of networks with a Wilcoxon rank sum test (FDR with 0.05

rate across post-hocs (Benjamini and Hochberg, 1995)). A similar analysis was carried out on the variability of the SUVR values across different RSNs.

Visual inspection of the scatter plots of SUVR values by network showed that in each RSN it was possible to have both metabolically expensive or inexpensive nodes, but that the relative distribution varied by network. To determine which networks were significantly enriched in metabolically expensive or non-expensive nodes, we measured the proportion of high/low SUVR nodes within a RSN as compared to a random set of nodes forming a random RSN of the same size.

A null distribution of the expected proportion of high/low SUVR values in a random set of nodes was generated by repeating the same procedure 50000 times. Significance was determined by counting how many times SUVR values of the null distribution were more extreme (respectively higher or lower) than high-SUVR and low-SUVR values measured from the RSN of interest after normalizing for the number of repetitions.

A network was significantly enriched in low/high SUVR nodes if the number of extreme values in the null distribution occurred less than 5% of the times ($p < 0.05$) Bonferroni corrected for the number of networks tested. The analysis was run at different criteria of high and low-SUVR values by decreasing or increasing the percentiles of the SUVR distribution (respectively from 50^{th} to 10^{th} or from 50^{th} to 90^{th} percentiles), and results were evaluated at different cut-offs.

4.2.2.7 Metabolic similarity of functionally connected regions

Once we measured the similarity of the two datasets in terms of BOLD signal (spectral properties, local and global functional connectivity) and SUVR, we were interested in relating FC properties to glucose consumption. In a first analysis, we reasoned that if the connectivity profile of a node (i.e. its FC with other nodes) were not related to its glucose metabolism, then functionally similar nodes will not show similar glucose metabolism profiles. In other words, nodes with stronger FC will

show the same metabolic homogeneity than a randomly sampled group of nodes. Conversely, if functionally connected nodes have lower glucose metabolic variability than random nodes, then we can conclude that FC has an influence on glucose consumption. In this study, two nodes were considered functionally similar if their FC profile was correspondingly similar.

This hypothesis was investigated as follows: (1) nodes were hierarchically clustered according to their functional profile similarity (Ward hierarchical clustering of connectivity distance (Smith et al., 2011)); (2) the full node set was randomly clustered (without replacement) using the same number and size of the clusters determined in step 1; (3) glucose metabolism variability was estimated calculating the SUVR variance intra-cluster, averaged across clusters, separately for random (step 2) or functionally-derived (step 1) clusters.

Step 2 was repeated 50,000 times for random set of nodes yielding clusters of the same number and size as those functionally defined. The significance level of intra-cluster metabolic homogeneity obtained on functional clusters (step 1) was compared to that obtained from random clusters (step 2) by counting how many times the random (null) distribution had lower SUVR variance than the SUVR variance obtained from the functional clusters, after normalizing for the number of repetitions. The level of significance was adjusted to $p < 0.05$. This analysis was repeated cutting the hierarchy tree (step 1) at increasing height, thus decreasing the number of clusters from 15 (consistent to the typical number of RSNs) to 2 (consistent with a macroscopic network categorization in intrinsic vs. extrinsic networks as defined in (Doucet et al., 2011; Hacker et al., 2013; Thomas Yeo et al., 2011).

This analysis of similarity of FC and glucose consumption across multiple nodes/modules was also performed using in step 1 clusters defined based on the GL atlas-derived RSNs.

4.2.2.8 FC WEIGHTS AND GRAPH PROPERTIES VS. GLUCOSE METABOLISM

We tested the linear association between graph properties of functional connectivity (DEG, STR, CC, LE, BC, PAR, VER) and glucose metabolism (SUVR) across nodes. A backward stepwise regression (significance level 0.05) was then applied to detect which graph feature was significantly explaining SUVR across nodes. Each connection was also labelled as within- or between-network and according to inter-areal distance (considered short or long range connection respectively if the Euclidean distance fell above the 75^{th} percentile or below the 25^{th} percentile of the overall ED distribution) to separately evaluate whether these link features, once summarized in terms of functional features, were singularly more clearly related to the nodal SUVR.

4.2.3 GLUCOSE METABOLISM IN HUB NODES

As observed in other real-world networks, the brains network structure exhibit a long-tailed degree distribution, suggesting that few nodes referred as hubs have a very high degree and play a fundamental role in maintaining network efficiency (van den Heuvel and Sporns, 2013a). HUB nodes are not defined based on a single feature, but different features highlight different properties of hub nodes in a network (van den Heuvel and Sporns, 2013a), which may be relevant for their metabolic behaviour.
We considered the connectivity level (DEG (Buckner et al., 2009)) to detect hubs nodes. Candidate hubs were selected among the nodes with DEG level exceeding a set threshold, defined as a linearly increasing percentiles (2.5^{th} to 97.5^{th}) of the overall feature distribution.

The metabolic behaviour of selected HUBs was studied associating their STR and SUVR, separately discussing their network role to highlight whether HUBs primarily involved in few modules (provincial, characterized by low PAR) are metabolically different than HUBs that link many modules (connectors, characterized by high PAR) as well as the

role of inter-HUB connectivity and distance. To test if the STR-SUVR association in HUBs was significantly higher/lower compared to other network nodes, for each selection criteria, we compared the STR-SUVR correlation (Pearsons linear correlation) with the same measure obtained over a random subsample of nodes (i.e. not necessarily HUBs, 5000 repetitions). The significance was evaluated respectively counting how many null distribution occurrences of STR-SUVR correlation are lower/higher than the observed for HUBs (FDR corrected with 0.05 rate across selection thresholds and separately for each HUB criteria).

4.3 Results

4.3.1 Spatial distribution of glucose metabolism

The typical spatial distribution of glucose metabolic activity in the human brain assessed by 18F-FDG-PET SUVR is depicted in Figure 4.3.1. Point-wise SUVR (Figure 4.3.1-A) can be parceled according to a functional atlas (GL atlas) resulting in the map shown in Figure 4.3.1-B for cortical areas and Figure 4.3.1-C for subcortical areas. From the medial view, SUVR was bilaterally higher than the brains average in the posterior and anterior medial regions of cortex including medial occipital cortex, cuneus, retrosplenial cortex, precuneus, and pregenual cortex. From a lateral view, high SUVR regions include middle and inferior frontal gyri, intraparietal sulcus, and superior temporal gyri. Subcortical nuclei and cerebellar regions showed high SUVR (respectively highest in thalamus, caudate, putamen), comparable to those of the most metabolically active cortex regions (Figure 4.3.1-C). Low-SUVR areas included pre- and post-central regions and anterior temporal lobes (represented in blue and brown at the bottom of Figure 4.3.1-A).

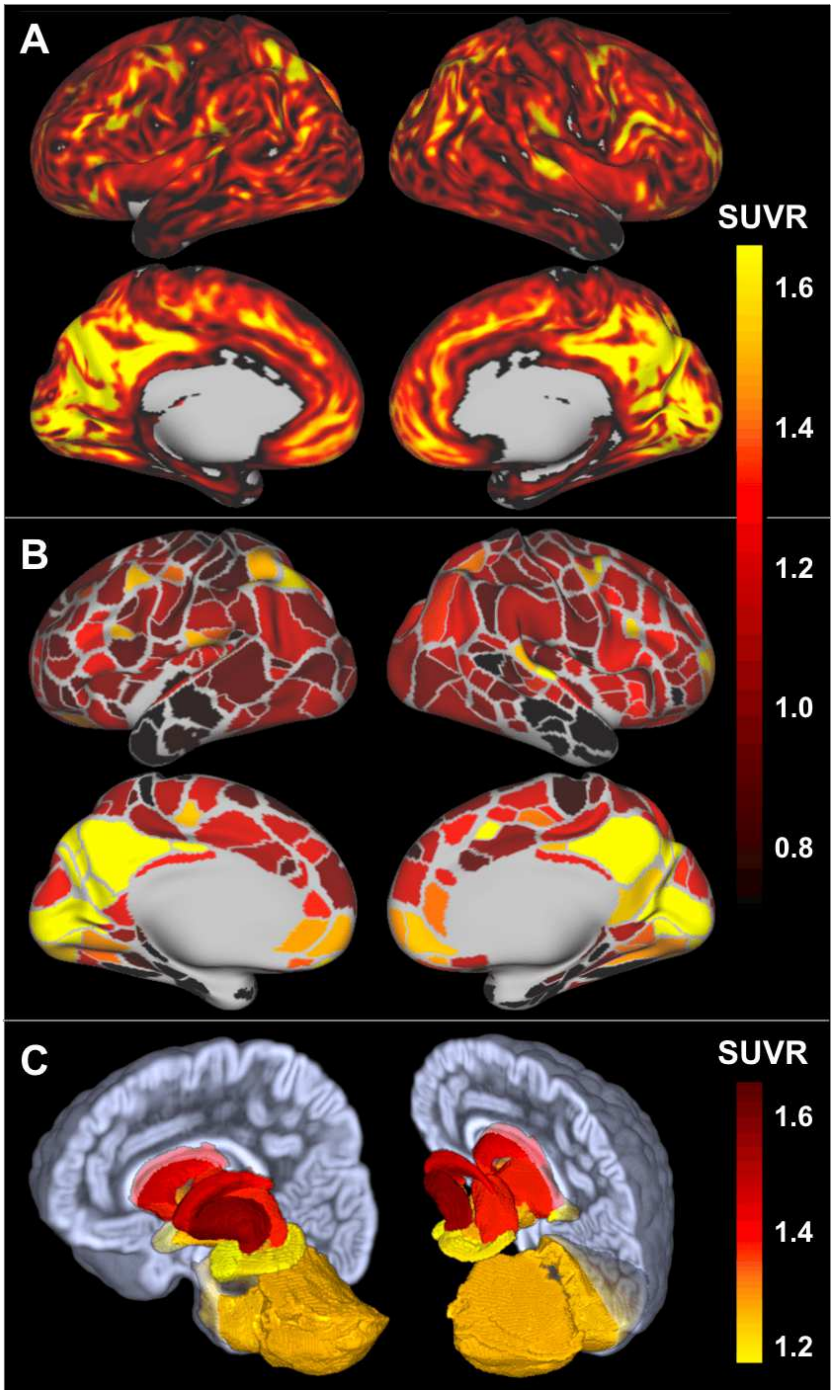

Figure 4.3.1: Distribution of glucose metabolic activity in the human brain. A) SUVR distribution on cortical Freesurfer surface; B) SUVR distribution mapped on parcels of GL atlas; C) SUVR distribution in subcortical nuclei and cerebellum.

4.3.2 METABOLIC FEATURES OF HUMAN RSNS

A non-parametric ANOVA (Kruskal-Wallis test, $degreeof freedom-dof = 13, X = 87.1, p = 5 \cdot 10^{-13}$) suggested that different RSNs (Gordon et al., 2016) have significantly different SUVR. This difference was significant even omitting areas of None network (uncertainly mapped as close to discontinuities of magnetic susceptibility) and SUB networks (Kruskal-Wallis test, $dof = 11, X = 58.7, p = 1.6 \cdot 10^{-8}$). The median of SUVR by network was not significantly correlated to the network size or the networks average spatial extent (Spearmans correlation, $p > 0.05$). As shown in the box plots of Figure 4.3.2-A, most of the RSNs have consistently similar SUVR except for CP and None, respectively having elevated and decreased values. This was confirmed with a post-hoc comparison of SUVR among RSNs (Wilcoxon rank sum, FDR corrected at 0.05 rate across multiple tests) showing significantly higher SUVR in CP and FP networks (Ranksum test, $p < 0.02$).

As represented by red stars in Figure 4.3.2-A, FPN, SMH, VIS, CON, DMN networks exhibit outliers SUVR values. In the DMN, these bilaterally corresponded to the posterior cingulate cortex exhibiting among the brains highest metabolic rates while other DMN parcels did not have high SUVR. Parcels with high SUVR (Figure 4.3.2-B top rows, over the 75^{th} percentile of the overall SUVR distribution) were part of the medial VIS network, DMN and CP in corresponding of posterior cingulate and ventromedial prefrontal cortex, and FPN, DAN, CON parcels in correspondence of lateral prefrontal/insula and intraparietal. Low SUVR (Figure 4.3.2-B bottom rows, under the 25^{th} percentile of the overall SUVR distribution) was instead observed in pre/post-central regions of the SMM and SMH, and None parcels.

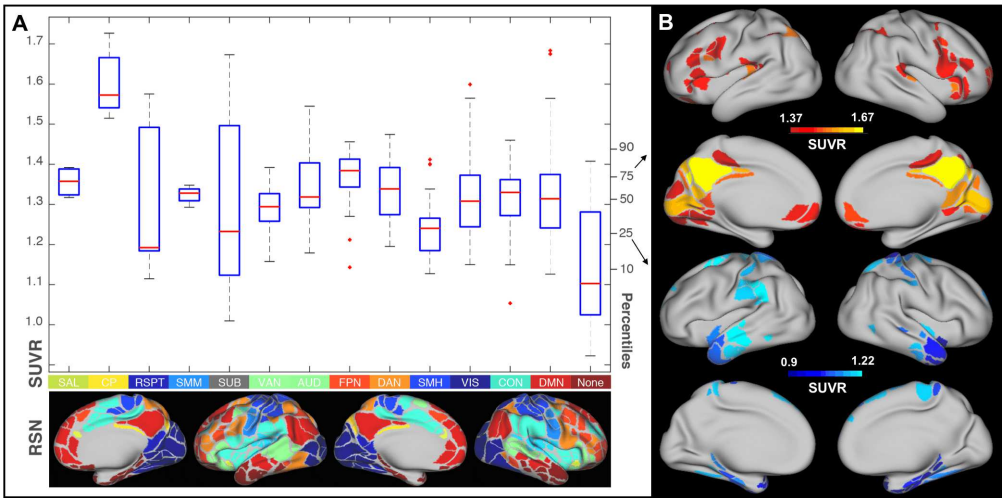

Figure 4.3.2: SUVR distribution by network. A) Boxplots representing the SUVR in different networks (above) as referred by label, sorted by network size (number of nodes). Red line indicates the network-wise SUVR median, the blue box reports the inter $25^{th} - 75^{th}$ percentile range and external SUVR values are reported as red whiskers. Spatial representation of associated networks (color-coded as the cortical surface representation). B) Spatial representation of high and low SUVR cortical areas (respectively identified as: $SUVR > 75^{th}$ or $< 25^{th}$ percentile of the SUVR distribution). Left column represent areas for the left hemisphere first with lateral then medial view, the right column give same presentation for the right hemisphere. C) SUVR distribution in subcortical nuclei and cerebellum.

4.3.2.1 The metabolic activity baseline determined by the network function (intrinsic/extrinsic differences)

In resting condition, the role of putative RSNs for example distinguished in sensory-motor or cognitive can entail adaptive mechanisms and explain network consumption variability. Extrinsic networks (DAN, VAN, VIS and SM, blue parcels in Figure 4.3.3-A) had significantly lower SUVR (Ranksum test, $p < 0.05$) than intrinsic ones (FP and DMN, red parcels in Figure 4.3.3-A) following the separation proposed in (Hacker et al., 2013), further represented in Figure 4.3.3-B.

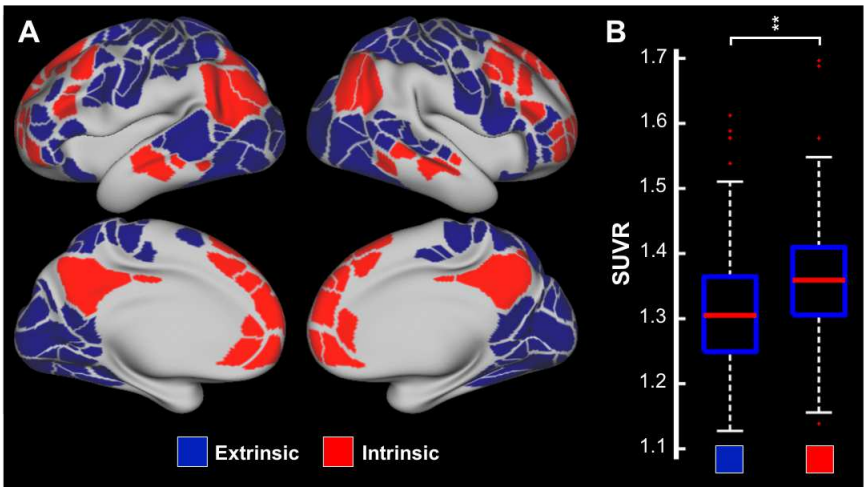

Figure 4.3.3: Representation of extrinsic (DAN, VAN, VIS, SM; depicted in blue) and intrinsic (FP, DMN; depicted in red) resting state networks in box (A) along with comparative distribution of the SUVR in these two network categories in (B). Statistical significance of two-tailed median difference between network categories is reported by ** ($p < 0.05$).

4.3.2.2 Metabolic enrichment analysis

Figure 4.3.4-A shows the distribution of SUVR values over all brain parcels. This distribution was thresholded at different percentiles to determine the RSN-level enrichment of high/low SUVR parcels. As depicted in Figure 4.3.4-B, the proportion of low SUVR parcels was statistically significant in RSPT, SMH, None and Sub networks consistently across differ-

ent percentile levels. High SUVR parcels were instead more consistently observed within CP, FPN, DAN, SAL, DMN networks (Figure 4.3.4-C) eventually supporting a more central roles related to higher cognitive functions while less involved in sensory and motor activities.

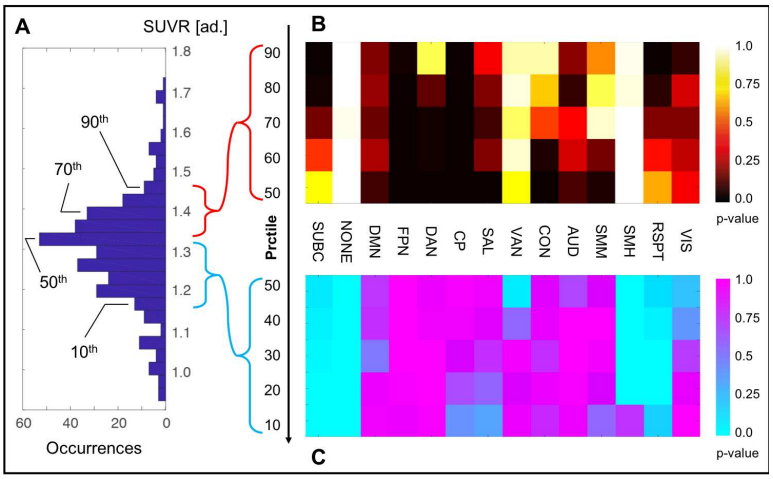

Figure 4.3.4: Network SUVR enrichment analysis. A) Frequency distribution of SUVR values across parcels, and percentiles of SUVR values. B) High SUVR enriched networks from 50^{th} to 90^{th} percentile of SUVR value distribution: network parcels with significantly higher SUVR values, as compared to random parcels (Yellow to Black). Networks with no significant enrichment (White). C) Low SUVR enriched networks from 10^{th} to 50^{th} percentile of SUVR value distribution: network parcels with significantly lower SUVR values, as compared to random parcels (Cyan-Teal). Networks with no significant enrichment (Magenta-Pink).

4.3.3 Node connectivity entails glucose metabolic activity

We found a positive linear association between glucose metabolic activity and nodal connectivity across nodes. Connectivity assessed by DEG, STR and EC features obtained from the group-average FC were significantly correlated to SUVR (Table 4.3.1, column 1 and 3). A lower but significant correlation was also found using a non-linear (Spearman rank) association metric in place of Pearson correlation (Table 4.3.1, column 2 and 4). Increasing the sparsity level used to binarize and calculate the node DEG was found to provide a progressively less consistent (from Pearson

$r = 0.35$ with clear significance to Pearson $r < 0.1$ with no statistical significance) association of DEG with SUVR when increasing the sparsity level from 70% to 99% (preserving 30% to 1% of strongest FC edges).

Graph metric	(P) r	(S) r	(P) r (wo None)	(S) r (wo None)
Degree (DEG)	0.35**	0.29**	0.16*	0.13*
Strength (STR)	0.40**	0.31**	0.23*	0.17*
Eigenvector Centr. (EC)	0.35**	0.27**	0.15*	0.11

Table 4.3.1: Association between local metabolic glucose consumption (SUVR) and connectivity graph metrics (Node degree, strength, eigenvector centrality). P: Pearson correlation, S: Spearman ranks correlation are evaluated both considering all 347 nodes or omitting None group (without None). Significance reported as: * $p < 0.05$ and ** $p < 10^{-6}$.

The clearest linear association, observed between STR and SUVR ($r = 0.40, p < 10^{-6}$), was not dependent on spatial distance. In fact, regressing out the Euclidean distance from FC amplitude before the STR evaluation limitedly affected the STR-SUVR association.

The limited linear association amplitude among STR and SUVR was clarified in Figure 4.3.5-B highlighting the presence of many outlier from the main trend. Most of them, responsible for lowest STR values, belong to the None group of functionally unassigned areas (lower frontal and lower temporal positions) while in the high-SUVR range ($SUVR > 1.5$) a pool of outliers instead had a lower STR than expected from their SUVR ($50 < STR < 70$) and were localized in posterior cingulate cortex (DMN, RSPT), visual (VIS) and subcortical (SUBCORT) networks.

The STR evaluated considering between-network edges was significantly related to SUVR (Pearson $r = 0.41, p < 0.01; SUVR = 1.1 + 0.0037xSTR, R^2 = 0.17$) in agreement with (Castrilln et al., 2016) while a borderline significant relation was observed regarding intra-network edges (Pearson $r = 0.15, p = 0.045$). Similarly, the STR evaluated considering only short-range connections was significantly associated with SUVR (Pearson $r = 0.44, p < 0.01$) as compared to long-range ones (Pear-

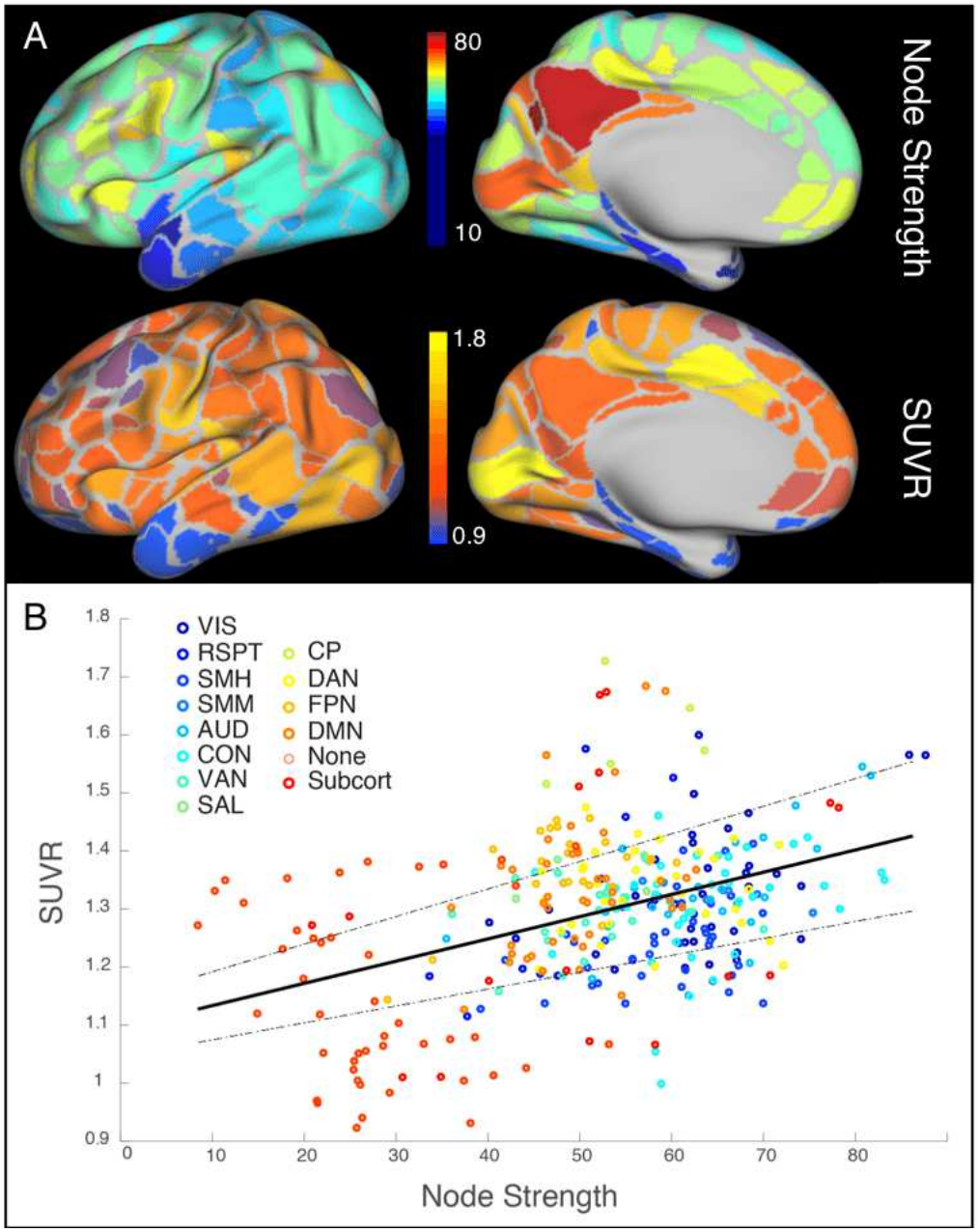

Figure 4.3.5: Metabolic and functional spatial correspondence. (A) Representation of group-wise node strength (above) and SUVR (below) at each parcel over an inflated cortical surface for the left hemisphere of GL atlas (right hemisphere and subcortical areas omitted). (B) Scatter plot depicting the global (all ROIs) linear association between SUVR and node strength (FC summed by column). Linear least square regression line (black plain) and 95% confidence intervals on regression slope (black dotted) reported in overlay. Network nodal membership is highlighted using different colours for each network (see relative color-coded legend).

sons $r = 0.16, p = 0.05$). Taken together, these results suggests that the observed STR-SUVR association was mostly mediated by between-network and short-range edges. As reported in Table 4.3.2, regressing out the Euclidean distance from the FC weights, before evaluating any node connectivity metric, lowered but not completely resolved the observed association with SUVR.

Graph metric	Full FC	FC - Distance regressed
Degree (DEG)	0.35**	0.30**
Strength (STR)	0.40**	0.37**
Eigenvector Centrality (EC)	0.35**	0.22**

Table 4.3.2: Distance effect on FC. Variability due to edge-wise Euclidean distance over the association between relevant nodal connectivity metrics (Node degree, strength, eigenvector centrality) and the relative SUVR (* $p < 0.05$; ** $p < 10^{-6}$).

4.3.3.1 Per-network metabolic association

The STR-SUVR association observed over all nodes was network-dependent. The functional-metabolic association (Table 4.3.3), once corrected for multiple comparisons, held only in VIS, SMH, AUD and FPN networks (Pearson $r > 0.4, p < 0.01$) while DMN and RSPT had borderline association significance. Network size and average spatial extent were not related to STR-SUVR correlation (respectively: $r = -0.05, p > 0.05; r = -0.3, p > 0.05$) at network-level.

4.3.4 Functionally similar nodes are metabolically similar

Aiming to a more general relationship between glucose metabolism and functionally connected regions based on the actual network organisation. We hypothesized a link between the connectivity profile of a region, i.e. its FC with all other regions (nodes), and its metabolic consumption. Specifically, regions with similar connectivity profiles shall have lower variability of SUVR than randomly selected groups of regions. Such a

Network	Network size	r(STR-SUVR)	Network	Network size	r(STR-SUVR)
VIS	39	0.42*	SAL	4	0.33
RSPT	8	0.8	CP	5	0.25
SMH	38	0.42*	DAN	32	-0.006
SMM	8	-0.42	FPN	24	0.54*
AUD	24	0.67*	DMN	41	0.36
CON	40	0.21	None	45	-0.14
VAN	23	0.33	SUBC	16	0.31

Table 4.3.3: Network-wise functional-metabolism association. The network size expressed as number of regions per network is consistently reported. Values in bold define: $p - value < 0.1$, while *: $p - value < 0.01$.

prediction would be consistent with a link between the metabolic consumption of a region and the sum of its excitatory/inhibitory inputs to/from the very same region. In this analysis, we first identified groups of regions with similar connectivity profiles based on a Ward hierarchical clustering based on connectivity distance (Smith et al., 2011).

Figure 4.3.6-A shows the results with the tree distance varying between 15 and 2 clusters. Next, we tested whether SUVR variance was lower for nodes belonging to each of these functional clusters as compared to random cluster. The null hypothesis is that random clusters should have the same SUVR variance than functionally defined clusters. This analysis was repeated for clusters of different size from n=15 to n=2 correcting for multiple comparisons. As an example for n=14 clusters, SUVR variance for functional vs. random clusters was respectively 0.0123 vs. 0.0175 (median of 50,000 permutations), $p < 10 - 6$.

Figure 4.3.6-B shows that SUVR variance was significantly lower from 15 to 4 clusters, as compared to random ones. This effect was no longer present for very large clusters (n=2). By plotting the ratio of SUVR variance for functionally defined vs. random clusters, SUVR variability was relatively stable between 15 to 8 clusters (with a minimum between 8 and 12) at about $0.5 - 0.6$ of random variance, but then slowly climbed as clusters became larger in size (Figure 4.3.6-C). Therefore, a functional division of brain regions in 8-12 clusters is the most homogeneous metabolically.

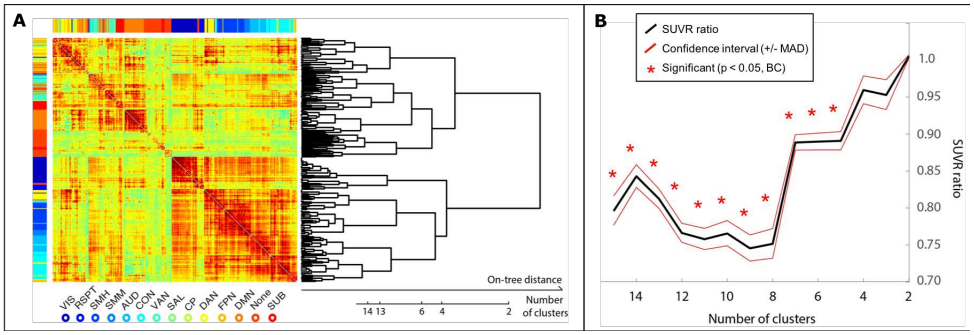

Figure 4.3.6: Regions with similar FC have lower glucose metabolism variability. (A) Group-average FC matrix (pooling across datasets) and associate hierarchical clustering tree. Colours define the baseline distance of significantly segregated clusters. The tree distance among nodes is mapped onto the corresponding number of clusters (from 2 to 15). (B) Ratio between SUVR variance of functionally defined clusters and matched random clusters (black line), as function of the number of clusters. Confidence intervals (red lines) based on $+/-1$ mean absolute deviation (mad) of SUVR ratio. As the variance ratio approximates 1, then functionally defined and random clusters tend to have more similar SUVR variability. The more homogeneous metabolic variability is obtained between 8 and 12 clusters.

Importantly, these effects were not influenced by the relative distance of nodes/regions. In fact, the average SUVR between two nodes was not related to their distance (Spearman $\rho = -0.03, p = 0.4; R^2 < 10^{-3}$).

The network structure obtained by Ward hierarchical clustering was similar but not completely overlapping to that GL atlas-derived RSNs when cutting the hierarchical tree to about 12-14 clusters. When the same analysis was repeated on RSNs as compared to random node clusters, SUVR variance was also significantly lower. The difference in SUVR ratio was comparable to that obtained for data-driven clusters (respectively 70% for Ward clusters vs. 74% for RSNs).

4.3.5 The role of network organization features

Features that describe the inter-modular connectivity role of each node as locally (CC, LE) were associated with node-level SUVR (Pearson $r = 0.39, p < 10^{-6}$ both metrics). Centrality and inter-modular connectivity (BC, PAR, VER), were not clearly associated to SUVR ($r = 0.16, p <$

$0.01 for BC, r = 0.31, p < 10^{-6}$ for participation coefficient). However, CC and LE were consistently correlated (Pearson $r > 0.9, p < 0.05$) with STR while PAR and BC had lower but significant correlation (Pearson $r = 0.79$ and $r = 0.36$, both significant at 0.05 level), suggesting a limited additional information once STR is considered from these features in explaining SUVR across nodes. A stepwise regression analysis (pooling all nodal features together) in fact identified as most significant features, to linearly explain SUVR, the STR ($p < 10^{-6}$) and VER ($p = 0.047$). Considered the borderline significance of VER feature, further analysis were based only STR.

4.3.6 Metabolic features of network HUBs

The glucose metabolic activity of highly-connected and central nodes, the HUBs, was clearly related to their nodal connectivity. Nodes with degree over the 85^{th} degree percentile (corresponding to $DEG/DEG_{max} = 122/203$ in Figure 4.3.7, selecting 35 nodes of which 15 on the right hemisphere) exhibited a clear linear SUVR-STR association (Pearsons $r = 0.63$, $p < 0.05$, FDR-corrected across thresholds) with a correlation level significantly higher ($p < 0.05$, FDR-corrected across thresholds) than the association previously observed across all parcels (up to Pearsons $r = 0.72, p < 0.05$, FDR-corrected across thresholds selecting nodes with DEG over the 92^{th} percentile).

These HUBs were consistent to those observed in (Buckner et al., 2009; Power et al., 2013; van den Heuvel and Sporns, 2013a), with the exception of posterior cingulate cortex found to have an high but limited degree, despite being a metabolic hotspot ($SUVR > 1.5$ if bilaterally considered). This association was stable over increasing DEG from $DEG = 90$, correspondent to the 70^{th} DEG distribution percentile. In this selection range ($DEG = 102 - 142$, respectively 77^{th} to 92^{th} percentile), HUBs also stably exhibited higher association than randomly chosen nodes (green box, Figure 4.3.7) and became unstable or not significant with higher thresholds due to the insufficient number of selected HUBs to draw consistent

associations.

An opposing pattern was observed considering DEG thresholds lower than the 70^{th} DEG distribution percentile, highlighting an association level possibly weakly significant and lower than observed in randomly selected nodes (purple box, Figure 4.3.7) suggesting that low DEG nodes play an important role in defining the overall SUVR-STR association which is weakly significant without them and returns to be significant only at HUB-level DEG values (i.e. over 70^{th} DEG percentile).

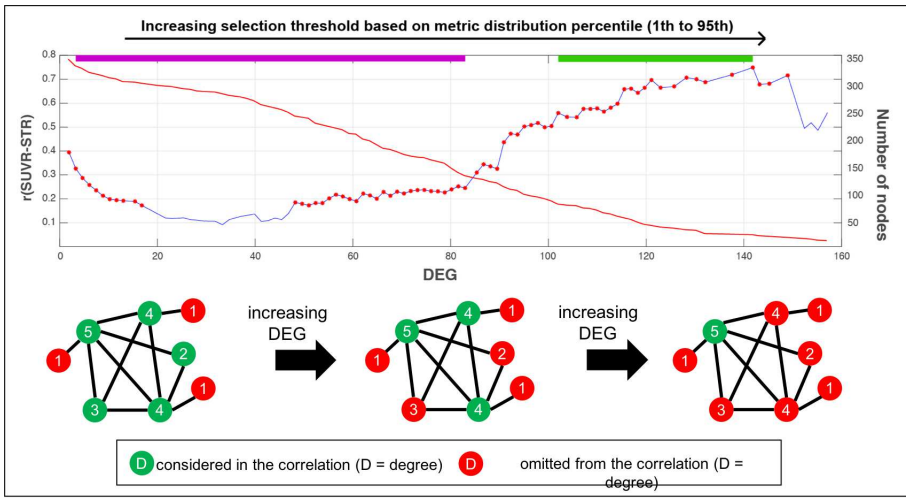

Figure 4.3.7: Functional-metabolic association over HUB nodes. HUBs identified according to different criteria, respectively based on node connectivity (degree, DEG). Association between strength and SUVR over HUB nodes selected (blue curve) by increasing respectively (x-axis) the DEG threshold. Statistically significant correlations (FDR corrected across selection thresholds, 0.05 rate) are indicated with the red star (more conservative than FDR). Decreasing density and selected HUBs are depicted by the red curve at increasing degree thresholds. Purple and green bars respectively represent degrees where selected nodes are correlated less/more to SUVR than a random group sampling.

Distinguishing the HUBs (nodes over the 90^{th} DEG percentile) according to their PAR in connectors (HUBs with PAR level over the 70^{th} PAR distribution percentile, 10/35 nodes 6 on right hemisphere) or provincials (HUBs with PAR level under the 30^{th} PAR distribution percentile, 10/35 nodes 6 on right hemisphere) while omitting others provided a signifi-

cant criteria to delineate HUB metabolism. The centrality of connector HUBs (BC and PAR features) was found to be strongly associated to the SUVR in these nodes (respectively with Pearsons $r = 0.79, p = 0.007$ and $r = 0.7, p = 0.02$) as opposed to provincial ones (respectively with Pearsons $r = 0.19, p = 0.6$ and $r = 0.2, p = 0.5$). Connector HUBs had significantly higher SUVR than provincial HUBs (Wilcoxons rank sum test, $p = 0.002$, the median SUVR in connectors was 14.5% higher than the median SUVR in provincial HUBs relative to their average). The SUVR was not significantly different among HUBs and non-HUBs correcting for multiple comparisons (Wilcoxons rank sum test, 0.05 level significance, FDR corrected).

4.4 Discussion

The relation between neural communication activity (probed by means of electrical recording of cell spiking) and glucose metabolism in the brain is a well-known biological principle (Mergenthaler et al., 2013; Shulman et al., 2004; Sokoloff et al., 1977b). Spatially integrating this cellular behaviour up to functionally homogeneous putative brain areas, whose connectivity is currently being described by rs-fMRI functional connectivity (Biswal et al., 2010; Smith et al., 2011), a relation between such a connectivity and local glucose metabolism is expected.

However, the spatial variability of brain glucose metabolism has been hardly investigated at whole brain scale supporting this macroscopic functional interpretation of the metabolism. Few studies tried to explain its variability from a connectivity perspective by using local FC metrics (Aiello et al., 2015; Tomasi et al., 2013) (e.g. ALFF, ReHo, etc) with, however, inconsistent results across studies at whole brain level.

Conversely, these metrics were very effective if the pattern agreement among glucose metabolic activity and connectivity is evaluated within the functional neighborhood of single brain regions, that is its belonging functional network referring to modern functional connectivity literature. However, the association of these metrics was still inconstant

among RSNs suggesting other explanatory mechanisms in place explaining the spatial variability of glucose metabolic activity. Eventually these results suggests that the RSN organization of the brain is fundamental to explain its actual metabolic demand.

To cover this neglect, we explored which aspects of brains network structure are biologically supported by glucose metabolic activity to provide metabolically-based validations of brain network features. The local glucose metabolism was assessed by 18F-FDG-PET SUVR, and simultaneously measured along with rs-fMRI to characterize the brains functional network structure (Bullmore and Sporns, 2012). Two datasets of healthy subjects, whose consistency in metabolic and functional terms was first of all evaluated, were considered to improve the sample size. Functional brain network structures were consistently organized as separable subnetworks recalling known topology of RSNs, each with different role and purpose (Smith et al., 2013a; Thomas Yeo et al., 2011) in resting condition.

The SUVR spatial distribution was significantly modulated by the RSNs topology. In agreement to (Passow et al., 2015), CP, DMN, SUB, RSPT and VIS networks were the most metabolically expensive RSNs and while the most metabolically expensive (CP and FPN) are considered intrinsic networks, a significantly lower metabolic demand was observed from extrinsic networks such as sensory-motor areas (Doucet et al., 2011; Golland et al., 2008).

These groups fundamentally constitutes two networks set respectively (Bullmore and Sporns, 2012) with suboptimal but stable demand underlying to the brains metabolic baseline (Raichle et al., 2001) or dynamically involved in task response and as such more explicitly optimized preferring more performing and energy efficient structural connections in agreement with the perspective offered in (Gu et al., 2018; Honey et al., 2007; Mennes et al., 2013).

Networks involved in internal information processing and decision making processes (intrinsic) are therefore more metabolically active than those involved in attention modulation, saliency, cognitive control and

information sensing (extrinsic RSNs), in agreement with an overall less operational system which eventually requires a more frugal metabolism, barely changing also during tasks administration (Raichle et al., 2001). Consistent with this view, energy-savvy (low-SUVR) nodes were more frequently encountered in SM e VAN than expected by chance while expensive (high-SUVR) ones mostly enriched RSPT, CP, FP, SUB networks, respectively part of the extrinsic and intrinsic class.

However, such inhomogeneous distribution of regions with extremal metabolic behavior along different networks without a clear ranking suggest that other mechanisms are actually modulating the region-level SUVR. We conjecture the connectivity structure and topology to be an additional clarifying mechanism useful to handle this SUVR variability.

Upon previous assumptions, higher connectivity yields higher local synaptic activity, resulting in an increased metabolic consumption (Sokoloff, 1999) that supports such connection. Considering a measure that integrates all the contributors to the local activity to best describe the local metabolic activity, such connectivity level measure should be consistently associated to the SUVR variability across regions. In agreement with a conceptually similar measure (degree centrality) used in (Aiello et al., 2015), this association was investigated considering within a graph theory framework measures of node degree, strength and eigenvector centrality. All these measures were significant although limitedly associated to the respective SUVR. Among them the node strength arose as most relevant metric in linearly explaining the SUVR.

Specifically, this association was mostly supported by the strength of between-RSN and short-range connections. The clearer metabolic role of between network connectivity is consistent with various studies (Greicius et al., 2003; Liang et al., 2012; van den Heuvel et al., 2009) suggesting the RSNs to be internally linked via (metabolically cheaper) structural projections while inter-network connectivity can be possibly less optimized, delivering a more straightforward metabolic footprint. Considering a different, phenomenological notion of energy, a recent study (Gu et al., 2018) also hypothesized a differential energy expense by within-

system interactions as compared to between-system interactions by observing a preferential support of cognitive effort from between-system interactions.

This notion of connectivity distance role is also consistent with the small-world property found to apply in brain functional networks (van den Heuvel et al., 2008). Small-world networks in fact were found to overall have high local clustering and short topologic network paths (limited number of hops to traverse the network) and are maintained by few long-distance edges evolutionary minimized because of their high cost (Kaiser and Hilgetag, 2006).

Therefore, considering the role of long-distance edges as negligible (due to their limited number and optimized behaviour) in describing the glucose metabolism relation to the connectivity across nodes, short-range edges instead are expected to play a major role on the energetic balance, in agreement with our results and in relation with a recent study (Markov et al., 2014a,b) showing that feed-forward connectivity pathways are mediated by relatively short-range connections hinting again to the sink functional behaviour of metabolically expensive nodes as previously observed.

In agreement with (Aiello et al., 2015; Tomasi et al., 2013), such relation was however not consistent in all RSNs but was significant only in VIS, SMH, AUD and FPN and partially in DMN and RSPT again suggesting the role of RSN organization goes beyond the naive regional segregation.

Note that in this study, the functional connectivity analysis was carried on by means of linear correlation analysis between the BOLD dynamics of different brain regions. This FC methodology is conveniently simple to apply and offers predictable effects from the denoising strategies (i.e. linear confound regression or filtering) while scaling efficiently over large datasets. For these reasons, it has been previously applied in countless fundamental FC studies ((Biswal et al., 1995a)) and also in this study to offer a proper glucose metabolism on the basis of previous investigations. On the other hand, recent developments offered more advanced methodologies by performing more sophisticated connectivity analysis that are

not limited to testing some form of correlation against a null hypothesis of uncorrelation (zero correlation) as they aim not only at understanding which regions are significantly, coupled but also how such connection is defined informing the researcher on the type of relationship. While the brain condition provided consistent FC measures, for example in resting and task conditions ((Cole et al., 2014)), different FC metrics from correlation such as the cross-coherence ((Sun et al., 2004)), mutual information ((Jeong et al., 2001)) or canonical correlation ((Zhou et al., 2009)) might provide valuable additional information to clarify the connectivity role on metabolism. However, these are still association measures working on tight assumptions to determine pairwise association among regions and their weight information, although very valuable can be difficult to scale across subjects therefore providing difficult to interpret glucose metabolism support.

Regarding the limited association found between overall node STR and SUVR, a possibility would be to explicitly discard unreliable or spurious connections so that their weight contribution does not confound the STR-SUVR correlation making the FC measure based on correlation also more informative. A first attempt in removing spurious edges arising from indirect connections can be for example disentangled by means of partial correlation in place of Pearson correlation or considering higher-order models to describe the entire set of connections alltogether rather than pairwise (again with the aim of providing less spurious edges) as discussed in Chapter 3 of this thesis. Removing form the STR-SUVR those edges is in fact expected to remove the confound effect promoted by indirect connections, particularly damaging central nodes exhibiting high FC to others.

Interestingly, other edge features such as its directionality could serve as additional explanatory mechanism of the involved energetic behaviour. A recent study made use of the metabolic perspective (Riedl et al., 2016) in the opposite way: determine the effective connectivity among areas based on their glucose metabolism to infer directionality. That study further suggest that the FC structure can be important but also needs

to be accompanied by the communication directionality to complete the metabolic demand picture. An intriguing possibility is that weak functional connections are not metabolically informative because their actual communication activity is strongly non-stationary. However, this imply that Pearson correlation operator can be biased and a much clear connectivity picture (also supported from glucose metabolism) might be obtained discarding the stationarity hypothesis passing to dynamic FC measures ((Preti et al., 2017)) to measure not only if a functional connection exists, but also for how long, providing direct glucose metabolic interpretation.

Even if limited, the observed STR-SUVR association also suggests that nodes with similar STR should have similar SUVR. Among the nodes with similar STR, if we consider those with similar functional landscape (i.e. they are connected to their network neighborhood in a topologically similar way), they should not have similar consumption unless the network structure has a meaningful role independently from its cumulative connectivity effect. This possibility was investigated considering the overall communication profile of each functional node to evaluate if this structure is able to shape the glucose metabolism.

In practice, if the communication structure is somehow related to glucose metabolic activity, then nodes with similar connectivity profiles should have similar glucose metabolic consumption. The connectivity profile of each node was here expressed by the FC amplitude exhibited by a node against all other nodes in the network whereas functionally similar nodes were determined by means of hierarchical clustering of the exhibited functional profiles. Our results demonstrate that topologically closer nodes, having similar connectivity profiles, have similar glucose metabolism according to the performed clustering analysis, regardless of potential distance effects in agreement to (Guo et al., 2014), advocating that functional homogeneity overall shapes the glucose metabolic homogeneity. This also suggests that the complete set of nodal connection can be needed to understand the metabolic behaviour of each node, speculated to directly result from the biological evolutionary tuning performed

at both node and whole network scale (Achard and Bullmore, 2007). Note that although functionally similar nodes (similar connectivity profiles) occurs to be significantly closer in space, the distance among nodes was unrelated to their metabolic similarity that is, closer nodes does not necessarily have a similar glucose consumption.

Considering between 8 and 12 clusters during the hierarchical analysis provided minimal and stable intra-cluster metabolic variability as compared to random samples suggesting that functionally grouping nodes with this numerosity provides a functional clustering which is metabolically supported.

This range of clusters is well in agreement with the optimal number of functional clusters determined in (Lee et al., 2012) based on a cluster dispersion measure found to be minimal when considering 7 or 11 clusters using a fuzzy-c-means clustering algorithm on averaged functional connectivity data of healthy individuals. Similarly, the clustering and stability analysis performed in (Thomas Yeo et al., 2011) reported that 7, 10, 12, or 17 networks can be stably estimated in resting state, a further confirmation of the range adequacy determined in this work which could give a parallel interpretation of network stability from the glucose metabolic consumption stability point of view. Grouping network nodes according to putative RSNs structure, as provided in (Gordon et al., 2016), provided consistently similar connectivity profiles as well but more interestingly thus gathered nodes with similar glucose metabolic activity, in agreement with previous results.

This result and the incomplete agreement exposed by traditional RSN provided with (Gordon et al., 2016) atlas, suggest that the chosen parcellation strategy, aimed at maximizing the fMRI-based signal homogeneity within-parcel to ensure consistency across subjects, might be suboptimal metabolically advising for different parcellation strategies. Note that in this study, rather than exploring the association between FC and glucose metabolism using a wide range of parcellation schemes, we focused on understanding the topological role of FC in describing the local glucose metabolism. Therefore, we did not rely strictly on RSN structure organ-

isation by also providing a data-driven analysis to determine the actual RSN hierarchy structure (i.e. data-driven instead of atlas-derived) but still based our fMRI-FC measures on a single parcellation scheme, functionally adequate, but not necessarily metabolically.

From the glucose metabolism perspective, the inherited RSN structure ((Gordon et al., 2016)) may 'over' segregate the set of parcels in too many RSN in agreement to the improved metabolic homogeneity shown between 8 and 12 clusters above, considered as metabolically-supported RSN under the hypothesis of this study. Overall, this suggests that to coherently study the metabolism heterogeneity in the brain, further effort in parcellation strategies is needed, for example providing mixed parcellation strategies to ensure proper fMRI-signal management (adequate parcel definition for consistent FC analysis) while also accounting for the glucose metabolism heterogeneity which can be otherwise confounded.

Adding other relevant network features (such as centrality and clustering measures) aimed at describing the local network structure (Rubinov and Sporns, 2010) was not beneficial in improving the limited agreement among SUVR and strength.

Moving past the classical interpretation of small world network, the overall network efficiency depends on topological short-cuts preferentially connecting highly central nodes such as the HUBs (van den Heuvel and Sporns, 2013b).
We found that the HUB regime described by highest node degree, the number of significant discrete connections, select nodes whose connectivity strength is robustly related with their glucose metabolic activity with a progressively clearer association level, highlighting their unique features of connectivity optimisation framework which entails a more clear linear cost for its links as also observed with a metabolic consumption surrogate, the hematic blood flow, found to be as well related to the node strength in (Liang et al., 2012).

Among the high-degree HUBs, we also found that a very different role is played by the participation of these nodes into a single rather than more than one network module, respectively describing provincial and

connector HUBs (Power et al., 2013). The latter class of HUBs was found to be more metabolically expensive, in agreement with their more central network role and previous literature results suggesting an increase in their activity during tasks involving multiple cognitive functions while provincial hubs have more stable activity during task switching (Mišić and Sporns, 2016). The consumption of connector HUBs was also significantly mediated by their participation level across multiple modules in a picture: higher glucose metabolism is demanded by more central HUBs.

As suggested in (Power et al., 2013), a suitable measure to detect HUBs is based on within-module degree. Other than a pattern across selection thresholds in good agreement with the one obtained with DEG, we found that dividing the network with 9 to 25 modules provides a suitable means for degree normalisation that provides selected HUBs with robust STR-SURV association, nonetheless suggesting an adequate range of resolutions for network modularity analysis supported by glucose metabolism arguments. This range was also in agreement with the optimal number of detected modules reported in (Doucet et al., 2011; Lee et al., 2012; Thomas Yeo et al., 2011), whereas the less clear SUVR-STR association found by normalizing the DEG considering a modularity structure given by putative RSNs suggest their limited role in describing high-level network features.

Taken together, these observations suggest that high connectivity (by means of significant number of connections, i.e. degree) and network centrality (network role) are strongly related features in the brain that covariate in defining their energetic needs suggesting that possibly one functional feature is not sufficient to characterize brain HUBs (van den Heuvel and Sporns, 2013a) maintaining an adequate biological support but as we found for betweenness centrality and participation alone, not all nodal features provide effective means to detect HUB with metabolically supported connectivity.

4.4.0.1 STUDY LIMITATIONS

Several limitations of this work should be considered:

- The glucose metabolic activity measure, namely SUVR, can offer a biologically confounded interpretation as compared to quantitative kinetic tracer 18F-FDG-PET analysis (Hamberg et al., 1994b; Keyes, 1995) and variably biased by non-neurological effects nonetheless interacting with the brain metabolism measure (Laffon et al., 2008) even in neurologically healthy subjects.

- A single parcellation strategy was used to ensure consistent fMRI-FC measures across subjects. However, such parcellation is by no means optimized also from the glucose metabolism perspective and can act as metabolic heterogeneity confound operator. Even if the underling hypothesis was that the functional homogeneity can directly influence the glucose metabolism homogeneity (as seen in previous studies where the FC amplitude and regional homogeneity were strongly associated to the glucose SUVR distribution at voxel scale (Aiello et al., 2015)), further investigations might benefit from the use of more parcellation schemes to more clearly address the relationship between metabolism and FC.

- In this study, to cope with FOV limitations of fMRI data which not always encompassed subcortical areas consistently in all subjects, we summarized the FC of subcortical nuclei and cerebellum as single parcels (i.e. averaging all enclosed voxel dynamics) and enclosing their FC contribution as separate network. However, future investigations might benefit from the use of finer parcellation schemes for example able to cope with functional differences of Thalamus or Cerebellum. It has in fact been observed that different part of the Cerebellar cortex are actually functionally connected with brain cortical areas by (Dobromyslin et al., 2012), suggesting that the number and actual RSN hierarchy can be shrinked from that used in this study toward more compact schemes as also metabolically suggested above. This parcellation refinement would also provide a further validation tool to verify the scalability of presented results.

- Current large-scale FC models of the human brain were meant to

capture only the inter-regional connectivity across macroscopic putative areas while intrinsically neglecting any functional contribution from local neural circuitry. Improved methods to identify the FC structure are thus needed clear spurious connections offering an unbiased perspective on the actual communication structure expectedly extend the metabolic support of the identified structure. Even if the network contribution is currently unclear, time-variant components of connectivity are likely to play an important role in understanding the energy consumption in the brain network. Therefore, unlike the simple first-order connectivity metric employed in this study as based on Pearson linear correlation to support metabolically previous studies, future investigations will purposely benefit from enhanced FC measures or mascroscopic models. A second level investigation might as well benefit from those novel FC approaches providing deeper insights about the glucose metabolic association to FC structure.

- Finally, related to the previous limitations, a limited experimental sensitivity can be advocated from the group-level analysis carried out. In fact, even if averaging the FC structure was expected to lower the inter-subject variability of FC measures while suppressing not stable network features shared to different subjects, averaging the local glucose metabolism could provide stable estimates but affected by intrinsically lower sensitivity which neglect the observation of finer metabolic optimisation principles to be possibly observed at single subject level. To promote even more reliable FC measures, the current experimental paradigms for FC measurements might be first of all extended to encompass the complete brain within the FOV, provide more comprehensive sampling (i.e. longer scan durations to better characterise the fMRI dynamics) in each subject to promote better denoising strategies and consider a larger populations of subjects with eventually more homogeneous age range.

4.5 Conclusions

Functional brain networks share a common organization (Gratton et al., 2018) but their role in pathological alterations, often accompanied by sharp glucose metabolism impairments, is still incompletely understood. In this work, we strived to describe the local brain glucose metabolism in terms of brain functional networks by identifying which organization principles can explain the actual consumption. We found a consistently different glucose metabolic activity in different networks and even if without a clear metabolic ranking, functional criteria attributed by the network role and intrinsic/extrinsic distinction provided meaningful insights about the glucose consumers in resting condition.

Cumulative connectivity measures partially explained the regional metabolism noticing that the node strength was the most clearly associated to local metabolism, in agreement with previous voxel-level (Tomasi et al., 2013) or network level (Vaishnavi et al., 2010) analyses. This association relied on short-range and between-network connections in agreement with (Guo et al., 2014; Hermundstad et al., 2013)based upon a distance effect currently only principled (Achard and Bullmore, 2007; Bullmore and Sporns, 2012). Even if local organisation metrics were less able to clearly describe the associated regional glucose metabolism, some interesting departures from association linearity among strength and glucose metabolic activity suggested a network-related metabolic behaviour in resting state indeed verified to provide inconsistently clear association as explained by potentially different efficiency mechanisms (Passow et al., 2015; Vaishnavi et al., 2010). The connectivity of central network nodes, or HUBs, was more consistently associated to their glucose metabolic activity with a suggestive effect from their network role: the glucose metabolic behaviour of inter-module facilitators (connectors) is different from that of local mediators (provincial), in connection to the previously observed abrupt metabolic sensitivity and functional alterations in neuropathology (Nugent et al., 2015; Scherr et al., 2018) involving HUBs. Rather than single network features, we found that it is the

entire set of connections that eventually shapes the local metabolic activity: topologically closer nodes indeed tend to be metabolically similar. Future investigations will benefit from considering an enhanced dataset that allows a second stage analysis aimed at clarifying the observed FC to metabolism relationship making use of more complex but sensitive FC measures which, once associated to proper parcellation methods, could provide more clear explanatory mechanism on the glucose metabolism heterogeneity.

These observations have consequences for basic neuroscience research and neuropathology indicating that: (1) brain network structure obtained from FC shapes the local metabolic activity in the brain; (2) individual functional connections are not effective in explain the metabolic demand, instead short-range and between network connections cumulatively play a metabolic role with limited influence from the local network organization; (3) the metabolic activity of high-rank nodes, backbone of the brain network (van den Heuvel and Sporns, 2013b), is consistently tuned according to their connectivity and role in the network compared to less central nodes. Afterwards, the regional metabolism could be thought as an additional valuable tool to comprehend and guide network structure selection promoting physiologically reasonable communication structures and bridge alterations of connectivity structure and metabolism in pathology.

4.6 Supplementary material: Consistency analysis

4.6.1 Comparison of 18F-FDG PET data

We compared SUVR values between the Munich dataset (A) and Naples dataset (B) at the parcel level of the GL atlas (Gordon et al., 2016). Out of 347 parcels only 12 exhibited significant differences between datasets (Figure 4.6.1-A). Most of these parcels (7/12) belonged to the None network (Gordon et al., 2016) that forms small clusters, rather than well-organized RSNs, and overlaps with regions of high magnetic susceptibility and poor signal-to-noise.

The other regions showing different SUVR values between datasets were scattered over different RSNs with no discernible pattern. The SUVR variability measured as $CV_{\%}$ across subjects, was of $5.4 \pm 1.3\%$ (median $\pm$ mad over all ROIs) in dataset A, $7.0 \pm 1.3\%$ in dataset B and remained consistent once the datasets are merged at $6.8 \pm 1.0\%$ in relative agreement with their size difference.

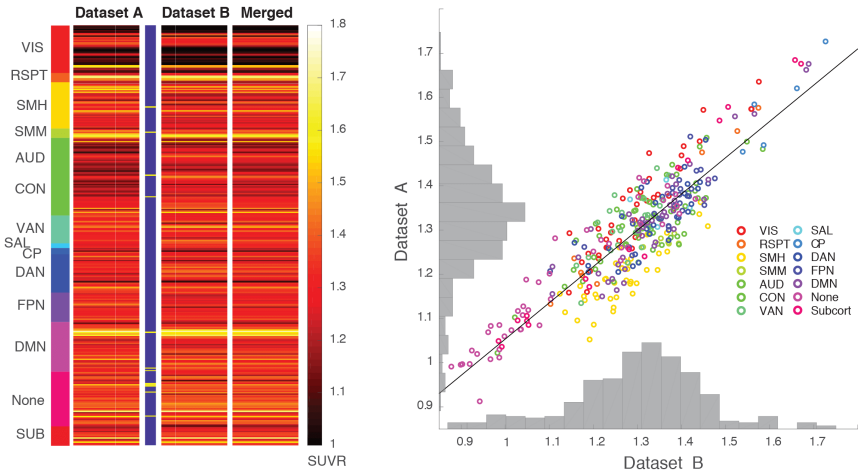

Figure 4.6.1: Glucose metabolism (SUVR) agreement between datasets. (A) Group-average nodal SUVR ordered by network (lateral colour label bar) for the two datasets and the merged one. Statistically significant SUVR differences between datasets are reported in the central blue/yellow column bar (yellow for significant differences). (B) Scatter plot and linear regression of SUVR across corresponding parcels, values colour-coded by RSNs.

SUVR values between datasets were strongly linearly related. Figure 4.6.1-B shows the linear regression agreement ($SUVR_B = 0.978xSUVR_A + 0.03, R^2 = 0.89$, where $SUVR_{A,B}$ represent the SUVR in dataset A or B) between SUVR values in corresponding parcels of the two datasets. The SUVR values frequency distribution in the two datasets show a similar mean/median and variance. Regression of age and gender covariates prior to intra-dataset averaging did not affect appreciably the observed linear agreement ($R^2 = 0.8$).

Visual inspection of Figure 4.6.1-B also shows that the smaller SUVR values mapped onto regions of the None network; that intermediate SUVR values mapped onto sensory (VIS, AUD) and motor (SMH, SMM) regions, and that the highest SUVR values mapped onto some nodes of associative networks (CP, SAL, DMN). Similar results were obtained when comparing SUVR values sampled with different surface sampling strategies. In summary, we conclude that the two datasets were highly comparable in terms of SUVR values and their variability at the parcel level of a functionally defined cortical atlas.

4.6.2 Functional Connectivity comparison

Next, we compared local and global metrics of BOLD signal time series in the two datasets. At the parcel level, we measured in each data set: (1) the amplitude of low frequency fluctuations (ALFF, i.e. the power of the signal within [0.01, 0.1] Hz band); (2) the fractional ALFF (fALFF), i.e. the power within the low frequency range [0.01, 0.1] Hz, divided by the total power in the entirely detectable frequency range; (3) The Regional Homogeneity (ReHo) for the signal between each voxel and its neighboors. Local fMRI signal metrics were highly consistent between the Munich and Naples dataset, with R^2 linear agreement of 0.84, 0.92 and 0.80 for ALFF, fALFF, ReHo, respectively. The metric variability across subjects ($CV_{\%}$) between datasets was similar for ALFF ($CV_{\%A,B} = 24.3; 26.3$), fALFF ($CV_{\%A,B} = 6.5; 9.7$), but slightly different for ReHo ($CV_{\%A,B} = 14.1; 20.4$). These metrics were not significantly altered when pooling all subjects of

the two datasets ($CV_{\%}\ ALFF = 28.6, fALFF = 9.4, ReHo = 21.8$).
We then compared group average FC matrices obtained from each dataset. FC matrices were organized into Visual (VIS), Retro Splenial Temporal (RSPT), Sensory-motor-hand (SMH), Sensory-motor-mouth (SMM), Auditory (AUD), Cingulo opercular (CON), Ventral Attention (VAN), Salience (SAL), Cingulo Parietal (CP), Dorsal Attention (DAN), Fronto-parietal (FPN), Default Mode (DMN), Unassigned (None) networks according to the RSN scheme proposed in (Gordon et al., 2016), while parcels corresponding to subcortical regions were assigned to the Subcortical (SUB) group. On visual inspection (Figure 4.6.2-A), the two FC matrices showed a similar RSN architecture with higher within-network connectivity and lower between-network connectivity. A noticeable scaling effect with overall higher FC values in the Naples sample (dataset B) can be also noted.

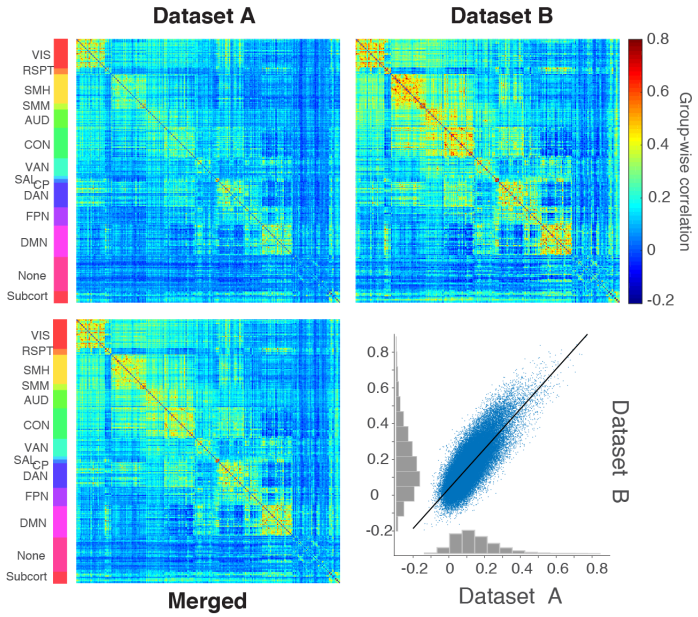

Figure 4.6.2: Functional connectivity (FC-fMRI) agreement between datasets. A) Group-FC matrices of the two dataset (A, B) and merged (Merged). B) Linear regression analysis of the respective FC weights distributions of the two datasets overlaid to a scatter plot of the correspondent FC weights.

The linear regression of FC values at the parcel level between datasets

was moderate ($R^2 = 0.64$) (Figure 4.6.2-B). Comparatively, the linear consistency across random samples of subjects in each dataset was similar. In dataset A (Munich), comparing the average FC of 5 versus 5 random subjects, we obtained a relationship equal to $R^2 = 0.58 \pm 0.023$ (median $\pm$ mean absolute deviation (mad) of random sampling), while in dataset B (Naples), comparing the average FC of 8 versus 8 random subjects, the corresponding values were $R^2 = 0.66 \pm 0.021$. These figures are comparable to other reports on inter-group (Choe et al., 2015; Liu et al., 2018b), or inter-subject variability (Gratton et al., 2018). Moreover, the spatial correlation of the group average FC matrices for dataset A and B, with or without removing linear scaling, was in excellent agreement ($R^2 = 0.995$). In summary, we conclude that, notwithstanding scaling differences in FC weights, the overall functional organization was similar in the Munich and Naples datasets, comparable to other reports in the literature on agreement between groups (Choe et al., 2015; Liu, 2017), or inter-subject variability within the same group (Gratton et al., 2018).

5

A functional connectivity perspective on Multiband EPI imaging

5.1 Introduction

Forecasting the importance of single-subject FC characterization (Anderson et al., 2011; Badea et al., 2017; Shah et al., 2016), unbiased tools for FC from fMRI data requires a more detailed exploration of the confounds effects attributed to motion artefacts, noise propagation as well as any other source of variability able to alter local fMRI signal variance.

Besides the structured signal artefacts extensively studied elsewhere (Griffanti et al., 2017), the role of thermal and residual physiological noise propagation (i.e. after adequate confound removal) is expected to play a major role on FC as currently based on linear correlation analysis (Triantafyllou et al., 2005, 2011; Wald and Polimeni, 2017), since any experimental factor able to enhance the temporal local noise content (e.g. image

acceleration) could nonetheless alter the FC measure, possibly even more at single-subject level which exhibit higher sensitivity to the subject brain features but to its confound and noise content qualities as well.

Unbiased FC studies require adequate experimental optimisation of the employed sequence together with data processing: ideally, other than minimal temporal noise content to avoid uncertain connectivity descriptions, each data processing step should be designed to limit the impact of temporally structured artefacts not related to the brain dynamic of interest (i.e. confounds from drift to the subject motion). Their effect can be ameliorated during post-processing (Bright et al., 2017; Griffanti et al., 2015; Murphy et al., 2013) provided that these phenomena are adequately sampled. This introduces a tight experimental trade-off in terms of temporal/spatial resolution and brain coverage which limit the effectiveness (Bright et al., 2017) of confound removal.

Despite their great potential, recent MB-EPI sequences are fundamentally limited by current MRI hardware technologies and to maximise the achievable acceleration levels with adequate image quality different strategies have been implemented (Todd et al., 2016) with unclear effects of enhanced image acceleration over the FC structure. In fact, the role of noise propagation at different levels of image acceleration, is expected to play a major role on FC since higher acceleration is connected to a potentially lower FC estimates through enhanced signal variability, limiting the methods potential at single subject level.

Building upon previous considerations about hardware and acquisition choices that could affect the ratio of thermal to non-thermal noise content over the fMRI signals (Triantafyllou et al., 2011; Wald and Polimeni, 2017), we studied the impact of a shifting noise regime and amplitude over the FC estimates at single subject level.

FC differences obtained at different acceleration levels (thus different noise propagation level) will be studied under virtually matched experimental conditions designed matching sequence settings to focus only on propagation of thermal noise content.

5.2 Materials and Methods

5.2.1 Participants and data acquisition

Ten healthy subjects (M/F: 7/3, age: 25.2 ± 4.3 yrs) were scanned on a Siemens mMR Biograph 3T PET-MRI scanner (Siemens, Erlangen, Germany) using the vendor-supplied receive coil (12 channels). Written informed consent was obtained from all subjects who were instructed to maintain their eyes open and not fall asleep during the scan. A T1w-MPRAGE image (T1w) was collected for each subject (256x256x160 matrix, 1mm isotropic voxel, $T_R/T_E/T_I$ =2400/3.24/1000 ms, FA=8 deg, GRAPPA R=2). Resting-state fMRI (rs-fMRI) data was acquired using a 2D MB Gradient Echo EPI sequence (*ver.* R014, (Moeller et al., 2010; Setsompop et al., 2012; Xu et al., 2013)).

All fMRI scans shared: isotropic 3 mm voxel size; 6868 acquisition matrix size; T_E = 30 ms; Echo spacing = 0.51 ms; sequence-default CAIPI shift. FMRI volumes were reconstructed using Split-Slice-GRAPPA (Cauley et al., 2014) with default parameters. Two Spin Echo EPI (SE-EPI) images, geometrically-matched to fMRI volumes, were acquired with parallel and reversed phase encoding (PEdir) orientation for distortion correction.

To study the receive performances of the standard 12-ch head coil for MB imaging, fMRI volumes were collected with both axial (AX) and coronal (COR) slice orientation. Different performances were expected along different directions because of the modest inhomogeneity profile available along head-feet direction as compared to in-plane (left-right and antero-posterior). Coronal orientation had been prescribed to investigate whether the theoretical improvements of signal dropout and slice un-aliasing performance (Todd et al., 2016) resulting from the proper usage of receive coil sensitivity profile play a clear role on fMRI functional connectivity data.

Resting state fMRI acquisitions

Two experimental protocols were implemented, first to identify suitable sequence settings for fMRI-FC studies (P1) and then assess their performance for FC estimation (P2).

P1: 16 fMRI runs of 50 volumes (TR = 3700 ms, flip angle - FA = 90) were acquired in five subjects by varying: *slice orientation* (AX, COR); *MB* factor (1-4); *iPAT* factor (1, 2).

In-plane parallel imaging acceleration (iPAT) was based generalized autocalibrating partially parallel acquisitions (GRAPPA) (Griswold et al., 2002).

The considered iPAT factor (image acceleration factor, R) corresponds to the ratio of the desired k-space phase-encoding lines prescribed over the number of k-space lines actually acquired after each RF excitation (e.g. iPAT = 2 acquires half of the echoes to fill the k-space while missing phase-encoding lines are recovered with GRAPPA algorithm) as compared to the acquisition of the entire k-space during each EPI train (i.e. iPAT = 1 filling the entire k-space). Conversely, the MB factor (slice acceleration factor, MB) corresponds to the number of simultaneously RF excited slices, directly influencing the achievable T_R and FOV. Axially oriented volumes comprised 40 slices with anterior-to-posterior (A-P) PEdir while coronal volumes of 60 slices with left-to-right (L-R) PEdir.

Out of all settings explored in P1, three provided adequate performances, respectively determined by: 1) achievable temporal ($T_R \sim 1\ sec$) or spatial ($voxel\ size \leq 3\ mm$) sampling and coverage (FOV for whole brain imaging); 2) limited image artefacts content and EPI ghosting level (required stable amplitude <10% and motion-independent); 3) adequate tSNR and signal dropout.

These three settings (Table 5.2.1) were further explored during **P2** collecting 12 minutes of rs-fMRI with minimal TR and same geometric parameters from P1 (FA according to Ernst angle (Ernst and Anderson, 1966)) in the remaining five subjects. Each run (Table 5.2.1) was collected along opposing PEdirs and consecutive days (test-retest) overall providing 6x2 fMRI runs/subject. In the following these main settings will be

referred according to the following notation: slice orientation (AX, COR), iPAT factor (1, 2) MB factor (2, 3). Therefore, runs 1-4 of Table 5.2.1 will refer to the AXR1MB2, 5-8 to CORR1MB3 and 9-12 to CORR2MB3 setting.

Run	1	2	3	4	5	6	7	8	9	10	11	12
MB / slice orientation	2 / AX				3 / COR							
iPAT (R) / TR [ms]	1 / 1261								2 / 1090			
Phase encoding	A-P		P-A		L-R		R-L		L-R		R-L	

Table 5.2.1: Sequence parameters acquired during protocol 2 (P2) for single-subject FC assessment. Each run was repeated on consecutive days along two test/retest sessions.

5.2.2 Data processing: P1

Structural T1w images were bias field corrected (*N4BiasFieldCorrection*, ANTs v2.1), skull stripped (*bet*, FSL v5.09, www.fmrib.ox.ac.uk/fsl, (Smith et al., 2004)), segmented (*fast*, FSL v5.09, (Smith et al., 2004)) for principal tissues (gray matter-GM, white matter-WM, cerebro-spinal-fluid-CSF) and parcelled in 108 regions of interest (ROI) with *Multi-Atlas Label Fusion* (MALF) method (Hongzhi Wang et al., 2013) and MICCAI2012 reference dataset. FMRI data was motion corrected (*mcflirt*, 12 degree of freedom - dof, FSL) using the single band image as reference (temporal average for non-MB accelerated data) and high pass filtered (*butterworth*, 128s cutoff).

Framewise displacement (FD) (Power et al., 2014) was evaluated and motion affected volumes (0.5 mm threshold) discarded. Prior to T1w image registration (Boundary Based Registration approach, 12 dof *flirt*, FSL), functional data was corrected for geometric distortions *(topup*, *FSL)* using run-specific SE image pair. Proper distortion correction and registration was visually ensured.

A schematic summary for data pre-processing is reported in Figure 5.2.1. Temporal Signal to Noise Ratio (tSNR), was calculated as ratio of

the standard deviation of voxel signal and its temporal average in native EPI space, finally resampled on the T1w reference.

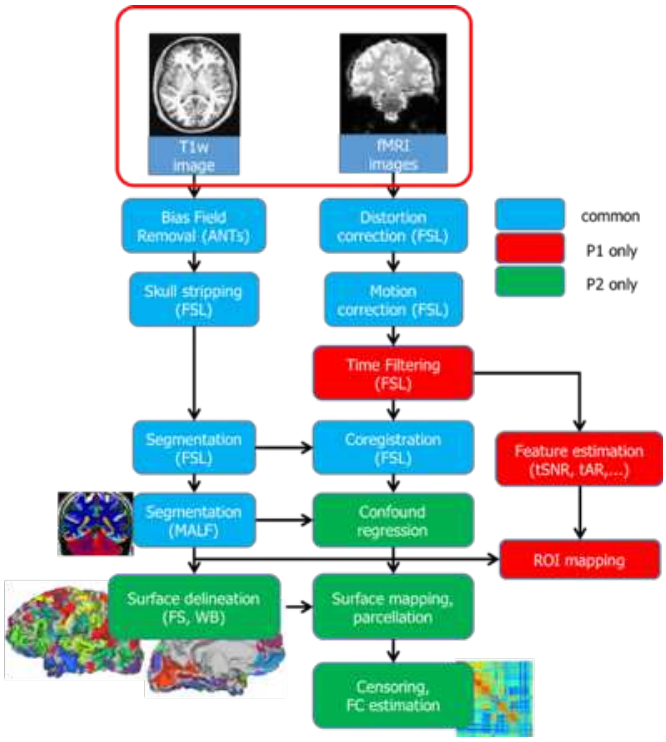

Figure 5.2.1: Pre-processing pipelines implemented for P1 and P2 illustrating all the processing steps employed in the two protocols. Processing steps are color coded according to the pipeline usage by protocol (see legend).

Statistically significant differences in tSNR were evaluated by means of 3-way analysis of variance with repeated measures (3way-ANOVA, $p<0.05$) and slice orientation, iPAT and MB as main factors. A Greenhouse-Geisser correction scheme was applied in case of sphericity hypothesis violation, separately assessed with a Mauchly test (0.05 significance level) per factor and interaction considered in the model.
Factor interactions were explored also regionally performing a similar 3way-ANOVA over frontal, temporal lobes, subcortical areas and, as comparison reference, midbrain areas (posterior cingulate cortex, sensory-motor areas). Statistical assessment was carried out using JASP software (v.0.9).

Visual assessment for unusual signal dropout, distortions, ghost effects and MB-related residual artefacts were carried out by means of *fslview* tool (FSL v5.09, www.fmrib.ox.ac.uk/fsl, (Smith et al., 2004)) at single-subject level as part of the image quality assessment based on artefact, ghost, noise content. Extra care was due to the presence of tSNR banding and residual aliasing effects attributed to MB acceleration.

5.2.3 Data processing: P2

In addition to the pre-preprocessing described in the section 5.2.2, in the section 5.2.3 the structural image was used for cortical surface delineation (Freesurfer v. 5.3, https://surfer.nmr.mgh.harvard.edu/fswiki; Caret v. 5, Connectome Workbench v. 2.3 (Marcus et al., 2011)) and functional parcellation (Gordon functional atlas (Gordon et al., 2016) for cortical parcels, MALF method (Hongzhi Wang et al., 2013) for subcortical nuclei).

FMRI data was further confound-regressed removing the contribution of estimated motion traces and its first-order derivatives, the five most variance-explanatory PCA components of WM and CSF signals (Salimi-Khorshidi et al., 2014), high pass cosine filter basis (cutoff frequency 0.009 Hz). Regressed fMRI data was then AR(p) whitened (Arbabshirani et al., 2014; Lund et al., 2006), modelling the signal temporal autocorrelation structure by a family of 8 exponentials with halflives from 0.5 to 64 TRs.

Pre-processed fMRI signals were finally registered to T1w reference image and resampled over the delineated cortical surface. Parcel-representative fMRI signals were obtained by averaging all the signals from nodes belonging to the same cortical surface parcel.

Similarly, voxel-wise fMRI signals were averaged to obtain representative time course for all defined subcortical areas (bilaterally: Caudate, Putamen, Accumbens, Pallidum, Amygdala, Hippocampus, Thalamus, Ventral diencephalon, Cerebellum cortex) anatomically defined from MALF segmentation. For each parcel and run, tSNR was computed as local noise content probe.

FC matrices were obtained by Pearson cross-correlation of all parcel-defined time courses, subsequently Fisher's z-transformed obtaining 12 matrices (351x351) per subject. A schematic summary for data pre-processing is reported in Figure 5.2.1. Each FC matrix was processed to determine the node strength, eigenvector centrality, local efficiency and participation coefficient (Brain Connectivity Toolbox (Rubinov and Sporns, 2010)) after FC normalisation. FC binarization was obtained by at 90% sparsity level (10 upper percentile of highest FC values retained).
Significantly non-null FC edges were detected at group level by means of Network Based Statistics (NBS method (Zalesky et al., 2010) with cluster enhancement by extent, F-test with base threshold 3.1 and 5000 permutations, 0.05 overall significance level, 5 subjects) tool.

5.2.4 Functional connectivity sensitivity analysis

Statistically significant FC differences across sequence settings were evaluated with a 1way-ANOVA with FDR correction for multiple comparisons (0.05 level) with t-test as post-hoc tests while the agreement in terms of estimated edge-level amplitude was evaluated by linear regression across multiple settings. This analysis was performed both over full FC matrices (thus comparing edge connections between settings, pooling opposed PEdir and T/RT) and on the nodal features and similarly between FC matrices obtained during T/RT scans to highlight setting-related stability issues.

Possible FC differences across settings were explored in terms of noise propagation. By definition of Pearson linear correlation, the temporal covariance of two fMRI signals is divided by the product of their temporal standard deviations, then any element able to modify temporal variance or covariance structure would affect the FC estimate. Under controlled experimental conditions, we attributed any difference in temporal variance to enhanced noise propagation resulting from increased image acceleration rather than minor differences in experimental parameters or physiological variability.

To test if the noise content is able to explain FC differences between settings, the product of tSNR, measured in two ROIs, was linearly regressed (t-test for slope significance with level 0.05, FDR criteria) to the FC of these ROIs along different settings (significance level 0.05, FDR criteria). A similar analysis was performed to assess the noise linear dependence of FC-derived nodal structural features, separately repeated adding a categorical covariate to account for slice orientation.

5.3 RESULTS

5.3.1 tSNR ASSESSMENT

The effect of MB and iPAT factors on tSNR along two slice orientations was represented in Figure 5.3.1-A, for a typical tSNR distribution in a mid-brain axial slice. Coronal slice orientation visually provided higher tSNR (even rows, Figure 5.3.1-A) compared to equi-accelerated scans along axial slice orientation (odd rows, Figure 1-A) with $MB > 1$, regardless of iPAT. Observing Figure 5.3.1-A, the tSNR loss and tSNR spatial inhomogeneity with increasing MB acceleration appears more marked using an axial orientation whereas only at the maximum total acceleration (MB x iPAT = 4 x 2), the observed tSNR loss pattern of coronal acquisitions was comparable to axial acquisitions considerably less accelerated (MB x iPAT = 2 x 2).

This performance shift suggests that MB-related noise propagation ($MB > 2$) interacts with slice orientation while iPAT usage provides a tSNR loss with spatial pattern typically observed under apparent physiological ($MB = 1$) rather than thermal noise regime ($MB > 1$). A critical point across these two regimes was observed using $MB = 2$ which, collected without iPAT provide high and spatially homogeneous tSNR in both orientation but enabling iPAT axially provided a tSNR pattern shift more clearly compatible to the expected g-factor whereas a similar coronal acquisition was in the between of the two noise regimes highlighting a more favourable BOLD sensitivity with this setting (coronal, $MB = 2$).

Higher MB acceleration levels ($MB > 2$) instead provided a tSNR loss pattern more consistent with the thermal noise regime even without iPAT. Interestingly, the tSNR observed coronally without iPAT was the unique combination stable across MB factors, highlighting a favourable noise propagation regime ($MB = 2 - 4$) thus possibly limited g-factor enhancemen t as confirmed in all scanned subjects. Noise regime in axial acquisitions was also confirmed by observing the pattern of net tSNR loss with increasing MB factor regardless of iPAT whereas coronal acquisitions provided stable average tSNR or an increasing/decreasing trend respectively enabling or not iPAT (Figure 5.3.1-B).

The patterns of tSNR loss observed axially or more interestingly in the coronal direction by increasing (from $MB = 1$ to $MB = 2$) then decreasing (from $MB = 2$ up) were consistent to previous observations (Todd et al., 2016), but were not further investigated in this study as we were interested in settings with temporal sampling adequate for functional connectivity (i.e. $MB >= 2$ axially or $MB >= 3$ coronally to cope with the different number of slices collected).

Previous observations were statistically assessed with a 3way-ANOVA (2x2x3 levels, main factors: slice orientation, iPAT and MB) over all brain areas, pooled together to study whole-brain effects. Significant main effects were found on slice orientation (F (1, 97) = 147.2 p $<$ .001, $\eta^2 = 0.6$), iPAT (F (1, 97) = 1820.8, p $<$ .001, $\eta^2 = 0.95$) and MB (F (1.24, 120.1) = 258.6, p $<$ .001, $\eta^2 = 0.72$, Greenhouse-Geisser corrected) over the tSNR. The interaction between slice orientation and iPAT was not significant (F (1, 97) = 0.37, p = 0.54, $\eta^2 = 0.004$) consistent with the geometric arrangement of receiving elements (cylindrical symmetry) of the receive coil used, expected to comparably support parallel imaging along the adopted PEdirs. Instead, MB factor was found to interact both with slice orientation (F (1.59, 154.3) = 468.9, $p < 0.001$, $\eta^2 = 0.83$, Greenhouse-Geisser corrected) and iPAT (F (2.38, 230.8) = 111.7, p $<$ 0.001, $\eta^2 = 0.54$, Greenhouse-Geisser corrected).

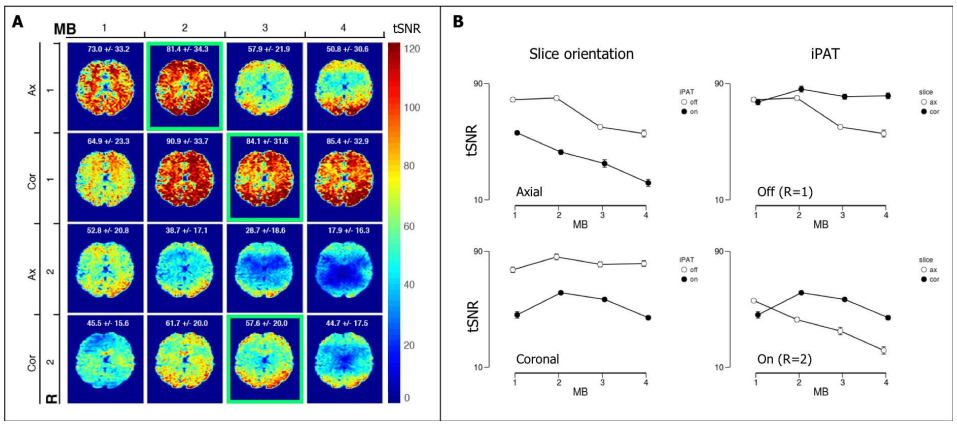

Figure 5.3.1: (A) tSNR spatial distribution in a representative subject with different sequence settings. Average $\pm$ standard deviation of intra-mask (brain-only) tSNR is separately reported in each box with acceleration parameters referred by upper row and laeral labels. Adequate settings (by artefact content and sampling capabilities) are highlighted in green. (B) tSNR marginal means (averaged over 5 subjects) obtained by splitting the three main experimental factors of P1 protocol (whole-brain average). Each box represents tSNR with increasing MB acceleration either with fixed slice orientation (left column) or iPAT acceleration (right column) depicting the other factor separately.

Observing the marginal mean plots in Figure 5.3.1-B, the relation between MB and tSNR was visibly modulated by the slice orientation (regardless of iPAT but more clearly when enabled). Conversely, the significant interaction found between MB and iPAT was resolved by specifying the slice orientation. In fact, with fixed slice orientations, the association trends between tSNR and MB were parallel across iPAT levels suggesting that MB was not interacting with iPAT in degrading the tSNR, once the slice orientation is specified.

A post-hoc paired t-test revealed that tSNR of axial acquisitions was significantly lower than coronal acquisitions ($p < 0.001$, Cohen's $d = -2.06$). The same test, Bonferroni-corrected over levels, suggested that increasing MB ($MB >= 2$) generally decreases the tSNR ($p_{Bonferroni} < .001$, Cohen's $d > 1.67$).

A 3w-ANOVA analysis was also performed to test tSNR dependency on main effects over four non-overlapping sets of contiguous areas considering frontal, temporal, subcortical and regular areas (posterior cingu-

late cortex, post-central areas, pre-central areas, superior frontal gyrus, orbito-frontal gyrus) and explore spatially-dependent effects (spatially represented in supplementary Figure 5.6.1).

Slice orientation did not account for significant tSNR differences in frontal areas (Figure 5.3.1, supplementary Figure 5.6.1) while significantly different tSNR were observed in temporal, subcortical o reference areas across slice orientations (row 1, Figure 5.3.1). As reported in supplementary Figure 5.6.1, the tSNR distribution of coronal settings was significantly higher than axial ones except for frontal areas. Differentiating the tSNR distribution according to the actual iPAT usage (supplementary Tables 5.6.1, 5.6.2) we found that (except for frontal areas) an overall significantly higher tSNR (supplementary Table 5.6.2) using coronal orientation with particular tSNR enhancement in temporal, subcortical and regular areas while using iPAT or pronounced tSNR advantages in subcortical and regular without using iPAT.

In all tested areas the MB factor accounted for statistically significant tSNR differences (row 2, Table 5.3.1) and significantly interacted with the slice orientation factor (row 4, Table 5.3.1) in agreement to the whole-brain results. Conversely, the lack of interaction between iPAT and slice orientation was not verified in temporal areas (row 2, Table 5.3.1) where the tSNR dependency over the slice orientation was significantly modulated by iPAT.

The MB factor that locally maximized the tSNR (in average across subjects) was strikingly dependent on the slice orientation which interacts differently with iPAT. This result was spatially depicted in supplementary Figure 5.6.2 where each area delineated was color-coded according to the MB factor which maximized the average tSNR across subjects. Considering axial orientation the figure confirms how without iPAT (second row, supplementary Figure 5.6.2) neatly half of the areas were optimized by omitting MB acceleration (coloured light blue) particularly in upper cortical areas or subcortical nuclei while the remaining was optimally supported by MB = 2 (coloured yellow) while to maximize the tSNR with iPAT almost all of the areas abandoned the usage of MB (third row, sup-

plementary Figure 5.6.2).

Instead, the MB factor which maximized the tSNR along coronal orientation was of 2 in most of the areas (82% regardless of iPAT usage) while other MB factors were optimal in up to 9% of the remaining areas.
The spatial pattern of optimal MB to support maximal tSNR was instead dominated by MB factor 2 along coronal orientation with little-to-no impact regarding iPAT usage (fourth/fifth row of supplementary Figure 5.6.2). Few occipital-parietal brain areas exhibited optimal support even at higher MB factor of four (without iPAT represented by brown colour on the fifth row, supplementary Figure 5.6.2) and three (with iPAT represented by red colour on the fourth row, supplementary Figure 5.6.2), consistently across the iPAT.

Factor / Brain region	Frontal lobe (20)	Temporal lobe (12)	Subcortical areas (12)	Regular areas (14)
slice orientation	$F(1,19) = 0.69, p = 0.4$	$F(1,11) = 37.2, p < 10^{-3}$	$F(1,11) = 152.5, p < 10^{-3}$	$F(1,13) = 156.0, p < 10^{-3}$
MB	$F(1.7,32.3) = 93.0, p < 10^{-3}*$	$F(1.7,19.5) = 132.4, p < 10^{-3}*$	$F(1.6,17.4) = 344.8, p < 10^{-3}*$	$F(1.1,13.9) = 53.2, p < 10^{-3}*$
slice x iPAT	$F(1,19) = 0.92, p = 0.35$	$F(1,11) = 22.3, p < 10^{-3}$	$F(1,11) = 0.37, p = 0.5$	$F(1,13) = 10 - 3, p = 0.9$
slice x MB	$F(1.28,24.4) = 69.0, p < 10^{-3}*$	$F(1.4,15.2) = 206.5, p < 10^{-3}*$	$F(1.2,13.6) = 23.8, p < 10^{-3}*$	$F(1.2,15.6) = 299.3, p < 10^{-3}*$
iPAT x MB	$F(2.0,38.7) = 32.7, p < 10^{-3}*$	$F(1.5,16.8) = 12.9, p < 10^{-3}*$	$F(1.2,13.4) = 3.8, p = .07*$	$F(1.8,22.8) = 17.6, p < 10^{-3}*$

Table 5.3.1: Main effect and interaction significance of defined factors (by row as declared in the first column) over the measured tSNR in different brain areas (column 2-4, with the number of considered areas reported in parenthesis). Starred significance results indicate Greenhouse-Geisser corrected significance, here considered to cope with sphericity assumption violation. Non-significant interactions at 0.05 level are instead highlighted in red.

Different PEdir and slice orientations did not provide visually different residual geometric distortions once corrected and registered to the relative T1w reference. The image quality assessment (supplementary Figure 5.6.3) discarded axial settings with MB acceleration over 2 (due to structured artefacts content and ghosting) and discouraged the usage of iPAT (due to the observed central slabs of variable tSNR). Settings with MB factor 4 along coronal orientation were discarded because of non-tolerable artefact content (with iPAT) or possibly unstable sequence behaviour (without iPAT) under strong motion conditions resulting in non-trivial motion artefacts, not further investigated in this study where we

chose to maintain conservative accelerations levels.

Settings not availing of MB acceleration as well as with MB factor less than 3 along coronal orientation were discarded for insufficient temporal sampling capabilities (i.e. high repetition time). These results finally provided three suitable settings for FC evaluation, respectively based on MB/iPAT = 2/1 with axial orientation or MB = 3 with or without iPAT with coronal orientation.

5.3.2 FC AGREEMENT WITH DIFFERENT SEQUENCE SETTINGS

Considering the adequate settings provided in the section 5.2.2, we tested their agreement level in terms of estimated FC at single subject level to investigate differences attributable to the acquisition process.

The results of this evaluation were summarized in Figure 5.3.2. FC weights with different setting were found to be in high linear agreement with minimum R^2 of 0.81 comparing AXR1MB2 and CORR2MB3 settings.

Despite such high agreement level, significant departures from the linearity were found specifically involving CORR2MB3 which was, compared to the other settings, characterized by a lower FC amplitude as testified in Figure 5.3.2 by linear regression slopes greater than one (1.4 compared with AXR1MB2 or 1.37 with CORR1MB3), negligible offset and more sparse departures from the linearity specifically involving high correlation values, typically corresponding to intra-RSN links.

We did not observe strongly different linear associations respectively considering the between rather than within-RSN links as compared to the whole link set, rather a relatively sparser linear association considering high FC amplitudes nonetheless not clearly affecting the overall relation. A strong FC agreement was seen among AXR1MB2 and CORR1MB3 settings, comparable to the intra-setting agreement level, that is the linear agreement among the FC matrices obtained by averaging the FC of

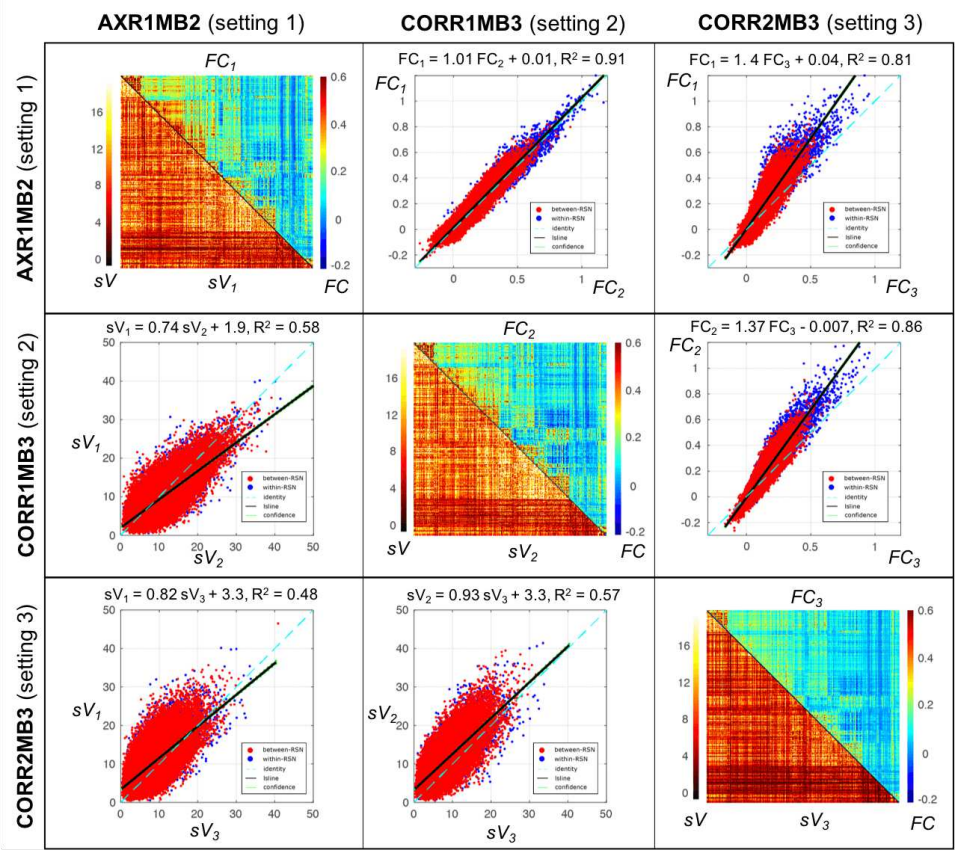

Figure 5.3.2: Representation of group average FC matrices using the three settings and inter-subject variability. The diagonal contains for each sequence setting (labelled by row/column) a matrix depicting the *average FC* (upper triangular) and between-subjects variability (*sV*) from the average FC (lower diagonal, standard deviation of FC across subject scaled by factor 100 for representation clarity). Out-of-diagonal squares represent the linear regression analysis of FC edge weights or sV estimates among couple of settings (indexed by row/column). Each box represents the distribution of edge values (red for between-RSN, blue for intra-RSN edges) paired by settings along with a least squares regression line (black, identified equation reported above) and associated 95% confidence intervals over the regression (green dashed lines), the identity relation is hinted by the dashed cyan-coloured line. For brevity of notation setting AXR1MB2 has also referred with index 1 (e.g. FC_1 and sV_1), setting CORR1MB3 with index 2 (e.g. FC_2 and sV_2) and setting CORR2MB3 with index 3 (e.g. FC_3 and sV_3) in this context.

(non-overlapping) random subjects sampled with same setting ($R^2 = 0.73 + / - 0.05 for AXR1MB2 and R^2 = 0.73 + / - 0.05 for CORR1MB3$, evaluated randomly sampling 100 times the runs obtained over five subjects to define two groups which average FC is then linearly regressed).

The linear agreement was similar also pooling all the acquisitions available ($R^2 = 0.86 \pm 0.04$ for AXR1MB2 and $R^2 = 0.84 \pm 0.05$ for CORR1MB3, randomly splitting 100 times the twenty acquisitions collected with each setting in two groups of 10/10 whose FC is being linearly regressed).

The inter-subject variability (labelled as sV in Figure 5.3.2, below diagonal boxes) in single links was sparser than the absolute FC agreement but nonetheless exhibited a significant linear trend comparing the FC variability with different settings. A proportionally higher sV was observed using COR settings as compared to AXR1MB2 (slope coefficients less than one) while relatively similar sV was observed among COR settings. No significantly different linear association was observed separately considering within- or between-RSN links (results were thus omitted for brevity).

We then evaluated whether the different sequence settings were able to provide consistent FC structures. To this extent, we linearly regressed the nodal features obtained by FC matrices derived from different settings across all nodes.

As reported in supplementary Figure 5.6.4, we found a robust STR association between AXR1MB2 and CORR1MB3 ($R^2 = 0.92$), between AXR1MB2 and CORR2MB3 ($R^2 = 0.75$)

or CORR1MB3 and CORR2MB3 ($R^2 = 0.83$).

The actual STR estimated with AXR1MB2 was proportionally higher than obtained with COR settings (regression slopes greater than one in supplementary Figure 5.6.4, first row) which were in even agreement of STR. A significantly positive STR offset was observed using other settings as compared to CORR2MB3, shifting the baseline STR by as much as 10% at low STR values. Similar considerations applied to the nodal EC measure, suggesting a very high agreement level among AXR1MB2

and CORR1MB3 (R^2 = 0.94) even with a minor scaling factor present and robust other settings ($R^2 > 0.7$). Both AXR1MB2 and CORR1MB3 settings provided proportionally lower EC measures (less than one slope in supplementary Figure 5.6.4, second row) in corresponding nodes as compared to CORR2MB3.

Node STR was significantly different across settings (Kruskal-Wallis test at node level, FDR corrected across 351 nodes with 0.05 rate) in 50.7% of the nodes, particularly affecting (with more than 50% of affected nodes) RSPT, SMH, SMM, AUD, CON, VAN, SAL networks.
Post-hoc comparisons (Wilcoxon ranksum, FDR corrected across nodes with 0.05 rate and Bonferroni among performed post-hocs) suggested that no significant differences of STR involved AXR1MB2 and CORR1MB3 settings (0/351 nodes) while different STR was found among AXR1MB2 and CORR2MB3 in 170 nodes or CORR1MB3 and CORR2MB3 in 67 nodes.

Node EC was significantly different across settings (Kruskal-Wallis test at node level, FDR corrected across 351 nodes with 0.05 rate) in 14.0% of the nodes, preferentially affecting AUD network for over than 50% of the nodes while other networks for less than 20% of their nodes.
Post-hoc comparisons (Wilcoxon ranksum, FDR corrected across nodes with 0.05 rate and Bonferroni among performed post-hocs) suggested that these differences were distributed among AXR1MB2 to CORR1MB3 for 17 nodes, AXR1MB2 to CORR2MB3 for 48 nodes and CORR1MB3 to CORR2MB3 for 11 nodes.

The previous linear agreement analysis was further explored to assess whether different sequence settings account for significantly different FC weights with a repeated measures 1way-ANOVA, separately carried out at edge-level (2 degrees of freedom for between setting effect, FDR corrected across edges, 0.05 rate).

Significantly different edges were depicted in Figure 5.3.3-A reporting the observed F statistic (left box) and significantly affected edges (right box) formatted as 351x351 matrices. Overall, 1.75% of the edges (1076/61425) exhibited significant FC differences (2.06% referring only to significantly non-null edges, determined by a one sample t-test per-

formed to compare the average Fisher-transformed edge weights over all settings with zero, FDR corrected with 0.05 rate) and involving 255 over 351 (72.7%) of the nodes.

Figure 5.3.3-A showed that the connectivity within and between sensory-motor (SMM, SMH, AUD) networks (with 18.4%, 12.7% of affected edges respectively within and between networks) as well as within cingulate (CON, 19.4% affected edges) and between CON and AUD nodes (11.8% affected edges) was significantly affected by the used setting. Connectivity among subcortical (SUB) nodes was similarly affected (21.6% of the edges) along with the connectivity among SUB and CP or SAL nodes (respectively involving 14.4% and 18.0% of the between network edges).

In Figure 5.3.3-B, affected functional connections were spatially represented for involved nodes (Figure 5.3.3-B, green mark) and their affected connections (Figure 5.3.3-B, red lines with thickness weighted by the associated F statistic value) overlaid to the brain cortical and subcortical node set in transparency.

This spatial representation clarified that the observed differences involved areas situated in sensory-motor, auditory or salience cortex and subcortical nuclei distributed around central to lower brain areas. Specifically, the connectivity among these areas often interested inter-hemispheric connections rather than few strong effects observed in the same hemisphere.

Post-hoc comparisons (suppl. Figures 5.6.5 performed between the FC matrices obtained by couples of settings highlighted that most of group-significant edges were nonetheless related to FC differences between AXR1MB2 and CORR2MB3 settings (involving 1.3% of the links while a minimal fraction ($< 0.1\%$) of the edges was different among CORR1MB3 and CORR2MB3 also exhibiting a sparse pattern over the FC matrix suggesting randomly distributed errors hardly affecting inter-hemispheric connections.

No significantly different links were observed between AXR1MB2 and CORR1MB3 settings. A decreasing FC amplitude mediated most of the

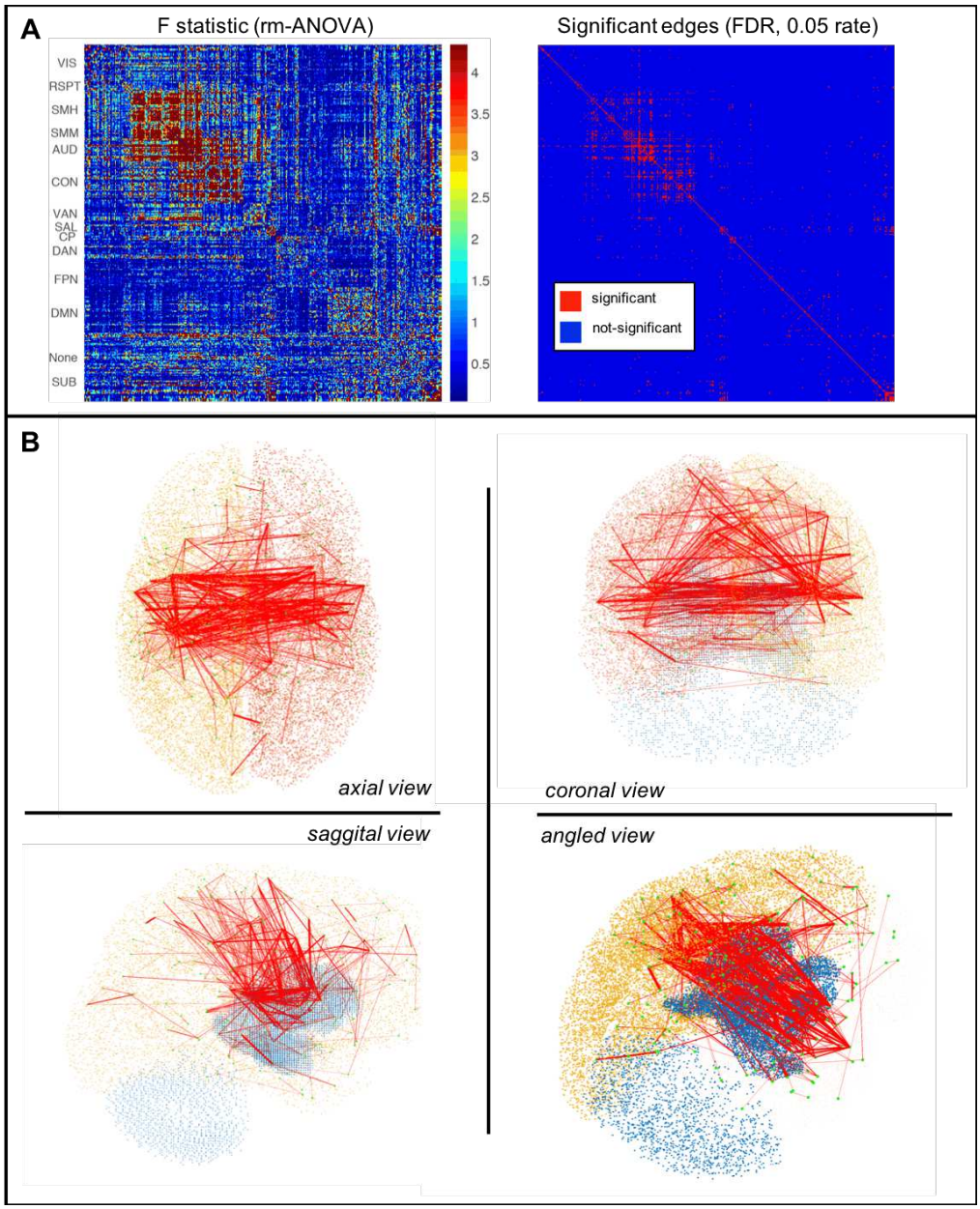

Figure 5.3.3: (A) Significance results of 1way-ANOVA test applied at edge-level, reporting the estimated F statistic (left box) and significantly different edges across the three settings (right box, FDR corrected at 0.05 level across multiple edges). Significantly affected edges were further spatially depicted in (B) in overlay to a typical brain representation for left hemisphere (yellow) right hemisphere (light red) and subcortical (blue) areas. Functional areas with affected edges are represented in bright green (circled) while the affected connections in bright red (thickness modulated proportionally by the relative F-statistic of the edge comparison) under four typical brain perspectives.

observed differences among AXR1MB2 and CORR2MB3, with lower FC at higher total acceleration, whereas differences of FC among AXR1MB2 and CORR1MB3 settings were not consistent in sign across edges (single tail post-hoc, pair-wise t-test, 0.05 level FDR).

The statistical comparison performed with a non-parametric Kruskal-Wallis test in place of the 1way-ANOVA for the setting factor (FDR corrected across edges, 0.01 rate), reported a consistently similar pattern of FC differences, however reporting an increased fraction of affected nodes, non-trivially explicable considered the actual limitations of sample distribution and size. Nonetheless, edge-level differences by means of Kruskal-Wallis test involved 11.3% (6957/61425) of the edges (13.0% referring to the number of non-null edges determined by means of Wilcoxon signed rank test at edge level testing if the median Fisher-transformed edge weight over all settings was significantly non-zero, FDR corrected with 0.05 rate), interesting 345 over 351 (98.3%) nodes.

5.3.3 Are these FC differences related to the noise enhancement across settings?

We further investigated whether previously found FC differences could be associated to noise propagation effects, caused by the image accelerations delivered with different settings. To this extent, we linearly regressed the FC weights to the tSNR product of connected nodes across all the acquisitions (60 points = 5 subjects x 3 settings x 2 PEdir x 2 sessions), separately for each matrix edge.

The linear association was found to be statistically significant in 7.3% of the edges as shown in supplementary Figure 5.6.6 (first row) (F-test on linear regression model consisting of an offset and tSNR product across acquisitions, FDR corrected across edges with 0.01 rate). Coherently, the Spearman correlation among these variables was significant in 8.3% of the FC edges (FDR corrected across edges with 0.01 rate) as reported in supplementary Figure 5.6.6 (second row). Out of 1077 significantly different edges across settings, 884 (82.1%) exhibited a significant association

between FC weights and tSNR product of connected nodes. A similar proportion (929 out of 1077 nodes, 86.3%) held using the Spearman correlation, overall confirming the pattern similarity observed in Figure 5.3.3 and supplementary Figure 5.6.6 (second row) respectively for edges affected by the setting factor and FC edges whose weights were associated to the tSNR.

Significantly different edges across settings, detected by means of Kruskal-Wallis test (FDR corrected across edges with 0.01 rate) instead of 1way-ANOVA test, were proportionally less associated to the tSNR product (3566 out of 6958 nodes, 51.2%). However, lowering the FDR correction rate to detect edges progressively more affected by the setting factor (i.e. from FDR rate 0.01 to 10-4), the proportion of edges whose FC was also associated to the tSNR product was of 1197 over 1509 (79.3%) by means of Spearman correlation. Omitting from these proportions the edges whose weight is not significantly different from zero at group level (paired t-test, 11 dof, FDR corrected across edges at 0.05 rate) did not considerably change the results.
The FC edges exhibiting such an association with tSNR product were more often within-RSN links (i.e. edges typically with high FC weights) with a relatively sparse prominence over VIS, DMN and DAN networks while a more consistent pattern involved the connectivity of SMH, SMM, AUD, CON and SUB networks.

Post-hoc tSNR comparisons (one-tail Wilcoxon ranksum test, FDR corrected across nodes with 0.05 rate and Bonferroni across post-hoc tests) suggested AXR1MB2 provided higher tSNR than CORR1MB3 in 0/351 areas and lower in 6/351; AXR1MB2 provided higher tSNR than CORR2MB3 in 337/351 areas and lower in 0/351 and finally CORR1MB3 provided higher tSNR than CORR2MB3 in 343/351 areas and lower in 0/351, confirming the tSNR similarity of AXR1MB2 and CORR1MB3 and the lower tSNR with CORR2MB3.
Post-hoc comparisons repeated after rescaling the tSNR of CORR2MB3 by a $\sqrt{2}$ factor, made the overall tSNR pattern across ROIs of relatively

similar amplitude to the other settings. However, higher tSNR was nonetheless observed using AXR1MB2 than CORR2MB3 in 116/351 areas and lower in 104/351 whereas higher tSNR was observed by using CORR1MB3 rather than CORR2MB3 in 264/351 areas and lower in 0/351.

The relatively similar tSNR amplitude along different settings suggested, despite the significance of observed differences, that CORR2MB3 and AXR1MB2 basically share a comparable tSNR pattern once corrected for noise scaling effects (i.e. $\sqrt{2}$) related to iPAT while the tSNR provided by CORR1MB3 was consistently highest with nonetheless similar pattern across ROIs.

After the tSNR rescaling, we still observed a consistently lower tSNR only in AUD and SUB areas (see supplementary Figure 5.6.7 for tSNR patterns across ROI with/out $\sqrt{2}$ factor applied) using CORR2MB3 as compared to CORR1MB3 (or similarly AXR1MB2), in agreement to the expected g-factor spatial pattern of noise enhancement instead expected to be less marked in central brain areas without iPAT acceleration.

The connectivity of these networks remained consistently associated to the tSNR even after such tSNR rescaling while the involvement of other RSNs was found significantly sparser than the previously observed association pattern (see supplementary Figure 5.6.6) also maintaining a solid association in edges linking SUB to SAL and CP networks. Notably, AUD and SUB along with CP and SAL were also the networks previously observed to have a significantly affected FC across settings (see Figure 4).

5.4 Discussion

Within the established framework described in Chapter 3, we studied the noise propagation effects over the functional connectivity provided by experimental parameters typically not optimized from the FC perspective such as the image acceleration. Our aim was to evaluate the FC estimation reliability in single subjects (Gordon et al., 2017) employing PET/MRI scanners simultaneously providing experimental optimisation guidelines for the researcher ensuring a limited impact over the FC structure, a fundamental asset for the enhancement of FC potential to uncover the true underlying connectivity of the brain.

To this extent, the experimental limits of MB-EPI sequences were explored in PET/MRI scanners evaluating their feasibility for FC estimation at standard neuroscience spatial resolution (3.0 mm) with maximal temporal resolution (i.e. minimum TR) but whole-brain coverage. Such experimental requirements were satisfied through slice- (MB) and in-plane (parallel imaging, iPAT) image accelerations. As observed in (Todd et al., 2017), increasing MB and iPAT factors introduces a spatially inhomogeneous noise propagation, non-trivially explained by the acceleration interaction (Risk et al., 2018; Todd et al., 2017).
We strived to disentangle these acceleration effects in order to maximize their advantages by pursuing an experimental optimisation task consisting of a two-stages protocol. A first set of scans was collected spanning the space of acceleration factors (MB, iPAT) along two slice orientations (axial, coronal) to identify which protocols provides adequate BOLD sensitivity (tSNR as suggested in (Wald and Polimeni, 2017)) and overall fMRI image quality with our setup.

These three experimental factors (slice orientation, iPAT, MB) accounted for significant tSNR differences in agreement with the theoretical predictions regarding the receiver array performances and experimentally demonstrating why MB-accelerated fMRI scans benefit from non-transversal 2D slices in our scanner setup. Coronal 2D slices, indeed provided higher and more spatially homogeneous tSNR as compared to equi-accelerated

axial scans. Considered the cylindrical geometry of the coil array, sagittal slice are expected to enhance the supported MB as well, not considered in this study to limit the protocol duration.

Interestingly, the interaction between MB and iPAT accelerations was modulated by the slice orientation, confirming how the usage of different slice prescriptions could more or less effectively support image acceleration from a tSNR perspective. Note that the tSNR observed at different iPAT levels was independent from the slice orientation (once accounted for the $\sqrt{(R)}$ factor (Breuer et al., 2009)), suggesting that the receive array similarly supported parallel imaging along the two orthogonal slice orientations (Ohliger and Sodickson, 2006) tested.

This interaction effect also accounts for the general observation of a tSNR monotonically non-increasing with MB (Risk et al., 2018). Instead, exploiting peculiar differences of the receive array, we were able to demonstrate few conditions where this is not actually true: MB factor 2 axially generally lower tSNR than MB factor 3 with coronal slices. This was taken to the extreme case where the interaction among MB and iPAT is resolved along coronal orientation: condition under which the tSNR was not significantly affected by increasing MB factors or in other words no tSNR penalty is introduced by MB acceleration. Potentially, the maximum MB factor (MB = 4) is not even the maximally supported, at least in terms of noise enhancement.

Considering the spatial pattern of tSNR homogeneity observed along coronal orientation without iPAT (not recalling the SNR_0 appearance that suggest thermal noise regime neither the anatomy of brain tissues suggesting a physiologically-dominated noise regime) we conjecture this condition is actually balancing the noise propagation without reaching the thermal noise regime whereas axial runs ($MB > 1$) exhibited a marked tSNR discontinuity across slices around the FOV centre, an effect attributable to discontinuous temporal signal variance, discouraging its use for FC particularly when using with iPAT (inconsistent across subjecs without iPAT).

Different slice orientations did not enhance the tSNR in frontal brain areas (regardless of iPAT), that is no further tSNR improvement is obtained once axial slices are tilted (improving the signal dropout) as compared to coronal orientation, whereas in temporal, subcortical or regular (not typically involved in heavy geometrical distortions or dropout effects) areas the coronal slice orientation entailed a significant tSNR advantage in agreement to the whole-brain results by using an appropriate combination of slice orientation and iPAT. The clearest improvements offered by coronal orientation were observed when using iPAT (negatively interacting with MB with axial slices) whereas, omitting iPAT, the coronal benefit was substantial only for subcortical and regular areas.

We extended previous studies where the optimal MB factor (i.e. provides maximum tSNR) was found to be region-dependent (Todd et al., 2016) by reporting that is also slice-orientation dependent. Specifically, it depends on the receive array configuration and imaging FOV which contribute to set the actual spatial pattern of SNR_0 or noise enhancement effects. Maximal tSNR was achieved in most of the brain areas using minimal MB acceleration (MB $<=$ 2) along axially orientated slices while the usage of iPAT basically discarded any MB factor in agreement with the negative factor interaction previously observed. Conversely, the locally maximum tSNR with coronal slices is achieved employing MB factor 2 in most of the brain areas and regardless of iPAT usage, with a small but significant fraction of areas exhibiting maximum tSNR at even higher factors (MB $=>$ 3) arguably due to the lower distance from the array coil receiving elements observing the concerned parietal and occipital brain areas.

Out of all evaluated settings, three were deemed adequate for FC: two based on coronal slice orientation (MB=3, both with and without iPAT), while the third was axially oriented (MB=2, without iPAT). Regarding the noise regime of these settings, only the iPAT-enabled one appeared to provide thermal noise regime, while the others exhibited spatially homogeneous tSNR without signatures amenable to physiologic rather than thermal noise regimes, but favourably balancing these noise sources for

maximal tSNR. Further processing steps required for FC analysis (e.g. registration, resampling and confound regression) are expected to shift these observed noise regimes toward the thermal-like dominated, yet maintaining high BOLD sensitivity (Triantafyllou et al., 2011; Wald and Polimeni, 2017).

Recalling the derivations proposed in Chapter 3, a relation is to be expected among FC and temporal noise content. To experimentally verify this effect we collected a second set of lengthier fMRI measurements (suitable for FC assessment) making use of the three adequate settings previously identified. We matched the imaging parameters other than acceleration and employed same pre-processing to ensure similar physiological noise content and signal level to make the tSNR especially sensitive to the thermal noise propagation if compared across differently accelerated settings (i.e. expected to provide increasing levels of noise propagation by means of decreasing tSNR).

In fact, even if the thermal noise regime provides desirable statistical features nonetheless beneficial also for the validity of FC statistical inferences, an upper bound exist in the amount of actual temporal variability a single acquisition can afford before losing the sensitivity to single functional connections.
We observed that FC by means of Pearson linear correlation is explicitly a decreasing function of thermal noise level which could be enhanced up to the point of causing a loss of FC amplitude and its statistical significance.

Unfortunately, this limit could be both spatially dependent (according to the SNR_0 modulated by g-factor) and related to the co-activity strength expressed by different brain areas (possibly in a subjective fashion (Rangaprakash et al., 2018) masking recently found biological metabolic support or resting state brain networks (Aiello et al., 2015; Passow et al., 2015; Riedl et al., 2014; Tomasi et al., 2013).

The brains FC is currently not meant to precisely characterize the coupling among two brain areas (e.g. its directionality). Rather, it aims to test their correlation against a null hypothesis of uncorrelation (Friston,

2011). Experimental settings suitable for FC assessment should therefore guarantee the absence of any significant structural bias and correlation patterns (or loss of it) susceptible to the acquisition process. The FC measures provided in corresponding edges with the three settings were found to be in high linear agreement: weak links with one setting were consistently characterized as weak with others. Similarly, robustly associated areas (high FC) with one setting generally exhibited robust association also with others. However, the actual FC amplitude of the strongest edges was more sparsely estimated by different settings as compared to weak edges. That is, despite the high linear agreement across settings, a significant spoiling effect acted over the strongest connections: arguably the within-RSN ones. This effect was particularly clear observing the within-RSN connectivity estimated with CORR2MB3 setting both lower and sparser than other settings (AXR1MB2, CORR1MB3), instead in much higher agreement.

This observed decrease of FC was nonetheless in agreement with the expected noise propagation across settings: the higher the acceleration (i.e. higher noise propagation), the lower the actual correlation due to the increased temporal standard deviation (see Chapter 3) by virtue of the nearly matched experimental conditions. Only the connectivity among areas of the visual network was preserved across all the three settings, while the agreement among AXR1MB2 and CORR1MB3 was generalized, demonstrating their FC equivalence and leaving to the researcher an experimental degree of freedom to be possibly spent in enhanced FOV rather than spatio/temporal sampling.

The FC estimated by means of different settings specifically differed within middle brain areas encompassing auditory, subcortical and sensory-motor networks. At the highest acceleration level (CORR2MB3), the connectivity of such areas was impaired to the point of possibly losing the statistical significance at group level, mimicking dysconnectivity phenomena otherwise observed in neuropathology (Badea et al., 2017) but nonetheless able cover possible connectivity differences among subjects.

Overall, the FC amplitude was found to be associated to the tSNR

product of linked areas in less than 10% of the edges. However, this proportion was remarkably higher among edges significantly different across settings (more than 80%), where the positive correlation observed among FC amplitude and tSNR product well agreed with the predicted FC loss. We also found that the more the FC amplitude is affected by the setting used, the clearer is the association of such a FC measure with the tSNR. This observation, together with the spatial pattern of areas exhibiting significantly different connectivity across settings, suggested us that the thermal noise enhancement, spatially described in terms of g-factor (typically greater than one right over mid-brain areas) is responsible for these structured FC differences, in good agreement with theoretical expectations.

Importantly, the association between FC amplitude and tSNR in setting-affected edges was not resolved taking into account the spatially homogeneous loss of SNR_0 given by parallel imaging (i.e. $\sqrt{(R)}$, with R the parallel imaging acceleration factor), it rather depends on the different spatial inhomogeneity pattern of SNR_0 exhibited by different settings (i.e. the g-factor) highlighting that it is not only important to maximize the amplitude of the tSNR but also its spatial homogeneity to provide unbiased FC estimates.

Graph theory-based measures of network structure such as the node strength was confirmed to be sensitive to the actual setting integrating the actual FC bias previously observed at higher acceleration while maintaining a high linear association.

There are limitations of this study that should be noted.
To accommodate for protocol duration limits, the two implemented experimental protocols explored a limited portion of the parameter space for MB/iPAT accelerations and slice prescription with fixed data processing regarding denoising and FC estimation. Physiologically similar conditions and narrow age range were ensured to control for physiological noise variability across subjects and sessions. Since all comparisons were carried out at single-subject level the authors did not expect significant

sample size effects, rather to generalize the results regarding group-level comparisons, an effectively higher sample size would be needed.

5.5 CONCLUSIONS

We are assisting to a paradigm shift in brain functional connectivity which is stepping from the phenomenological characterization of the human brain fundamental features (e.g. small-worldness, efficiency, hubness, etc.) to the its quantitative assessment, an asset considering how brain functional structure characterization could be useful pathological biomarkers.

We built upon previous considerations about favorable noise conditions to be achieved in fMRI experiments in order to make the typical statistical assumptions more experimentally fulfilled while limiting the impact of spurious spatial autocorrelation, overall improving the validity of the performed inferences. We reframed this concept from task-fMRI literature to the typical functional connectivity study, theoretically demonstrating how the noise amplitude and mixture interplay when the fMRI signal of two areas is being associated instead of just one. In particular, the thermal noise propagation of the associated areas can directly lower their connectivity whereas close attention should be paid to the locally defined balance among thermal to physiological noise ratio, ultimately function of the experimental setup and chosen sequence settings. This suggests that the FC structure can be amplitude-modulated according to the actual noise regime and level, possibly resulting in a loss of significance for some connections rather than masking interesting effects in others.

We demonstrated this effect during a two-stage experimental optimization task. First, we explored the parametric space of image acceleration (MB, iPAT) along two slice orientation to identify sequence settings suitable for FC studies overcoming current hardware setup limitations that could impair MB imaging potential. Out of the complex interplay between various sequence factors, we provide strong evidence in favor of non-transversal 2D slice orientations to make the most of MB acceleration within the available setup (Siemens mMR Biograph, Head-Neck 12-channel coil array).

Three settings with adequate sampling performance offered increasing levels of image acceleration (both MB and iPAT), these were employed with matched parameters in a test/retest fashion to acquire FC matrices of each subject. The FC matrices obtained with these settings exhibited structured differences affecting various middle and lower-brain areas, whose connectivity was positively correlated to the tSNR loss experienced in these areas with increasing image accelerations. These differences as well as their correlation with tSNR were strikingly related to a significant loss of tSNR (due to iPAT usage) clarifying that FC structural alterations can be attributed to significant tSNR variations, while minor-to-no FC differences are to be expected at single-subject level otherwise (in our study defined by the MB factor, slice orientation, phase encoding direction).

Moreover, the association of FC to tSNR in edges with connectivity affected by the setting, was still significant accounting for spatially homogenous losses of tSNR (as from $\sqrt{R}$ in iPAT) suggesting an important role regarding the g-factor spatial pattern of noise enhancement, consistent with the position of areas showing altered FC. Based on these observations we encourage the use of different slice orientations to exploit MB-acceleration while enhancing fMRI scanning performances and BOLD sensitivity. However, the actual noise content and regime should be carefully considered to guarantee appropriate FC robustness and possibly offer more than one protocol with comparable estimation capabilities to provide a FC consistency check at single-subject level. Even though noise arguments foreseen the observed FC differences, more studies are needed to provide guidelines and make the FC estimation more robust to the actual noise behaviour, providing more consistent definition for brain functional connectivity.

5.6 SUPPLEMENTARY FIGURES

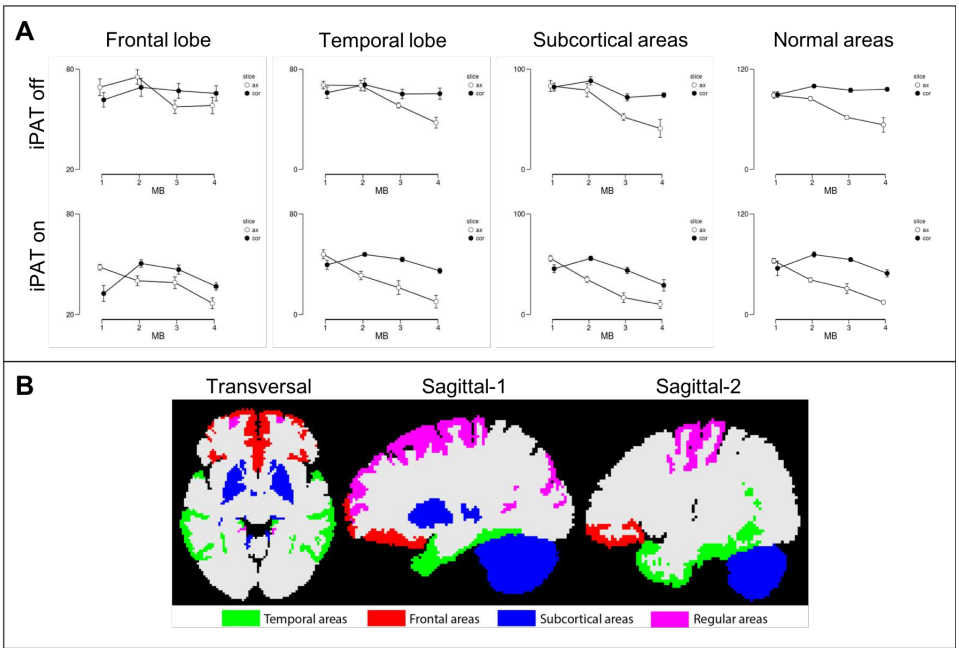

Figure 5.6.1: (A) tSNR marginal means respectively in frontal (first column from left), temporal (second column), subcortical (third column) and regularly sampled areas (fourth column). The tSNR marginal mean across specified factors is represented while increasing the MB factor and separately reporting the tSNR of axial acquisitions (white circles) and coronal (black circles) while different rows the iPAT factor employed (top row for R=1, bottom row for R=2). (B) The spatial location of evaluated brain areas of frontal (red), temporal (green), subcortical (blue) and regularly sampled areas (purple) is reported on the bottom map for a standard brain reference space.

Slice	iPAT	Frontal areas		Temporal areas		Subcortical areas		Regular areas	
AX	On	64.8 (13.9)	40.9 (9.5)	56.6 (14.4)	26.0 (13.7)	56.7 (18.9)	23.2 (16.7)	78.9 (16.1)	35.4 (17.6)
COR	Off	65.1 (15.8)	40.8 (9.9)	61.4 (13.1)	39.8 (8.2)	78.5 (9.9)	44.5 (10.4)	94.0 (6.3)	62.9 (9.7)

Table 5.6.1: Median and median absolute deviation (by parenthesis) of the tSNR distributions in different brain areas. Representative values are respectively reported separating by slice orientation (AX for axially oriented, COR for coronally oriented) and iPAT factor (On for R=2, Off for R=1).

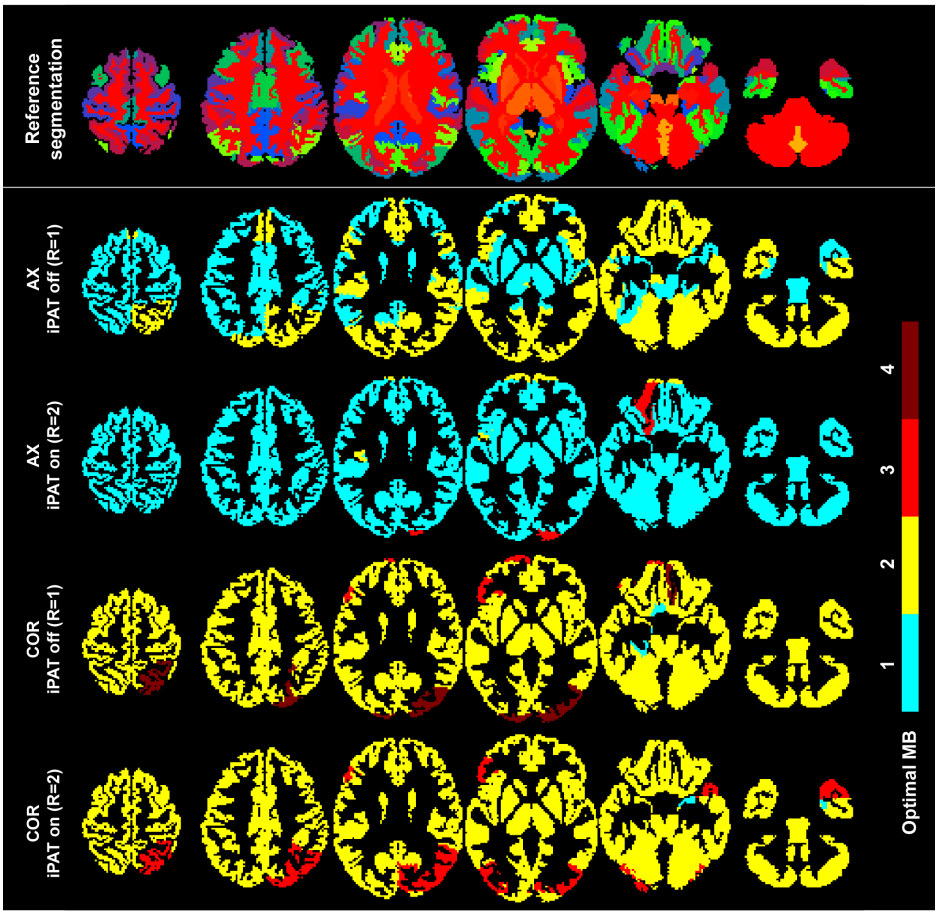

Figure 5.6.2: Number of brain areas exhibiting maximum tSNR in correspondence to each MB factor, separately reported for different slice orientation and iPAT factor. Each bar height is scaled by the number of areas found to exhibit maximum tSNR in correspondence to the specified MB factor. Optimal MB factors occurrences are separately reported by different combinations of slice orientation and iPAT factors to highlight possible optimal conditions of the MB acceleration depending over the interaction with other sequence settings.

Slice/iPAT	Slice/iPAT	Frontal areas		Temporal areas		Subcortical areas		Regular areas	
AX / 1	AX / 2	¡ .0001	8.5	¡ .0001	6.2	< .0001	6.0	< .0001	6.8
AX / 1	**COR / 1**	**0.85**	**-0.2**	**0.086**	**-1.7**	**0.0011**	**-3.2**	**< .0001**	**-6.9**
AX / 1	COR / 2	< .0001	7.7	< .0001	4.1	< .0001	4.7	0.0001	3.8
AX / 2	COR / 1	< .0001	-8.1	< .0001	- 7.4	< .0001	-8.1	< .0001	-9.1
AX / 2	**COR / 2**	**0.28**	**-1.1**	**< .0001**	**-4.2**	**0.0002**	**-3.7**	**< .0001**	**-5.4**
COR / 1	COR / 2	< .0001	7.5	< .0001	6.3	< .0001	8.0	< .0001	9.1

Table 5.6.2: Statistical comparison of the observed tSNR between factor combinations (slice orientation x iPAT) stated in column 1 versus column 2. For each performed comparison (by row) a Wilcoxon rank sum test was performed between samples (Bonferroni corrected across multiple comparisons to correct the base 0.05 significance level) with obtained significance separately reported for each tested area (frontal, temporal, subcortical, regularly sampled areas) in the respective left column and z-score difference (first second combination as defined by the selected factors) on the right.

Figure 5.6.3: Summary of image quality assessment of P1 protocol. Color-coded boxes respectively report criteria satisfied (green), limitedly satisfied (yellow) or not satisfied (red). Overall acceptable results are side-checked by a green mark highlighting sequence settings overall providing adequate imaging performances.

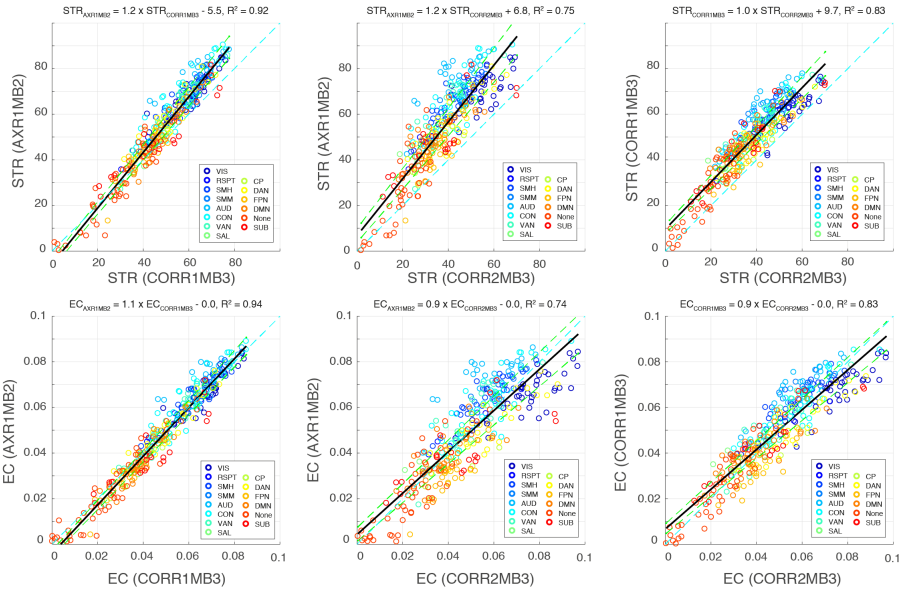

Figure 5.6.4: Linear agreement of node strength (STR) and eigenvector centrality (EC) estimated from FC group matrices with different sequence settings (reported by lateral labels). Nodes are colour-coded according to their belonging RSN (see lateral legend). Specifically, each box report the metric value (STR in the top row, EC in the bottom row) observed in corresponding nodes but different settings along with their least squares regression line depicted in black along with the associated 95% confidence intervals over the regression line (green dashed), the identified equation is instead reported in the relative caption. The relation identity is graphically represented by the dashed cyan-coloured line.

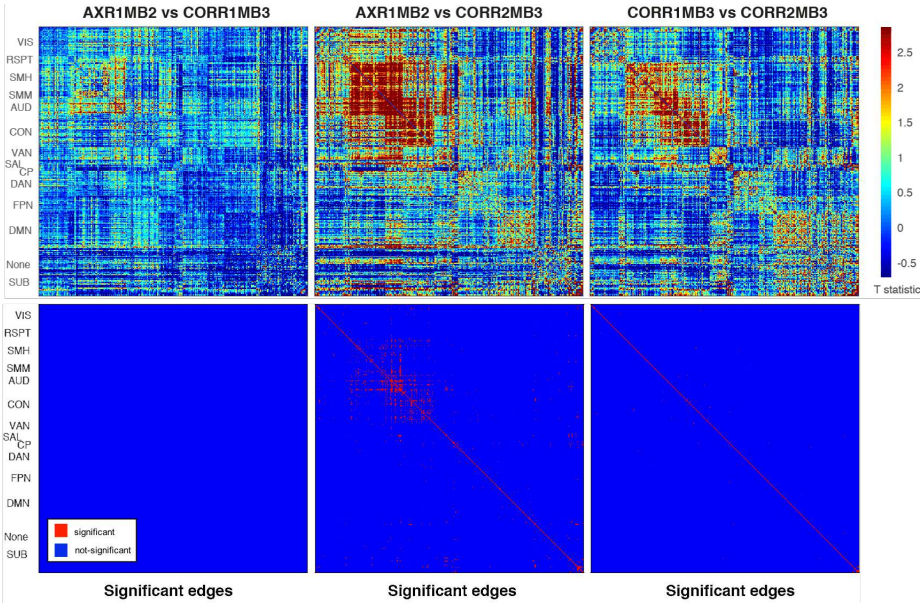

Figure 5.6.5: Significance of post-hoc comparison between couples of sequence settings (AXR1MB2 vs CORR1MB3, AXR1MB2 vs CORR2MB3, CORR1MB3 vs CORR2MB3 respectively reported along indexed columns) performed by means of paired sample t-test (FDR rate 0.05 for each comparison and additional Bonferroni correction across multiple couples compared) the rm-ANOVA test applied at edge-level over all 352 nodes. Top row reports the T-statistic estimated at edge-level for each post-hoc comparison while the bottom depicts edges exhibiting significantly different connectivity among settings (red for significant differences, blue for non-significant).

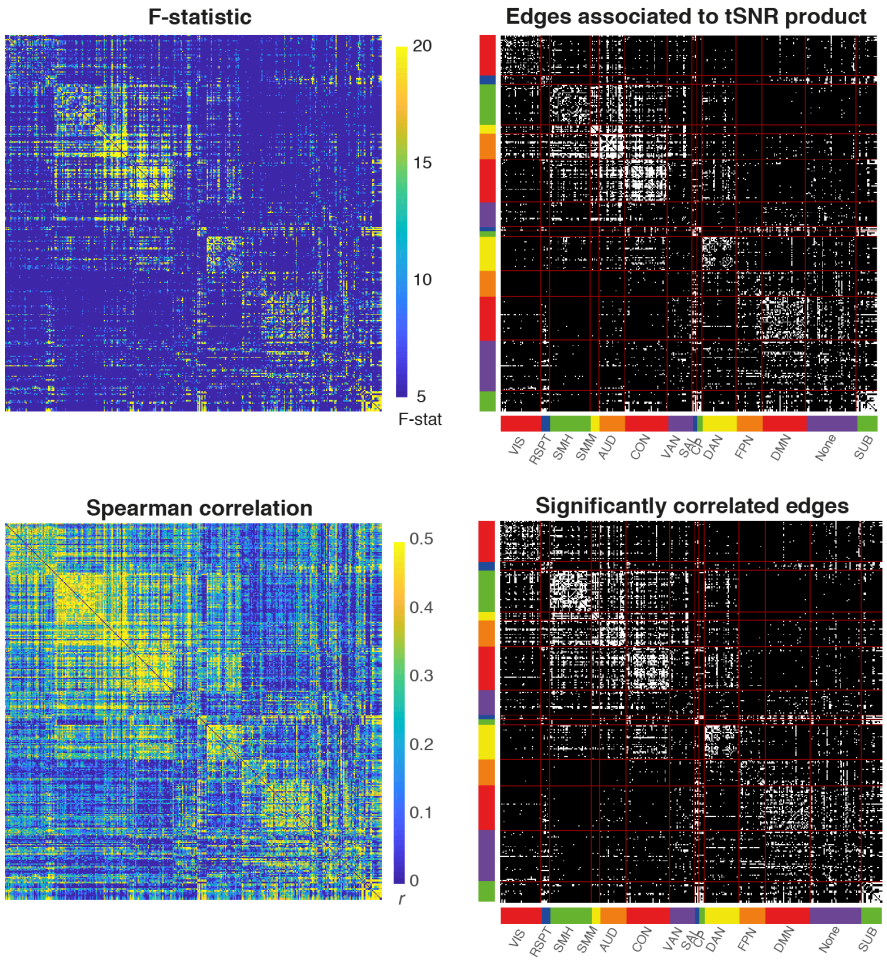

Figure 5.6.6: Linear association of FC amplitude and tSNR product of connected areas across acquisitions. Top row shows for each FC edge position the significance level of the linear model (F-statistic box top-left) and edges (top-right) where such a linear association is statistically significant (white) or not (black) in overlay with the network segregation (red lines) colour coded according to the connecting network. Results from Spearmans rank correlation among FC values and tSNR product across acquisitions (bottom-left) and edges where the actual correlation (bottom-right) was statistically significant (white) or not (black) across all edges (FDR corrected at 0.01 rate) in overlay with the network segregation (red lines) colour coded according to the connecting network.

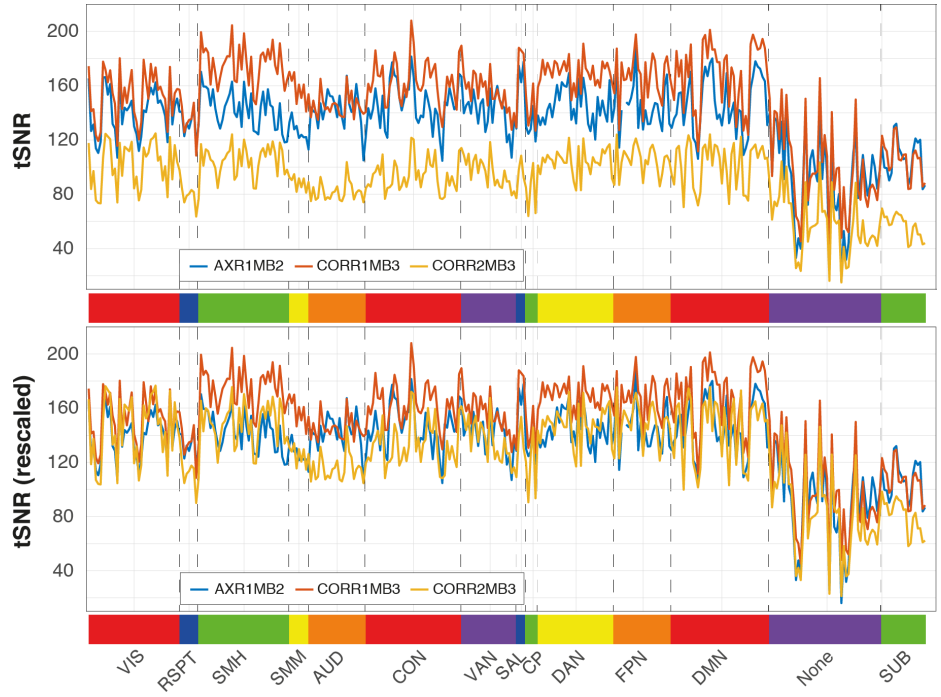

Figure 5.6.7: tSNR representation at group level with different sequence settings and across all 351 ROIs, organized by belonging network (colour-coded). Top row report the measured tSNR (averaged at group-level) while the bottom row depicts the tSNR distribution rescaling for $\sqrt{R}$ acceleration effects as attributed to iPAT usage in the CORR2MB3 setting.

6

Brain cortex segmentation framework for FC applications

In this chapter we formulate a framework to support accurate brain cortical segmentation. The relevance for state-of-the-art FC pre-processing will be discussed along with the generalization of current structural MRI data processing.

The aim was to change the traditional structural MRI processing, which provides the geometrical support of many FC studies, to a more robust and flexible design for brain cortical segmentation which minimizes manual interventions on the images and maximize the comparability across subjects with eventually enhancing the sensitivity of subsequent FC analyses to single subject effects.

The rationale of the proposed framework will be discussed reporting the framework and sequence design principles followed. The chapter is completed by some commented preliminary results that highlight the potential of the framework as well as the encountered limitations to shed light on critical steps that would guarantee further development.

This study was carried out in collaboration with Prof. Cloos and Prof. Lattanzi during an internship period at the New York University (NYU) - Center for Advanced Imaging Innovation and Research (CAI2R), developing the framework and required MRI sequences using locally available scanning and software facilities.

6.1 THE IMPORTANCE OF BRAIN SEGMENTATION FOR FC

The investigation of brain functional connectivity discussed in the previous chapters, fundamentally relies on the accurate alignment of brain spatial locations hypothesized to be functionally consistent across subjects.
After typical fMRI pre-processing (volume realignment, filtering and eventually confound regression), fMRI data is registered to a structural image and parcelled according to a chosen atlas for further FC analysis.
FMRI confounds to be regressed are typically extracted by processing fMRI data extracted from CSF and WM tissues (i.e. not providing significant BOLD contrast) while accurately preserving GM brain areas.
Therefore, suitable segmentation for these tissues as well as a correct whole brain mask that removes skull and out-of-brain contributors is fundamental to estimate CSF-related fMRI signal variabilities as well as to ameliorate the partial volume effect affecting GM voxels (Jo et al., 2007).
To avoid mixing up the fMRI signal contribution from different tissues (e.g. GM with WM or CSF), its customary to restrict the spatial delineation of brain areas (derived from an atlas) to weight only voxels supposed to contain the signal of interest (i.e. GM) while de-weighting others that consistently participate in the mixture of different GM parcels resulting in an inflated FC measure among these parcels.

Recent rs-fMRI literature conveyed that even at single subject level, FC estimation could be highly repeatable and comparable across modality (e.g. task vs. rest as found in (Gordon et al., 2017)) yielding important brain features provided that a sufficient amount of fMRI data is available.

To capitalize on recent experimental developments (e.g. MB-EPI imaging) and denser sampling, appropriate data compression schemes are needed while maintaining without losing information.
As an example, fMRI data can be effectively collapsed along the cortical thickness dimension assuming a homogeneous functional response along such direction (i.e. under typical fMRI spatial resolutions) thus representing the GM local response as coming from a single surface vertex rather than few volumetric voxels covering the cortical ribbon.

6.1.0.1 THE BRAIN CORTEX AS A SURFACE

The main idea underlying cortical surface generation is to avoid functionally redundant volumetric representations by modelling the cortical gray matter sheet as a set of vertices representing a 2D surface. In this way, vertices uniformly covering the entire cortex will separately represent spatial locations corresponding to left and right hemispheres while accounting for individual anatomical gyri and sulci variability.
To provide an average sampling resolution (average vertex spacing) on the surface of 2 mm, approximately 30000 vertices are required per hemisphere (Glasser et al., 2013) while to provide an average vertex spacing approximately 80000 vertices are needed.
The cortical surface would be represented by the adjacency of indexed vertices and the spatial location of each indexed vertex. Regarding fMRI, pre-processed data in the same space as a delineated cortical surface would be accordingly sampled by taking an average of the fMRI signal local to each vertex thus providing a vertex-related dynamic.

6.1.0.2 SURFACE DELINEATION ERRORS

The complexity of cortical surface delineation process had been tackled by many methods, typically requiring carefully acquired and pre-processed structural images to represent the brain anatomy (e.g. T_1-w MPRAGE or T_2-weighted volumetric images) which suffers from coarse intensity inhomogeneity eventually caused by transmit and receive fields

inhomogeneity.

Even if methods exist to cope with these effects, residual intensity bias combined with image artefacts (e.g. arising from motion or sequence limitations) could result in a loss of contrast between brain and non-brain tissues (see 6.1.1-A) such as the meninges (among which the dura is often the only MRI-visible) ultimately resulting in surface delineation errors or poor subcortical segmentations (e.g. thalamus, pallidum, cerebellum, etc.). The cortical delineation process can fail locally or at whole-brain level.
Whole brain delineation errors consist in cortical surfaces completely or partially out of brain and are typically determined by poor skull-stripping results due to improper subject positioning or excessive intensity bias.

However, typically the pre-processing of structural images proceed smoothly but the delineated cortical surface (e.g. by means of Freesurfer (Fischl et al., 1999)) exhibit local delineation errors associated to a locally poor image contrast. These errors more often consist in a poorly delineated pial surface (i.e. the boundary between GM and meninges or CSF) not strictly delineating the GM cortex from CSF but locally encompassing extensive CSF portions, subsequently considered as GM in further analysis. Instead, the delineation of GM from WM is typically more robust, eventually suffering only from very poor GM/WM contrast or SNR.

As illustrated in 6.1.1-B, the accurate distinction between brain tissues and meninges in condition of limited SNR is not guaranteed with same accuracy in the whole brain because the meningeal layers (specifically the dura structure for its possible MRI-visibility), have a T_1 relaxation relatively similar to GM (thus similar intensity in T_1-w images) but variable thickness and spacing from the pial surface.

These delineation errors, introducing CSF-like signals as if it were GM during the surface sampling process, will mix spurious fMRI signals (CSF, WM) other than GM (with impact dependent upon the GM ribbon thick-

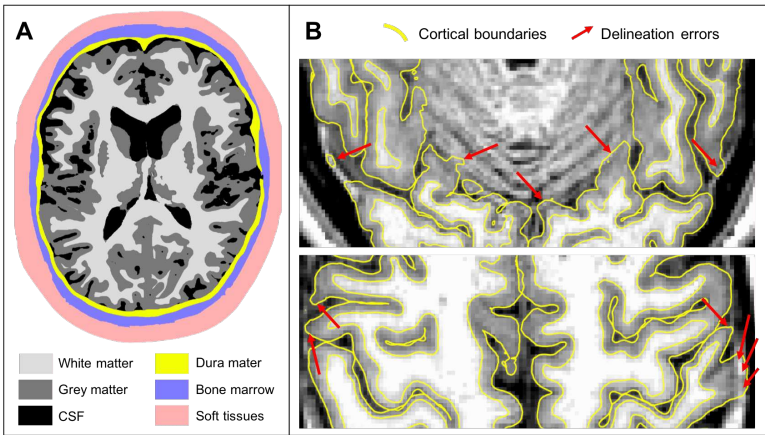

Figure 6.1.1: Human brain tissues and associated segmentation. A) Brain structural representation depicting cortical gray matter (dark gray) and dura (yellow), this figure was adapted from Fiederer et al., (Fiederer et al., 2016). B) Typical cortical surface delineation results over a lower brain transversal slice section (top frame) and upper brain transversal slice section (bottom frame) as obtained by standard Freesurfer processing of the background MPRAGE image with delineated cortical surface boundaries (yellow) overlaid. Delineation errors are highlighted by the red arrows involving poor contrast among GM and adjacent dura structure.

ness compared to the extent of delineation error), making any previous denoising and confound regression ineeffective and leaving persistent biases on the FC estimates at single-subject level.
Moreover, most of delineation errors involve CSF-like contribution which is considered one of the brain tissues mostly affected from physiological noise (i.e. flow effects, motion, pulsation, respiration) motivating the need to manually restrict brain external bounds or manual surface edits.

6.1.1 Refining the cortical surface delineation process

Previous works strived to overcome boundary segmentation errors considering, in addition to T_1-w images, T2-w or T_2^*-w images provided that similar geometric accuracy and intensity homogeneity can be achieved. In general, a T2-w image requires the acquisition of a separate sequence while different T_2^* weightings can be obtained collecting multiple echoes for example by extending a single-echo T_1-w MPRAGE.

The usage of T_2^*-w images was initially proposed by van Der Kouve et

al. (van der Kouwe et al., 2008) where multi-echo data with different T_2^* contrasts were used to refine a surface delineated.
Although interesting for consistent morphometric studies, the approach is currently not widely spread in the FC literature due to the requirement of a dedicated sequence (i.e. a multi-echo MPRAGE) possibly more prone to artefacts, motion and longer scan time although still somewhat limited in poor SNR areas.
These approaches are generally more effective to delineate GM from WM than GM from CSF or meninges when sufficient contrast is available because the structural T_1-w image is typically optimized for best GM to WM contrast assuming a CSF nearly intensity nulled (Wang et al., 2014). Meninges, in turn, are explicitly suppressed or exhibit vanishing signal intensity because of their low T_2^* though possibly MRI-visible, especially regarding the dura.
Cortical delineation errors arising from the usage of these images are only partially explained by limited SNR and CNR, whereas high SNR brain areas (see 6.1.1-B) instead exhibit delineation error more often related to the presence of MR-visible structures not considered during the contrast optimisation because hypothesized to be suppressed (i.e. non MR-visible). Following considerations about sequence design and optimization were performed according to these relaxation parameters observed at 7T.

6.2 A GENERALIZED CORTICAL DELINEATION FRAMEWORK

We propose a framework to cope with previously discussed FC uncertainty, shifting the entire traditional acquisition pipeline toward fast quantitative MRI approaches aimed at minimizing the need for manual surface editing.
The proposed framework relies on two concepts: synthetic MRI (*synMRI*) and quantitative MRI (*qMRI*) by means of Magnetic Resonance Fingerprint (*MRF*). The fascinating element is that these concepts to some extent overlap and will eventually merge current multiple-contrast images into a single flexible and general-purpose sequence (Gulani et al., 2004).

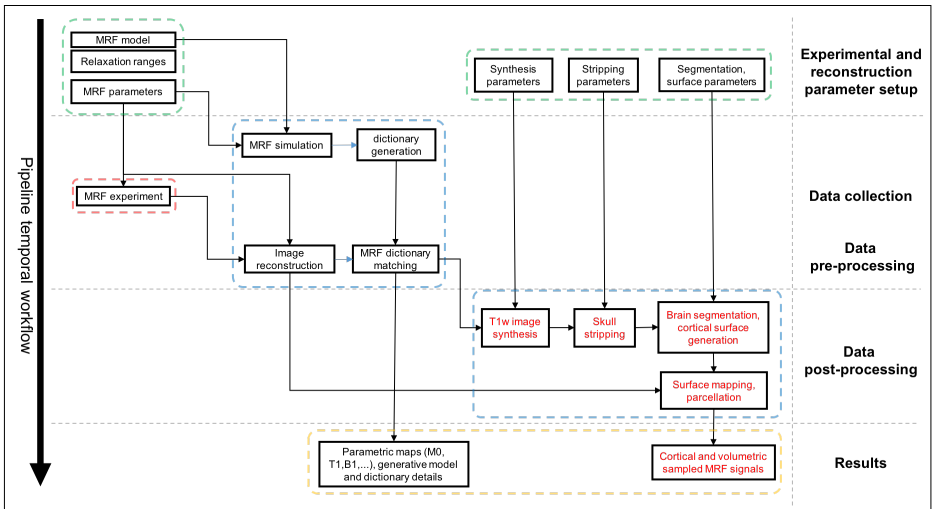

Figure 6.2.1: Implemented brain cortical delineation scheme. From top to bottom is represented the temporal processing domain from the MRF modelling and sequence definition (top-left, green dashed) along with the parameterization required by synMRI, brain skull-strip and segmentation (top-right, green dashed). The following step use these parameterizations to collect actual MRF data from the imaged sample (middle box, red dashed), building the MRF dictionary that will be used for the subsequent dictionary matching process (middle box, blue dashed) in order to estimate the relaxation parameters (i.e. T_1, T_2^*, etc). Relaxation maps are then fed to the synMRI tool (middle box, blue dashed) whereas generated images are skull stripped and segmented to provide cortical surface delineation over which the parametric maps (relaxation) are finally sampled (bottom right, yellow dashed square).

6.2.1 Synthetic MRI principle

Synthetic MRI consist in the generation of images with contrast based on the local relaxation parameters of the imaged object (Bobman et al., 1985).

It is aimed to provide completely arbitrary contrasts (tuneable off-line within a context correspondent to machine learning of different contrasts) (Bobman et al., 1985) or infer quantitative parameters from others (Callaghan et al., 2016) proving increased robustness to artefacts and motion effects

along with spatially homogeneous contrast helpful for improved segmentation accuracy.
The synthesis process involve a prediction model for spin evolution (e.g. Block equations, EPG models, etc) and a prescibed magnetisation manipulation to be simulated (e.g. sequence diagrams, T_E, T_R and FA). The collection of different contrast is no longer necessary with a possibly significant save of scan time in clinical setting (Blystad et al., 2012) additionally providing control on the artefact content or eventually obtain non-measured contrasts as in (Callaghan et al., 2016) for magnetisation transfer.

6.2.2 Magnetic resonance fingerprint for qMRI

A wide range of experimental methods are currently available for quantitative MRI, different by estimation accuracy, resolution and scan time. In general they can also be scan time efficient since they provide one or few parameters at a time while also simplifying the model description.
An opposite approach would instead make the experimental process sensitive to all the relevant relaxation parameters (Schmitt et al., 2004), disentangling their contribution during a post-processing. This perspective underlies the idea of MRF (Ma et al., 2013).

In MRF the experimental stage consist in making the actual spin evolution sensitive to many different relaxation parameters at once, performing the actual quantification step by matching the measured dynamics to a predefined set of dynamics (dictionary) generated by a proper model. The first critical ingredient of MRF is indeed the dictionary, consisting of a range of possible spin dynamics to be measured under the prescibed pulse sequence. However, MRF is practically feasible because it allows extremely high image acceleration factors, resolving the resulting aliases by means of adequate pattern matching provided that these aliases are temporally incoherent.
Since MRF makes no assumptions regarding the sequence in use (needs

only to be feasible its simulation) different excitation schemes like FLASH, FISP or True FISP modules can be combined within a single continuous acquisition to emphasize the various relaxation contributions and eventually balance spatial resolution and measurement precision or including water diffusion (Rieger et al., 2018) or perfusion (ESR, 2015).

6.2.2.1 THE MRF PRINCIPLE

As previously described, MRF consists in a comprehensive prediction of the observed spin dynamics under an arbitrary set of RF and gradient pulses hereby referred as fingerprint.
If the pulse sequence is known, then the fingerprint expected from a voxel characterized by a fixed set of relaxation features could be determined. Simulating the response for a range of voxel mixtures would therefore provide a basis to be inverted in order to gather informations about the sample according to the most similar fingerprint measured.
The flexibility of pulse sequence and problem inversion is essential to both independently promote differential spin dynamics while facilitating efficient solutions of the inverse problem.

In general the MRF approach requires three ingredients:

- A model for the spin dynamics during an arbitrary sequence;
- A suitable sequence to be applied;
- An inverse problem solver.

As previously discussed (see Chapter 2), the EPG approach offers a computationally feasible alternative to Bloch equations valid in a wide variety of experimental conditions and was one of the key tools that enabled MRF feasibility since its recent introduction (Ma et al., 2013).

EPG made also possible to simulate a wide range of fingerprints (discretized range of T_1, T2, etc.) with convenient computational burder overcoming the hurdles of analitical Bloch solutions, currently unavailable

with practical computational times. Keeping a focus on the ease of interpretation, each generated fingerprint (conveniently inserted within a dictionary) is associated to a unique set of relaxation parameters.

It is then fundamentally the objective of the pulse sequence to make such fingerprints sufficiently different among them to actually provide a non-ambiguous problem inversion, in this case consisting in the selection of the best-matching dictionary entry (pattern matching for example based on inner product).

Interestingly, this dictionary can be built considering every variable that can actually provide a measurable effect on the fingerprints. Therefore, recent studies added important features not related to the relaxation such as the perfusion or diffusion as well as system parameters such as B_1^+ (Buonincontri and Sawiak, 2016) making the actual quantification of every other parameter more robust to the hardware uncertainties typically affecting relaxation measurements.

This robustness enabled the use of more spatially inhomogeneous pulses (alleviates the need for accurate RF pulse design to guarantee homogeneous B_1^+ enabling faster excitations) while possibly discarding the effects of B_0 inhomogeneities (Cloos et al., 2016) using the hardware configurations as further probes for such inaccuracies.

The problem is therefore conveniently shifted from the sequence, RF and hardware design to signal modelling with the potential issue of increasingly demanding computational burden, recently alleviated by means of numerical decomposition and compression techniques (Lattanzi et al., 2018; McGivney et al., 2014).

In principle, fingerprint consists a separate set of k-space to be filled. However, at high resolutions this requires unfeasible scan times even applying traditional parallel imaging methods. A peculiar aspect of MRF is the availability of a model that describes temporal dynamics, therefore signal variabilities uncorrelated to the dynamic of interest (e.g. incoher-

ent aliasing artefacts (Feng et al., 2014)) are intrinsically discarded by the very nature of the dictionary matching.
Assuming smoothly varying spin dynamics, the k-space under-sampling strategy can be pushed as much as needed provided that it promotes temporally incoherent aliasing artefacts (Ma et al., 2013) solvable during the pattern matching process (i.e. uncorrelated alias dynamic would not bias the mapping results).
This led to dramatic reductions of the actual scan time achieved for example using variable density spiral trajectories (Ma et al., 2013) or radial spokes (Cloos et al., 2016), possibly stacked for 3D imaging.

6.3 MRF IMPLEMENTATION FOR RELAXATION MAPPING

We built upon the idea of using T_2^* to overcome the limited T_1 contrast between meninges and pial surface while measuring B_1^+ field distribution to obtain robust relaxation measures supplied to synMRI, in turn optimized for cortical delineation accuracy with a flexible approach built upon inherently co-registered relaxation maps.

6.3.1 MATERIALS AND METHODS

MRF sequence implementation, testing and safety assurance steps were performed on custom phantoms composed by different compartments (cylindrical test tubes) exhibiting various combinations of T_1/T_2^* relaxation encompassing the range of human brain tissues within a salted water container.
Estimation accuracy of obtained relaxation parameters was tested on phantom compared to gold standard relaxation measures: single slice (2D) IR-GRE measurements with variable T_I = 30-6000 ms (T_E/T_R = 3/7500 ms, FA = 30 deg) unevenly spaced over the T_I span to provide 8 measures at fixed spatial resolution for T_1 estimation; single slice (2D) SR-GRE measurements with variable T_E = 3-50 ms (T_R = 2000 ms, FA = 10

deg) unevenly spaced over the T_E span to provide 8 samples for T_2^* measurement.
The implemented MRF sequence, referred as MRF-vTE in the following ($1mm^3$ isotropic resolution, peak FA = 20 deg) was preliminary tested in 2 healthy volunteers (males, 25 and 28 yrs) on an investigational whole-body 7T (MAGNETOM 7T, Siemens Healthcare, Erlangen, Germany) using a 1-TX 32-RX head coil (Nova Medical, Wilmington, MA, USA) in circularly polarized RF configuration (CP mode).
Results were compared with structural T_1-w MPRAGE (Wang et al., 2014) images. Written informed consent was obtained from each study participant.

6.3.1.1 MRF Sequence design

A 3D MRF sequence previously used for T_1 mapping by Fojimoto et al. (Koji et al., 2017), derived from (Cloos et al., 2016), to measure T_2^* in addition to T_1 and B_1^+ using a single B_1^+ transmit configuration (single channel transmission).
Each MRF sequence application would result in the volumetric estimation of the apparent longitudinal magnetisation (M_0), T_1, T_2^* and B_1^+ (FA) maps.
As illustrated in 6.3.1-A, the MRF-vTE sequence (3D Plug-and-Play MRF with variable T_E) implements a 3D stack-of-stars readout (Block et al., 2014) by repeating, for each 2-spoke star (defined on the $k_x - k_y$ plane with k_z as cartesian partitioning dimension), an adiabatic non-selective Frequency Offset Corrected Inversion (FOCI) RF pulse (with FA of 720 deg (Ordidge et al., 1996)) followed by 750 or 1000 FLASH segments considering a different RF pulse relative amplitude, scaling down the maximal prescribed FA with a half-sinusoid pattern as depicted in 6.3.1-B.

This pattern provided progressively higher RF coil driving voltages along the three consecutive sectors in the 750 segments case while alternate low/high driving voltage in the 1000 segments case.

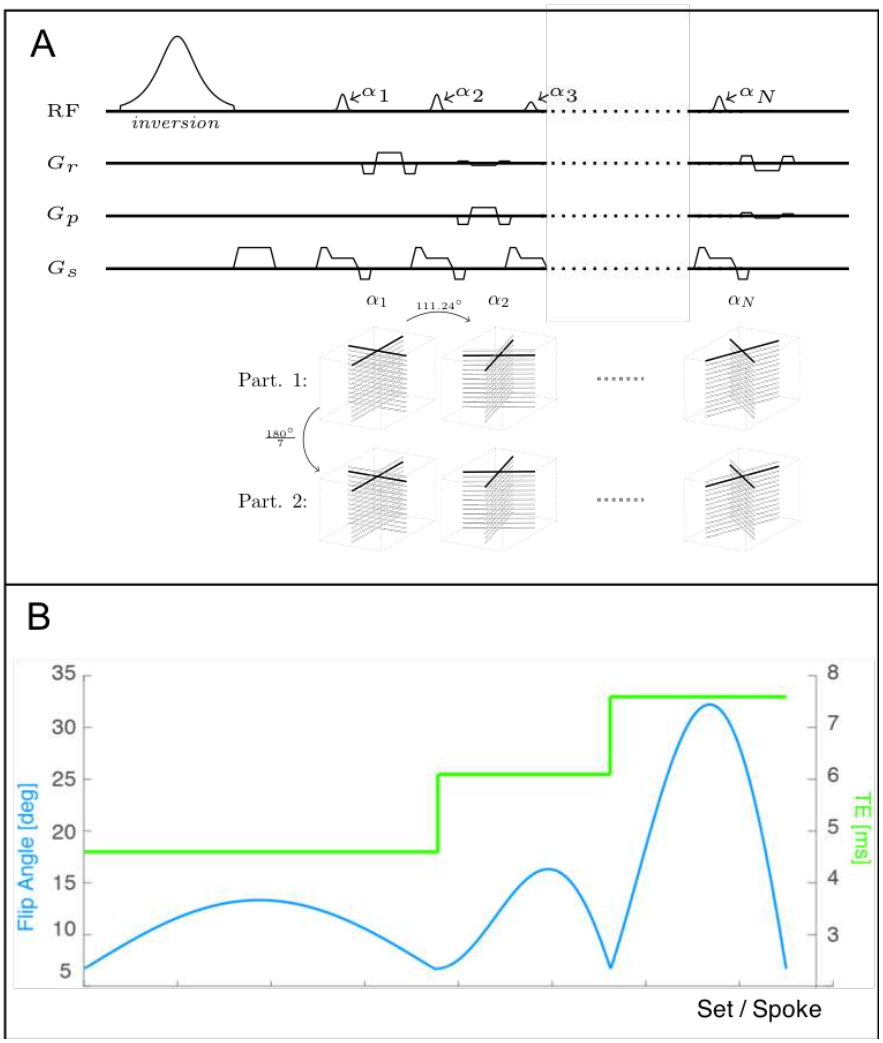

Figure 6.3.1: Overview of the MRF-vTE sequence. A) Pulse sequence diagram of the 3D-MRF with golden angle increase of spoke angles along the fingerprint while 180 deg fractional increment along partitions (Part.). The typical scheme of prescribed T_E (green trace) and FAs (blue trace) over 750 time points (at least 200 per each sector) are shown in (B) dividing the fingerprint in three sectors. T_R trace was omitted as identical to the T_E except for a fixed positive offset typically of 5 ms with the prescribed imaging settings.

Both 750 and 1000 shot patterns considered a traditional RF phase-cycling scheme based on a quadratic RF phase increment with increments defined by a base angle of 117 deg. The kernel sequence overall consisted in a RF-spoiled GRE (FLASH) instead of previously used FISP segments used for T_2 measurement while providing enhanced motion robustness (Yu and Cloos, 2017). K-space stars collected along consecutive segments are rotated by with a golden angle (117.3 deg) increase schedule and FA reported in 6.3.1-B.

In-plane stars were composed by spokes relatively angled to homogeneously fill the 360 deg range. For example 2-spoke stars are composed by spokes angled by 90 degrees. All kz partitions corresponding to a single radial spoke were collected sequentially with a linear ordering scheme (i.e. equi-distributed steps from k_z = -$k_{z,max}$/2 to k_z=+$k_{z,max}$/2, where $k_{z,max}$ is defined by the inverse of FOV_z and number of partitions) before collecting another radial spoke angle. To measure the T_2^*, the segments were divided in 3 or 4 sections respectively for 750 or 1000 shots with increasing T_E (and T_R keeping fixed T_R-T_E offset) at each section as depicted in 6.3.1-B.

In-plane logical gradients (G_x, G_y employed for radial readout) were first-moment balanced as well as out-of-plane (G_z) partition selection gradient with only unbalanced gradient the spoiler. The T_E delay introduced at each section was empirically optimized in order to provide adequate T_2^* sensitivity for distinguish the T_2^* of dura structure (few ms) to the T_2^* of GM. Baseline T_E/T_R were set at the minimally supported values, respectively of 2.5 ms for T_E and 7.5 ms for T_R within the prescribed imaging parameters and available hardware. The sequence made use of sinc-shaped RF excitation pulses (slab selective) with fixed duration, delay period after the initial inversion RF pulse of 20 x T_R [ms] and between sections with different T_E (10 x T_R [ms]).

The delay among consecutive inversion RF pulses was set to 2000 ms to allow a sufficient longitudinal magnetisation recovery.
To summarize, the sequence used for MRF-vTE phantom acquisitions was defined as: T_E/T_R = 2.5/7.5ms, RF time-bandwidth ratio 3, RF pulse

duration 2ms, 160 160 x 8 matrix, 1.0 1.0 x 5.0 mm resolution, 2x slice oversampling to avoid spurious aliasing along the spoke direction and overall under-sampling factor of approx. 10 (view sharing window merges 12 consecutive 2-spoke stars per each reconstructed volume) for an approximate scan time of 4min 10s using 750 shots.

The MRF-vTE sequence used for human in-vivo acquisitions was consistently similar while differing only for: T_E/T_R = 3.0/8.0ms, 240 240 x 8 matrix (overall under-sampling factor of approx. 16), 1.0 1.0 x 1.0 mm resolution and an approximate scan time of 5 min 25s with 1000 shots.
While consistently similar performances were offered by the usage of 750 and 1000 shots, we choose to employ 1000 shots for in-vivo data and 750 for phantom to provide a more comparable behaviour of the dictionaries in poor B_1^+ areas preferring to increase the train length rather than the nominal FA to provide similar estimation performances.

6.3.1.2 MRF Reconstruction

Single volumes of MRF data were reconstructed in Matlab (The Mathworks Inc., Natick, USA) using an in-house developed software implementing a 1D-FFT along the partition direction (k_z, i.e. across collinear spokes of stacked stars) followed by a 2D non-uniform fast Fourier transforms (2D-NUFFT) over an appropriate trajectory sampling grid to reconstruct in-plane ($k_x - k_y$) collected stars. In-plane ($k_x - k_y$) stars were composed by spokes collected along 12 consecutive RF shots implementing a view sharing scheme (with window size and sliding window step of 12 shots (Cloos et al., 2016)) aimed at reducing the aliasing artefacts during reconstruction stage, while preserving the parametric sensitivity range of relaxation.

Merging and reconstructing such stacked stars effectively reduced the number of MRF time points to reconstruct from 750/1000 to 62/83.
The MRF dictionary was subsampled to match the reconstruction size by averaging 12 consecutive generated time points for each dynamic (not averaging samples from sectors with different T_E).

A separate set of coil sensitivity profiles were derived in each of the three sections and applied for coil combine (Walsh et al., 2000) the pertaining segments and remove baseline phase-offsets depending on TE differences in order to discard B0 effects resulting in phase differences among consecutive sectors (Lattanzi et al., 2018).

6.3.1.3 MRF DICTIONARY

MRF signals for a range of T_1 (50-3000 ms, 5% increment), T_2^* (5-100 ms, 5% increment), B_1^+ (1-30, 1 increment) were simulated using an in-house implementation written in Matlab and C++ simulating the sequence with an EPG approach (see Chapter 2), considering $M_0 = 1$ (thus estimated from the match scaling to the measured data) while other parameters were as in the MRF sequence. Since the RF excitation is performed over a thick slab, we assumed the excitation profile to provide sufficiently homogeneous RF excitation within the slab centre, therefore not requiring to explicitly account for the across-slice inhomogeneity of the excited magnetisation.
This condition was further enforced in this study by prescribing in all imaging acquisitions a slice-oversampling factor of 2.

MRF measured signals of each voxel were matched to the best dictionary entry by means of maximum normalized inner product (i.e. linear correlation) of the MRF signal and all dictionary entries. The part of MRF signal right after the initial inversion pulse (10 shots after the inversion RF pulse) and after a T_E discontinuity (5 shots after the variation of T_E) were discarded to avoid phase instability unresolved during reconstruction which could bias the dictionary matching process. Note that, even if the FA schedule was fixed, the dictionary entries need to be sufficiently weighted by T_2^*. Therefore, adequate T_E schedules need to be first of all simulated and empirically tested to guarantee that dictionary entries generated with different T_2^*, are actually distinguishable by the matching

operator under realistic noise conditions.

This process strive to tune the T_E schedule in order to emphasize T_2^* contribution in the range of 5 to 30 ms, respectively making the dictionary sensitive to T_2^* possibly related to dura structures as well as different brain tissues. Note that making the dictionary actually able to distinguish brain tissues would require much longer T_E making the scan time unpractical. Instead, using T_E up to 20 - 25 ms, the sensitivity should be sufficient to distinguish T_2^* values up to 30/40 ms (depending on noise conditions). The implemented scheme from the MRF acquisition to the relaxation reconstruction was summarized in 6.3.2.

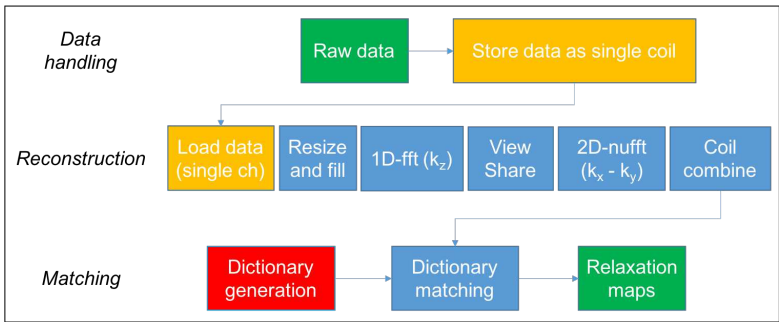

Figure 6.3.2: Flowchart of data processing for MRF. Acquired raw MRF data (k-space performed measurements) is decompressed and reshaped for more efficient handling in single channels (top). Single-channel data is loaded and reshaped in Matlab for reconstruction, first performed to resolve the frequency along partitions (kz), merging consecutive spokes (view sharing) and performing a non-uniform 2D-fft reconstruction (2D-nufft). Data reconstructed from single channels (coils) is then combined according to the sector-defined coil sensitivity profile (determined using the same reconstruction pipeline by merging all sector shots and normalizing the relative amplitude). Reconstructed MRF dynamics are then matched (Dictionary matching) to the dictionary entry finally generated to provide the actual 3D relaxation maps.

Data reconstruction, dictionary generation and matching were performed using a quad-core laptop computer running at 2.3GHz equipped with 8 GB memory. The approximate dictionary generation time was implemented in C++ and required in most cases less than30 minutes for the computation and, under prescribed dimensionality, less than 1 GB of disk storage (per dictionary, stored uncompressed).

Before the dictionary matching, the actual dictionary size was further reduced by a factor of 24 obtained combining a factor 2 by discarding the fictitious imaginary component of generated entries and an approximate factor of 12 given by the view sharing which bundled together 12 consecutive time points (with same compression scheme implemented for the measured fingerprints).
MRF image reconstruction of collected and compressed (view shared) data was implemented in Matlab (without parallel computing implementation due to memory constraints) and required typically less than10 minutes of computation time per slice while the dictionary matching (implemented in Matlab as well) less than 5 minutes per slice to reconstruct the final relaxation maps.

6.3.1.4 IMAGE PROCESSING

T_1 maps from MRF were subsequently used to create a synthetic MPRAGE (Wang et al., 2014) ($1mm^3$ resolution, 160 partitions, T_{I1}/T_D = 1000/3700 ms, FA=6).
T_1-w images were skull stripped (bet, FSL, v5.09 (Smith et al., 2004)), 3-class segmented (fast, FSL v5.09 (Smith et al., 2004)) and parcelled in 108 regions of interest (ROI) with Multi-Atlas Label Fusion (MALF) method (Hongzhi Wang et al., 2013) and MICCAI 2012 reference dataset.

Pial and GM/WM cortical surfaces were outlined (Freesurfer v. 5.3, https://surfer.nmr.mgh.harvard.edu/fswiki; Caret v. 5, Connectome Workbench v. 2.3) also as support for parametric maps representation. T_2^* map was separately used to verify the efficacy of brain mask refinements prior to post-processing. Consistency of T_1 and T_2^* values and maps on clear anatomical structures was verified and obtained segmentation locally inspected for delineation errors. Sensitivity to dura structure, signal dropout (susceptibility inhomogeneity) as well as intensity inhomogeneity and motion effects were evaluated.

6.3.1.5 IMPLEMENTED FRAMEWORK

Once the MRF sequence and an appropriate dictionary have been generated, from the data handling perspective the scheme reported in 6.2.1 was step-by-step implemented as:

- MRF data collection, dictionary matching for parametric map generation
- Formatting and conversion of parametric maps (T_1, T_2^*, M_0 , B_1^+) to standard format (NIfTI)
- Generate skull-stripping mask from T_1 and M_0 (bet, FSL), then segment macro brain tissues (fast, FSL)
- Refinement step of obtained masks
- Generate the synthetic MPRAGE image
- Cortical segmentation and reconstruction with Freesurfer (feeding the refined brain mask)
- Parametric surface mapping and parcellation

6.3.1.6 LITERATURE DATA

To investigate the relaxation features at 7T of the dura structure (section 4.1) we referred to literature images from Haast et al., (Haast et al., 2016) including data collected with a multi-echo 3D GRE with T_E range from 2.53 to 20.35 ms (see (Haast et al., 2016) for further details) and data from Forstmann et al., (Forstmann et al., 2014) comprising an MP2RAGE image (T_E/T_R = 3.71/5000 ms; T_{I1}/T_{I2} = 900/2750 ms; FA = 5/3 deg, 0.6 mm isotropic resolution) used for dura detection and a multi-echo 3D FLASH with T_E ranging from 11.22 to 29.57 ms (0.5 mm iso voxel size).

The T_1 and T_2 relaxations in the brain were also observed from unpublished data collected at 7T making use of the sequence implementation already used in Yu et al., (Yu and Cloos, 2017) and consisting in a radial

2D-FISP-MRF sequence (0.6x0.6x5 mm). Effectiveness of skull-stripping (section 4.2) based on T_1-w or quantitative relaxation was instead investigated over 7T human brain data, available from a previous study pilot (healthy male subject, 33 yrs) scanned using the standard and validated 3D-PNP-MRF sequence.

6.4 Preliminary results

6.4.1 Relaxation features from literature data

Observing the multi-echo 3D GRE images made available by Haast et al., (Haast et al., 2016), the dura structure appears visible at T_E = 2.5 ms, starts to decay at T_E = 7.0 ms while is non-visible at TE = 12.5 ms, suggesting its typical apparent transversal relaxation (T_2^*) to be less than 12.5 ms and higher than 2.5 ms.
Similar data published by Forstmann et al., (Forstmann et al., 2014), suggested by visual inspection that dura structure is consistently suppressed at T_E = 11.2 ms while completely nulled considering T_E = 20.4 ms or higher, again suggesting typical T_2^* of less than the lower TE but not with same rate across the brain.

From both datasets, the T_1 of dura is typically observed from 900 to 1000 ms, while CSF of 3300 ms or higher and the bone marrow of 100 to 200 ms. T_2 was instead observed in dura between 15 and 25 ms, the bone marrow typically having $T_2 < 10ms$ and CSF higher than 150 ms (observing the unpublished 2D-FISP-MRF data). Dura thickness across the brain is approximately 1 mm thick, entailing strong partial volume effects at typical resolutions.

6.4.2 Considerations from a reference MRF dataset

Human brain data, using the standard 3D-PNP-MRF sequence, was analyzed to compare the performances of traditional approach to the proposed framework for cortical surface delineation evaluating the feasibility of the latter in reducing pial delineation artefacts. This data consists

only in T_1 relaxation, B_1^+ and M_0 without T_2^* estimate. In this case, the proposed framework basically differs from the traditional delineation directly from a T_1-w MPRAGE regarding the data acquisition and synthesis of the T_1-w image (i.e. without any T_2^* refinements). This analysis will guide the selection of the most effective skull-stripping scheme based on all the estimated parameters and also eventually suggest whether some improvements are already offered using a clean T_1 contrast image alone, unaffected from B_1^+ or motion effects, expected to be particularly disturbing at 7T.

The standard 3D-PNP-MRF sequence provides two measures suitable for skull-stripping: M_0 and T_1 images and the synthetic MPRAGE. Since the T_1-w image is simulated, we can optimize its synthesis to improve skull-stripping efficacy. However, optimizing the T_1-w image contrast based on skull-stripping results would heavily depend on the algorithm implementation per se. A more flexible solution can instead be based on quantitative parameters to be directly segmented, thus optimizing the skull-strip parameters only once. In this implementation we consider for simplicity only skull-stripping methods based on watershed segmentation or intensity-based, leaving the application of registration-based methods for future application.

To note is that registration-based approaches would instead benefit from the usage of T_1-w images instead of relaxation parameters because: 1 same contrast as the reference images that should be registered to; 2 spatially homogeneous contrast offered by synthetic MRI.

A typical example of obtained parametric maps and synthesized T_1-w image (reconstructed with 1x1x2 mm voxel-size) is shown in 6.4.1. Accurate brain anatomy is depicted along different views, 6.4.1-A reporting adequate and homogeneous contrast among both GM/WM and GM/CSF. Estimated T_1 values of GM in frontal, temporal, parietal, occipital respectively were (ROI mean $\pm$ standard deviation): 1410 ± 85 [ms], 1400 ± 110 [ms], 1390 ± 80 [ms], 1420 ± 80 [ms] whereas in anterior or posterior WM were: 800 ± 140 [ms] and 780 ± 100 [ms]. More variable local

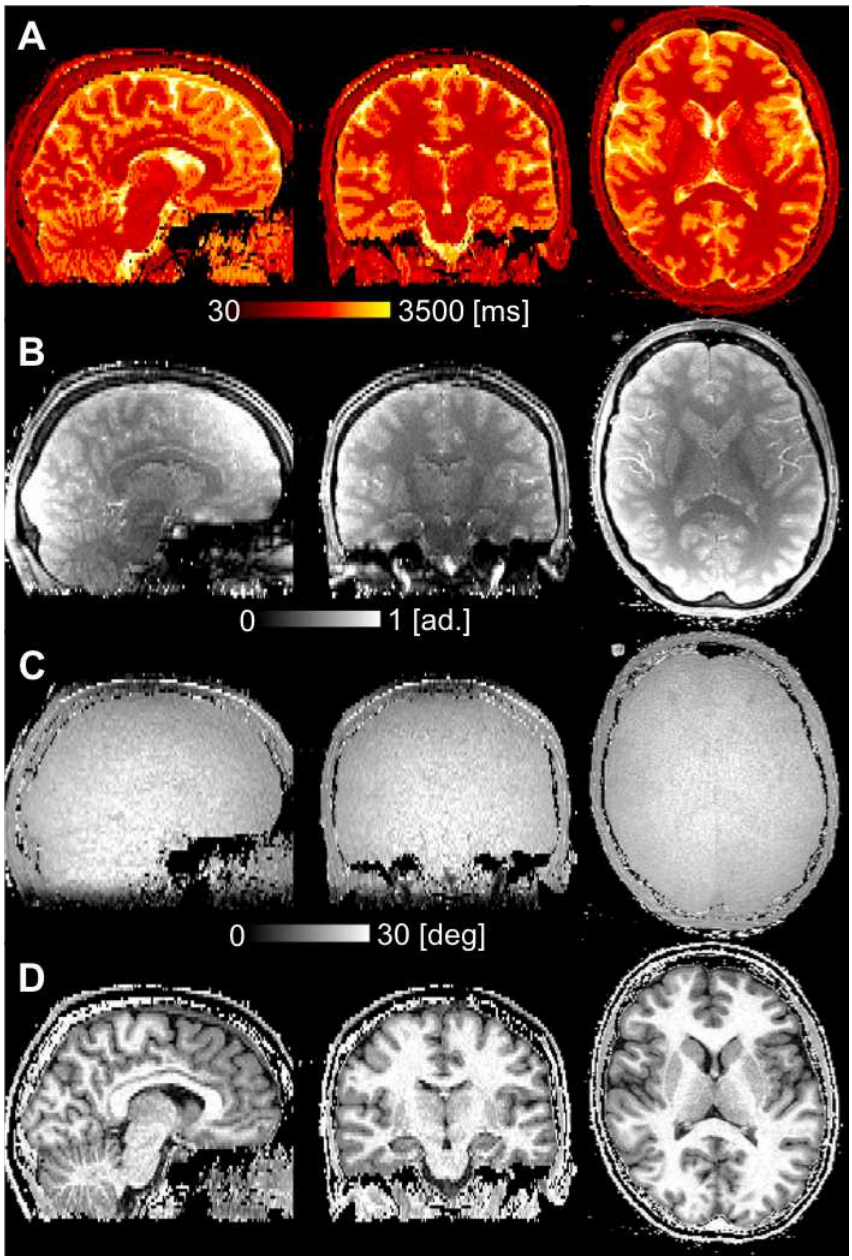

Figure 6.4.1: MRF mapping and synMPR image. Relaxation representation of a healthy human brain for T_1 (A), M_0 (B), B_1^+ (C) and synthesized MPRAGE (D) over three representative brain views (from left to right sagittal, coronal, transversal) acquired with the original 3D-PNP-MRF with stack-of-stars readout over 750 time points. Whole-brain maps were obtained with spatial resolution of 1x1x2 mm3.

estimate instead interested very high T_1 values of the CSF (ventricular) : 3200 ± 550 [ms] or small meningeal layers with typical thickness less than 3 voxels wide (manually delineated): 950 ± 400 [ms]. CSF locations exhibiting a dynamic not correctly described during the dictionary generation (i.e. having $T_1 > 3500ms$) instead are eventually shown with null T_1 estimate.

Around the GM matter the black areas reporting T_1 values under the display threshold represent the relaxation of bone marrow or scalp fat tissues, typically much shorter than other tissues ($T_1 < 500ms$), eventually non MR-visible. Obtained T_1 relaxation values were overall accurate except for areas exhibiting very low B_1^+ also possibly associated to the incomplete fulfillment of the adiabatic condition required by the initial RF inversion pulse that results in an inconstant initial amplitude of the measured fingerprint.

Even if the GM/WM contrast is confounded by the observed effects the actual contrast GM/CSF is suitable, adequately distinguishing GM from pial structures which are actually suppressed corresponding to a rim of voxels with nearly negligible M_0 amplitude either corresponding to dictionary entries scaled by very small magnitude amplitude (i.e. M_0) or very fast decaying spin dynamics not adequately modelled (thus degenerated estimates).

The FA profile reported in 6.4.1-C, is consistent with expected pattern of excitation provided by the two-channel coil used with circular-polarization mode with higher FA reached in the FOV center, slowly decaying without tissue-specific contrast from the maximally achieved FA at the brain center ($FA = 25 \pm 2[deg]$) to the periphery ($FA = 17 \pm 4[deg]$) that covers GM.

Figure 6.4.1-D shows the synthetic MPRAGE obtained from the T_1 relaxation. Obtained T_1-w image show high and homogeneous GM/WM contrast as well as GM/CSF contrast. However, meningeal structures are visually conspicuous exhibiting intensity similar or lower than GM, typical distance in this subject ranged from 3 voxels (i.e. 3 mm) to 1 voxel (i.e. 1 mm or less in case of partial volume effects) measuring the distance

from GM gyri to the nearest visible dura surface.

However, skull-stripping mask derived from the synthetic MPRAGE suffers from an excessive frontal erosion which possibly erode the GM while posteriorly the mask is broader encompassing both some pial areas with CSF-like intensity and part of the dura. Instead, the mask obtained from the T_1 map was consistently dilated (generally larger than its counterpart) encompassing all over the brain GM external surface CSF-like structures up to the meninges, possibly suffer less from parametric inhomogeneity. This suggest that with an adequate skull-stripping algorithm calibration, the T_1 could provide more consistent and homogeneous masking performance respect to standard MPRAGE.

In Figure 6.4.2 the frontal areas and overall homogeneity has been much improved by means of more effective B_1^+ shimming, recovering most of the signal dropout but still observing some frontal and temporal anatomical blurring in these locations exhibiting unclear GM/WM boundaries in the T_1 map (left column) and derived synthetic MPRAGE (middle column).

Even if with some caveats, these results suggest the usage of T_1 map for skull-stripping in conditions of adequate B_1^+ homogeneity while omitting M_0-derived information possibly hampered by signal dropout that determine tighter masks that result in GM cortex clipping.

6.4.3 PHANTOM STUDY

6.4.3.1 DICTIONARY T_2^* SENSITIVITY ANALYSIS

We then explored the sensitivity of MRF for T_2^* relaxation to various T_E amplitudes at different time intervals (segment) during the acquisition. All other sequence parameters, except for T_E (and thus T_R), are held constant as defined in methods. Instead, the employed T_E pattern and amplitude along the fingerprint have been varied employing different combinations as depicted in 6.4.3 to demonstrate its effect on the MRF dictionary sensitivity for T_2^*.

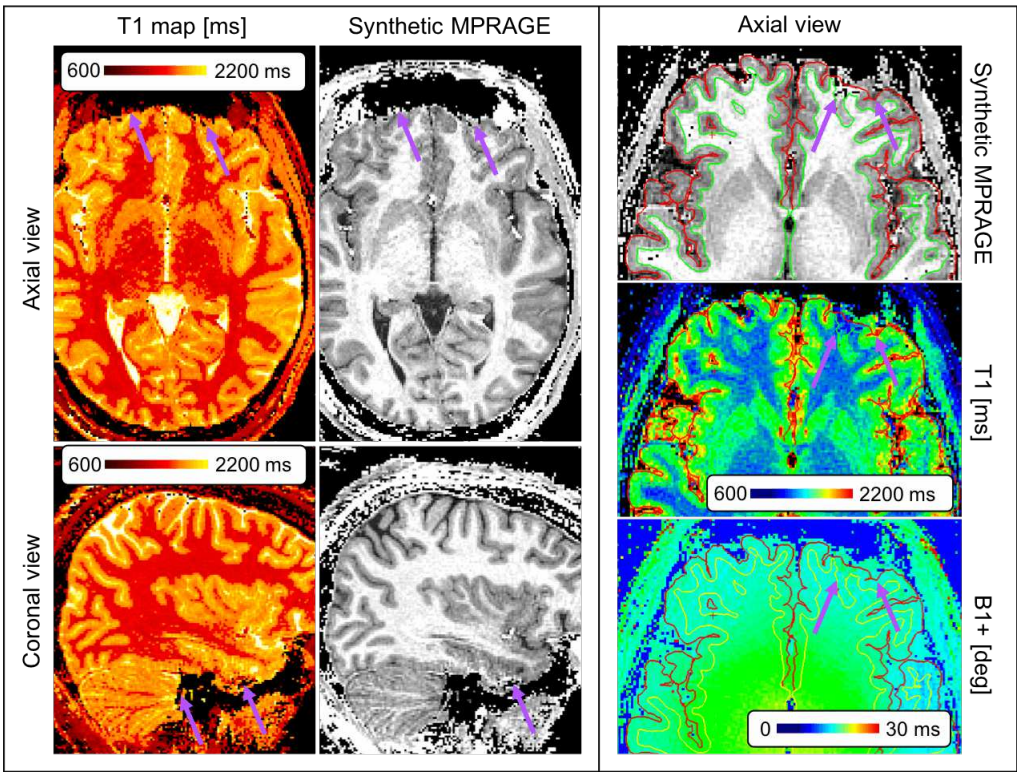

Figure 6.4.2: MRF performance limitation effects on delineated brain cortex. Brain T_1 map (left column) and synthesized MPRAGE (middle column) used for cortical delineation (right column) for an healthy subject over a transversal (top and right) and sagittal view (bottom). Improved positioning and shimming provided more accurate depiction of frontal lobe structures still affected by limited B_1^+ inhomogeneity over the external part of the frontal cortex as well as suffering in temporal lobe (purple arrows). These estimation inaccuracies propagated to the synMPRAGE result in a limited cortical delineation accuracy in these areas particularly affecting pial (red lined) as well as GM/WM interface (yellow lined) reported in the right column in overlay to the relative synMPRAGE, T_1 and B_1^+ maps, non-physiologically regressed from the correct pial location due to poor local B_1^+ amplitude.

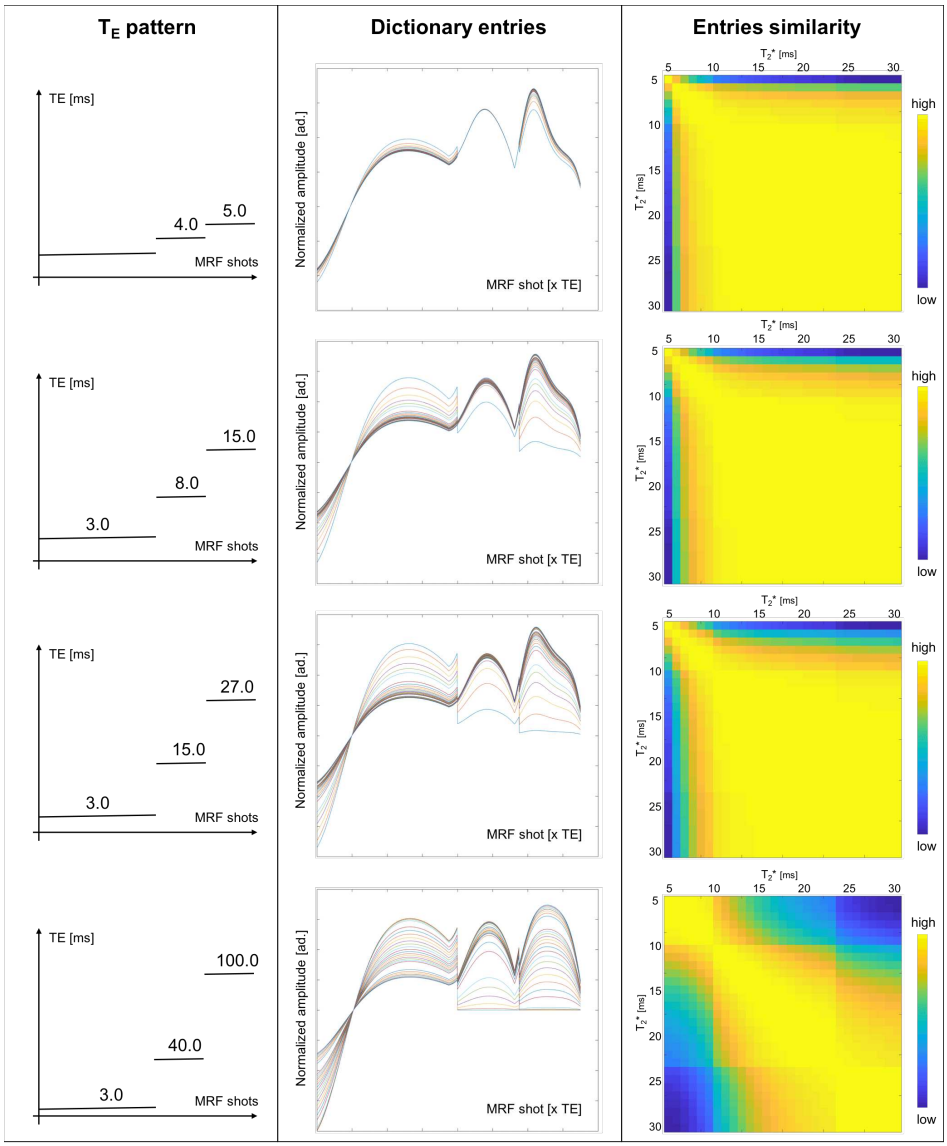

Figure 6.4.3: MRF sensitivity to T_2^* with different T_E patterns. For each prescribed T_E pattern (left column) reported in separate rows a subset of the generated dictionary entries are depicted (middle column) for a single T_1 value (800 ms) and FA (20 deg) and a range of T_2^* values from 5 to 30 ms (step 1 ms), differently colored for better visual clarity. The similarity among all dynamics couples is shown in the right column, depicting the normalized inner product among all dictionary entries for different T_E patterns (by row) to show improvements in T_2^* encoding sensitivity. The extreme case of maximum sensitivity is when the dictionary entries are uncorrelated among them (blue scaled similarity) or at least only locally correlated among similar T_2^* values while first row demonstrate how the dictionary is composed by very similar entries, thus strongly non-diagonal similarity matrix (yellow out of diagonal).

The four representative examples of T_E patterns reported by row in 6.4.3, respectively show in the left column the prescribed T_E pattern, in the central column the normalized dynamic of dictionary entries simulated for the prescribed MRF sequence with the associated T_E pattern (for a single T_1 = 800 ms, T_2^* ranging from 5 to 30 ms with step 1 ms and 33 to 50 ms with step 5 ms, FA peak of 20 deg with the previous half sinusoidal pattern) whereas the right column depicts the normalized inner product among each dictionary entry pairs reported in the central column (entries sorted by increasing T_2^*).

The first row of 6.4.3 depicts a minimal T_E variability (i.e. 1 ms added at each section on top of baseline T_E) across the three sequence sectors (same length for simplicity of 250 RF shots) which results in a very limited span of the simulated dynamics (central column) which are visually consistently similar, thus difficult to distinguish under noisy conditions. This is confirmed in the right column where, under noise-free conditions, the actual similarity displayed by all the entries is very high (corresponding to linear correlations $r > 0.95$), suggesting poor sensitivity for T_2^* (i.e. very similar dynamics regardless of T_2^*) provided by such TE pattern.

An enhanced T_2^* contrast was obtained using higher T_E, consistent with the simulated T_2^* range: as a rule of thumb, to provide significant signal variations the TE should be at least an integer fraction of the aimed T_2^*. For example, aiming at T_2^* of 20 ms, possible TE should be of 10 ms with higher sensitivity offered matching T_E on T_2^* (providing 40% of signal variations according to the single exponential decay model described in Chapter 2). The second to fourth row of Figure 6.4.3 apply this principle to progressively enhance the T_2^* weight of each dynamic, passing for enhancing contrast to possibly saturated contrast at extremely high T_E (40 or 100 ms) which actually enhance contributions of high T_2^* (e.g. 30 ms) while saturating (i.e. nulling) the signal of lower T_2^* (e.g. 5 ms). Coherently the similarity matrices associate to these dynamics reflect the enhancing dictionary sensitivity to the full T_2^* spectrum simulated.

However, the extreme case offered in the fourth row depicts how major T_2^* contrast is overall offered along the simulated T_2^* range but this con-

dition actually provides dynamics difficult to distinguish if having low T_2^* (5 to 12 ms) rather than intermediate (13 to 22 ms) or high (23 to 30 ms) explaining the blocked appearance of the matrix where the contrast is more consistent among blocks rather than being uniformly distributed across all the T_2^* range.
Note that this condition is anyway impractical form the experimental point of view as requires extremely long scan time as compared to shorted acquisitions.
If collecting with T_E/T_R = 3/8 ms requires (((5 x 16 x (8 x 750 + 60 ms)))/1000 + 2)/60 = 8.1 min (16 k_z partitions composed by stars of 5 spokes over 750 RF shots, 60 ms approximate inversion time, 2 sec inter-shot delay) while using a T_E (averaged for calculation simplicity) of 15 ms would require an excessive scan time of (((5 x 16 x (20 x 750 + 60 ms)))/1000 + 2)/60 = 20.1 min.

6.4.3.2 PHANTOM MAPPING RESULTS

Figure 6.4.4 shows the estimated T_1 (left column), T_2^* (middle column) and FA (right column) maps obtained with standard qMRI methods (first row, from the top), the original 3D-PNP-MRF sequence (second row) and the implemented MRF with variable T_E (third to fifth rows). These results were obtained in different scan sessions after repositioning (maps are thus rotated).

Despite some reconstruction artefacts involving the background of the liquid phantom, the geometrical structure of the phantom and inner tubes was well preserved in the MRF maps obtained with the implemented MRF-vTE sequence (third to fifth rows) as compared to the reference maps (first and second rows). Obtained FA maps (right column) were in very high agreement both in terms of spatial pattern and amplitude among the original MRF and proposed MRF-vTE sequence.
Similarly, the T_1 map (middle column) obtained was in remarkable agreement among measurements.

However, T_2^* values showed an apparent deviation from the T_2^* ref-

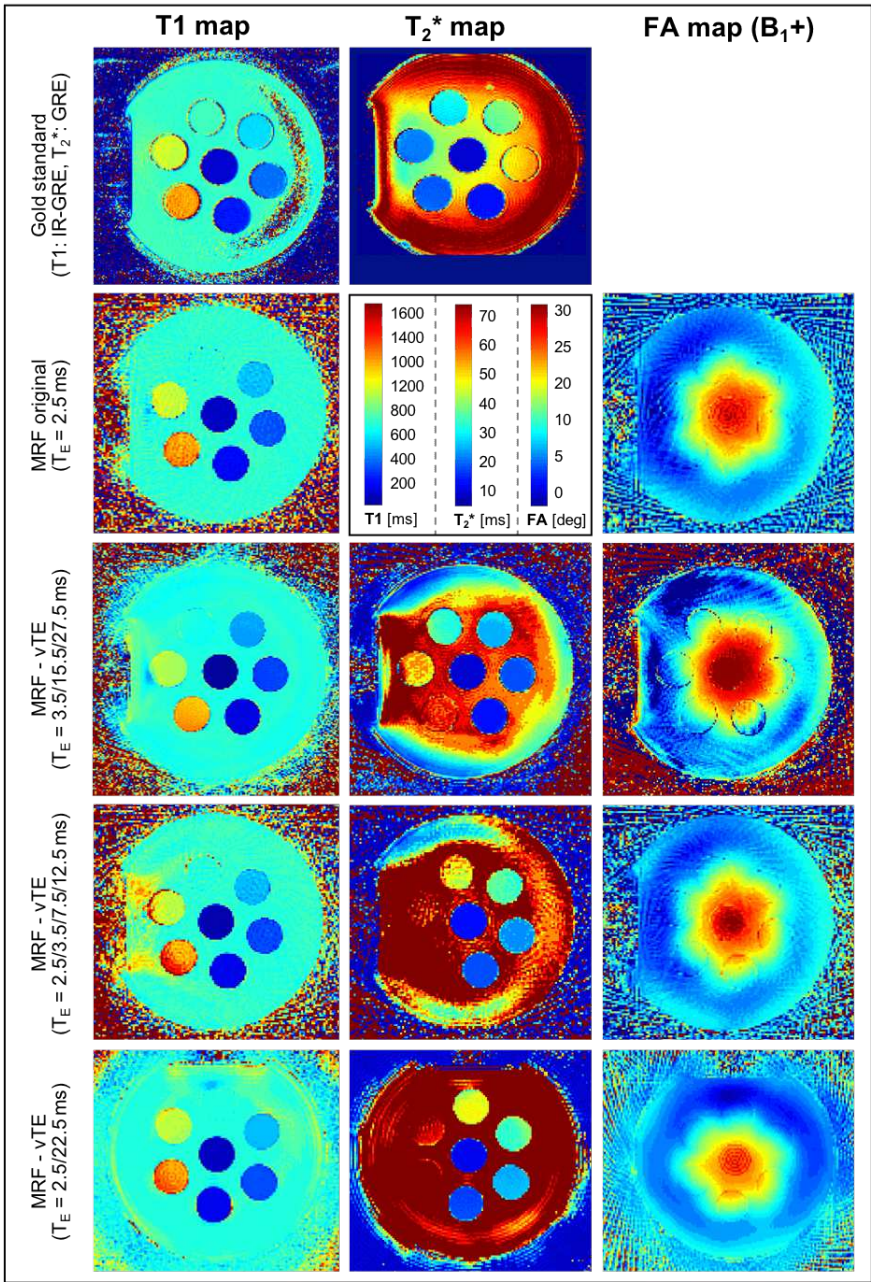

Figure 6.4.4: MRF phantom results at 7T. Phantom comparison of estimated T_1 (left column), T_2^* (middle column) relaxation and B_1^+ (right column) with reference methods (top rows), the original 3D-PNP-MRF (second row from top) and implemented MRF-vTE (third to fifth row) with different T_E patterns to demonstrate their different T_2^* sensitivity. All data was collected using a 1x1x5 mm voxel size and regarding MRF sharing TR=7.5 ms and same FA pattern and amplitude (25 deg).

erence map over high T_2^* values (over 50 ms) and a consistent spatial bias (over the phantom container background) passing from central areas where the B_1^+ actually matches the prescribed FA to external parts of the phantom where the achieved FA can be much lower resulting in the eventual loss of T_2^* sensitivity. The three tested T_E patterns showed progressively lower T_2^* sensitivity from third to fifth row, losing accuracy but also exhibiting lower sensitivity to the B_1^+ inhomogeneity.

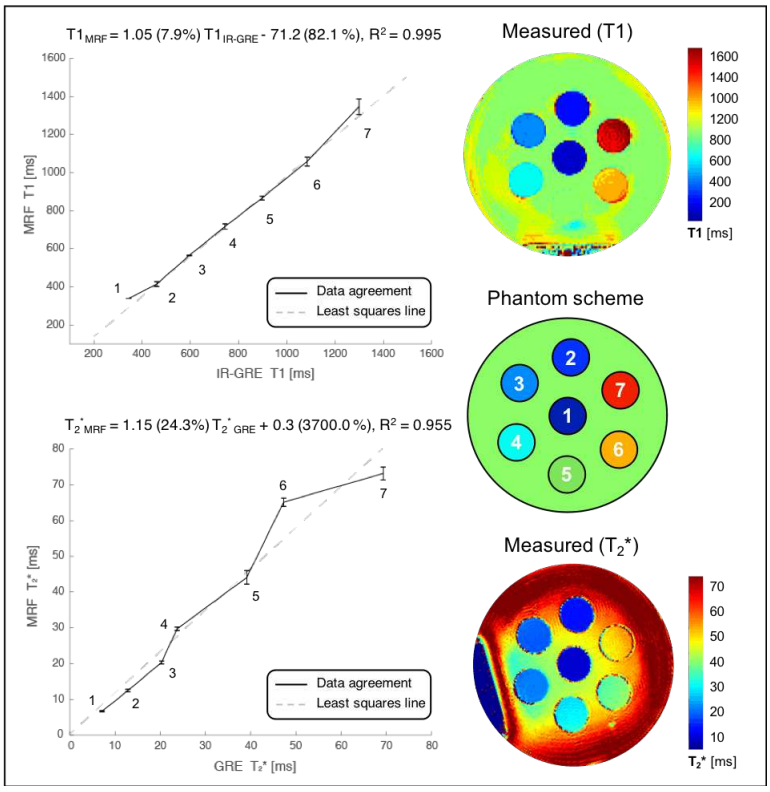

Figure 6.4.5: Phantom validation of MRF-vTE. Phantom validation analysis by means of linear regression between relaxation parameters estimated with reference methods and MRF-vTE (T_1on top, T_2^* in the bottom) expressing the linear agreement within the test tubes (numbered and schematized laterally).

To quantify the T_1 and T_2^* agreement, we performed a linear regression analysis (Figure 6.4.5) over corresponding ROIs, manually delineated encompassing the phantom inner tubes. A very high linear agreement ($R^2 > 0.99$) was obtained in terms of T_1 values (top-left of Figure

6.4.5) with minor T_1 underestimation (regression slope = 1.05) with MRF-vTE as compared to the T_1 estimated with IR-GRE. Deviations observed in the 400 to 1200 ms T_1 range peaked up to -8%. A similarly high linear agreement ($R^2 > 0.95$) was obtained in terms of T_2^* values (bottom-left scatter plot, Figure 6.4.5) with modest T_2^* overestimation for high T_2^* values ($T_2^* > 25ms$) and remarkable agreement over the lower T_2^* range ($T_2^* < 25ms$). The observed T_2^* deviation can be explained by the a progressive loss of dictionary encoding sensitivity, observed using MRF-vTE as compared to the reference with relative error increasing from +20% at 30 ms up to +30% at 50 ms.

6.4.4 Application on human data

Preliminary in-vivo data comprised a standard GRE with multiple echo times along a single 2D slice for a reference T_2^* mapping, a standard structural MPRAGE, the original 3D-PNP-MRF sequence and the implemented MRF-vTE sequence collected using two patterns of T_E to demonstrate their different effectiveness.

Collected images and relaxation maps are shown in 6.4.6 for a representative transversal slice. Despite the extreme acceleration levels employed, the MRF reconstruction and sequence framework provided adequate geometrical accuracy in agreement with the structural MPRAGE (Figure 6.4.6, first row on left) in posterior areas while frontal lobe areas exhibited strong T_1 estimation bias with both the original MRF sequence (Figure 6.4.6, second row) and implemented MRF-vTE variants (Figure 6.4.6, third and fourth row). Even if this bias corrupted the T_1 of frontal structures (as well as T_2^*), the underlying anatomy is possibly geometrically preserved (with all MRF implementations) observing the underlying interfaces. Instead, the T_1 estimated with all the MRF sequences in other brain areas was in high agreement with the literature values for GM and CSF while the WM appears slightly overestimated (up to 10% higher than reference) at 7T. The estimated B_1^+ field amplitude and spatial distribution was consistent with the prescribed FA pattern.

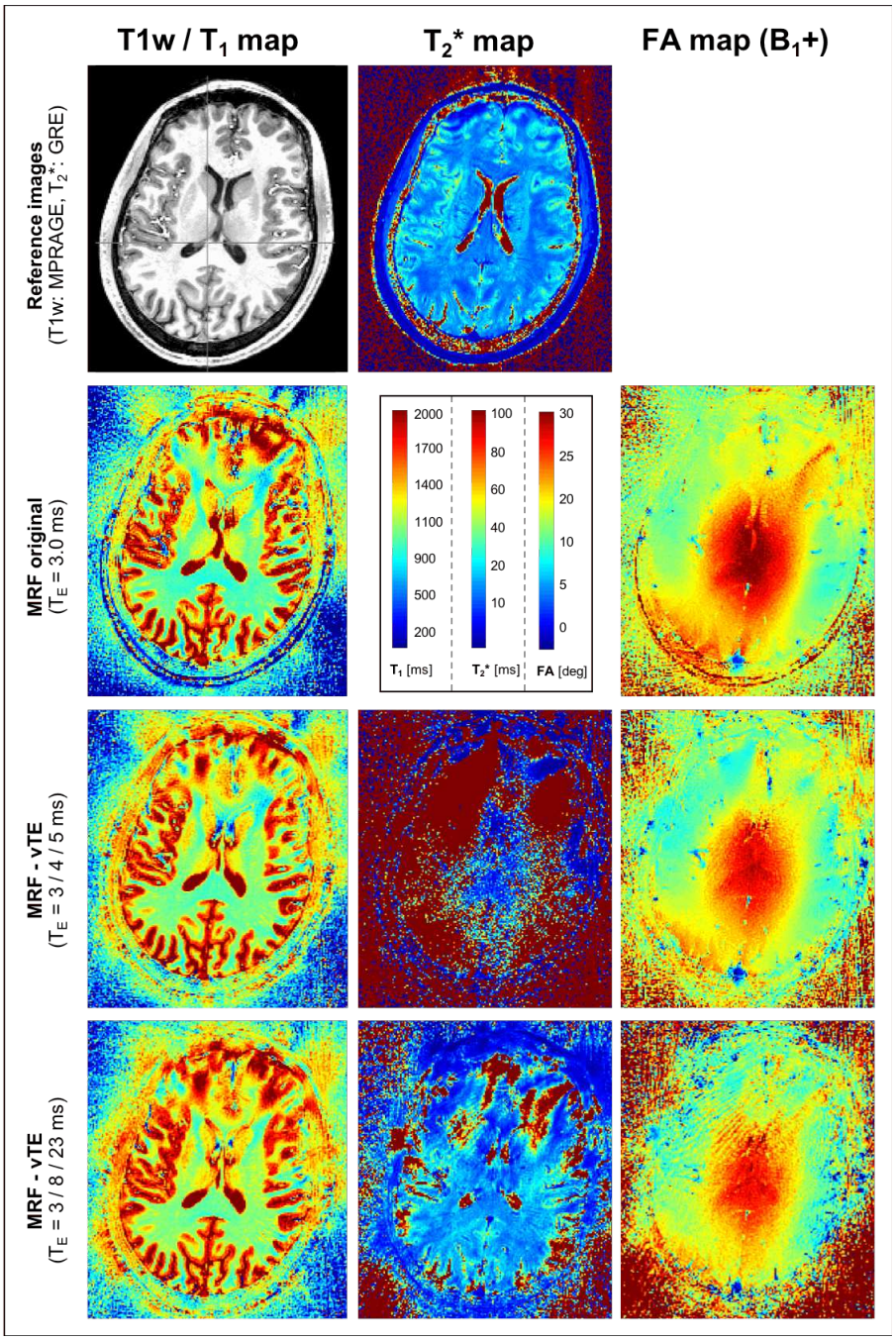

Figure 6.4.6: MRF results in-vivo at 7T. Comparisons of estimation results using a standard MPRAGE or ME-GRE for T_2^* mapping (first row on top) rather than the original 3D-PNP-MRF (second row) or the implemented MRF-vTE (third and fourth row) showing the obtained T_1, T_2^* and FA (B_1^+) maps using two different T_E patterns.

Regarding T_2^* estimation, the MRF-vTE implementation with lower T_E (Figure 6.4.6, third row) exhibited very poor estimation results with estimates saturated (overestimated) at the dictionary top value of 100 ms other than the brain middle where the FA is consistently high. This result was in agreement with the limited MRF sensitivity making it unusable for any application. Interestingly though, the associated T_1 map obtained was in high agreement with the T_1 supplied with the original MRF testifying how the poor T_2^* contrast actually did not affect the estimation accuracy of other parameters. The same applied for the B_1^+ spatial pattern while its actual amplitude is underestimated by as much as 17% compared to the original MRF.

Instead, using a pattern of higher TE (Figure 6.4.6, fourth row) provided more adequate T_2^* estimate with a comparable range to the T_2^* reference map. However, even if the WM amplitude appears to be in quantitative agreement with the reference except for frontal lobe areas, highly distorted and affected from the same bias exhibited by the T_1. Also the cortical GM (omitting the GM with some partial volume with CSF, possibly affected by reconstruction uncertainty due to unresolved aliases over the CSF, observed to be a strong GRE signal source) generally had T_2^* values similar to the reference map but the image quality is locally acceptable only along posterior brain areas where the higher T_E spent actually give sufficient sensitivity leaving the only remaining bias over very high T_2^* values as those involving the CSF ($T_2^* > 100ms$) eventually related to limitations in dictionary coverage as well as limited MRF sensitivity to such long decay rates.

Again, the T_2^* estimate and geometrical accuracy was best in middle brain areas both for WM and GM where the possible SNR role offered by high FA favoured clean T_2^* estimates. Note that the reference T_2^* map as well exhibited some frontal lobe uncertainty and distortions in spatial agreement with those observed with MRF sequences while the MPRAGE exhibit no clear issues in such location. This result suggest that a T_E pattern encompassing 15 to 25 ms could be sufficient to provide adequate T_2^* contrast over the signal variations under this under sampling and noise

condition, other artefacts involving frontal lobe are thought to be related to hardware miscalibration effects (possibly affecting gradient timing accuracy) further exacerbated by a locally poor B_1^+ to be accounted for in future applications with suitable calibrations and more homogeneous B_1^+ application.

A second human scan session improved on previous MRF sequence limitations collecting the original 3D-PNP-MRF sequence and MRF-vTE sequence using a single T_E pattern for quantification simplicity.
Encountered effects of miscalibrated hardware on MRF is demonstrated in figure 6.4.7. The estimated M_0 without any correction (second box from left, 0 px shift) exhibit a consistent inhomogeneity bias not related to the underlying apparent proton density nor to the possible receive inhomogeneity profile expected from the coil sensitivity.
We conjectured that this stems from a not perfectly calibrated gradient system, where the rise delay of one or possibly more imaging gradients, resulting in a coarse modulation of M_0.

To test for this effect we provided a simple correction strategy which assumes the gradient delay errors are mostly resulting in activation delays that correspond in k-space to a linear shift along the prescribed trajectory. As resulting from discrete delay blocks caused by this effect, we considered a correction scheme that shifts each acquired k-space line by -1 to +3 points along the spoke direction (see 6.4.7) adapting the prescribed k-space trajectory and sampling before the image reconstruction rather than applying k-space interpolations.

Within this scheme a gradient anticipation would correspond to a k-space line (spoke) acquired earlier along the trajectory, accounted by anticipating the ideal spoke trajectory by 1 pixel whereas positive delays would result in effectively measured data later on the spoke direction, to be accounted for by positive shifts along the trajectory as demonstrated in Figure 6.4.7-A for a range of discrete shifts.

The resulting M_0 obtained by providing different k-space shift to each acquired spoke is represented in Figure 6.4.7-B. As can be clearly ob-

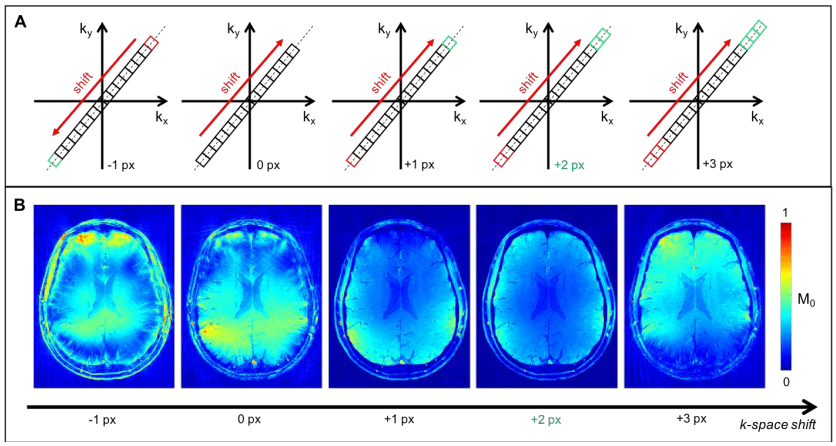

Figure 6.4.7: Effect of delayed k-space trajectory. Representation of a single spoke (A) consisting on consecutive points to be shifted along the spoke direction of discrete positions to mimic the effects of gradient delays from -1 point to $+3$ points. The M_0 estimated (B) with the original 3D-PNP-MRF with no shift of collected spokes exhibited significant background amplitude modulation possibly correlated to gradient delays effects. Negative shifts exacerbated the issue visually whereas a positive $+2$ points (pixels) shift restored the expected M_0 pattern based on the brain proton density modulated by the unresolved coil sensitivities (B_1^-).

served, gradient delays did not anticipate the data acquisition (left box) from the biased M_0 appearance. Rather, they are providing an error more possibly accounted by a discrete shift of two positions along the spoke (+2 pixels) as the obtained M_0 appears consistent with the ideal proton density in overlay with the receive sensitivity while additional shifts actually worsen the observed bias.

The results of this correction scheme are showed in Figure 6.4.8-A regarding the estimated T_1 map using the original MRF sequence implementation along increasing k-space shifts applied. Passing from no shift (+0 px) to the chosen shift (+2 px) it is clear that the frontal bias observed in the first subject could have been ameliorated by such a correction scheme as the frontal bias could be well described by a frontal bias also in the second, eventually corrected by the trajectory shift.

However, even if overall effective, the T_1 estimate in cortical GM of posterior brain areas start to suffer from an increased artefact content and

lower T_1 as compared to frontal brain areas (with relative difference up to 13% in terms of T_1) suggesting how the correction scheme helps but not completely accounted for trajectory errors. Figure 6.4.8-B showed how the implemented correction reversed a strongly biased T_1 and T_2^* maps obtained with MRF-vTE to maps with decent structural quality without any sequence improvements other than post-processing trajectory corrections (i.e. k-space shifts before image reconstruction). Even if similar improvements were obtained with the MRF-vTE in terms of T_1 mapping as compared to the original MRF sequence, striking effects interested the T_2^* quantification (while the B_1^+ mapping exhibit consistent results regardless of any trajectory shift).

Interestingly, the frontal bias which completely disrupted the T_2^* quantification (Figure 6.4.8-B, middle column) was resolved by the correction providing whole-brain level improvements (showed in Figure 6.4.9, top row) in terms of structural delineation and literature agreement for CSF and GM while locally inflated T_2^* regarding the WM.

The local structural appearance of T_2^* was still noisy after the correction (showed in Figure 6.4.9, bottom row and middle column), offering limited CSF/GM and dura distinguishability to be eventually used to enhance cortical delineations but this could be improved by enhancing the MRF pattern sensitivity, currently not strictly optimized as previously stated.

6.5 Considerations and future perspectives

A novel framework for brain cortex segmentation has been proposed. Building upon the idea of using more than the T_1 relaxation to better distinguish cortical GM from meninges as proposed by van Der Kouwe et al., (van der Kouwe et al., 2008), we generalized the image collection for accurate cortical segmentation applying the MRF concept for quantitative MRI combined with synthetic MRI for arbitrary contrast generation.

In this preliminary study, we tackled the MRF sequence implementa-

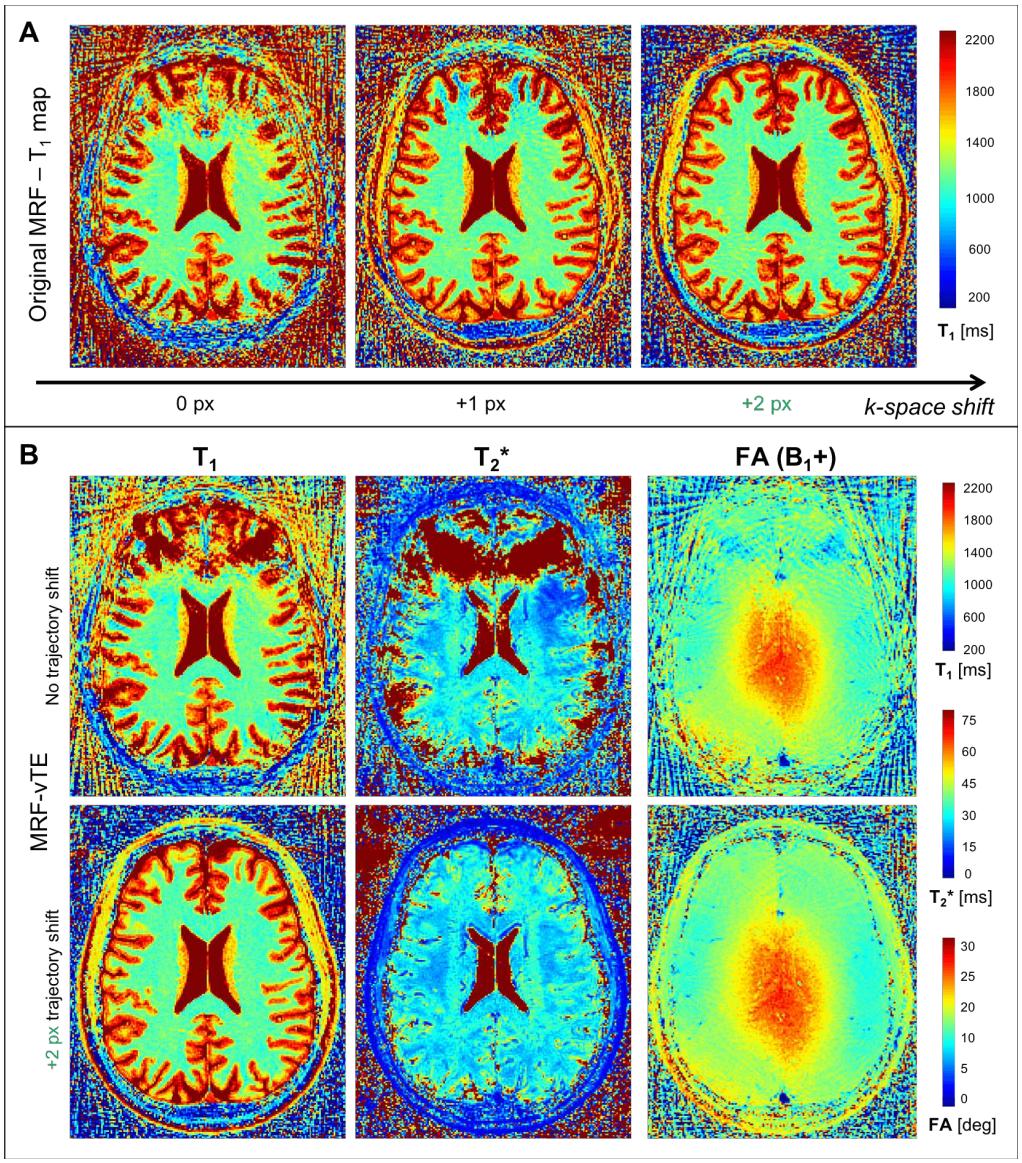

Figure 6.4.8: MRF results with delay correction. A) T_1 estimates obtained using the original 3D-PNP-MRF sequence with no correction to the suggested correction ($+2$ points shift) from left to right. B) T_1, T_2^* and B_1^+ estimates obtained with MRF-vTE without (top row) or with suggested shift correction (bottom row) showing the recovery of anatomical accuracy and T_2^* sensitivity using identical parameterization of the MRF sequence.

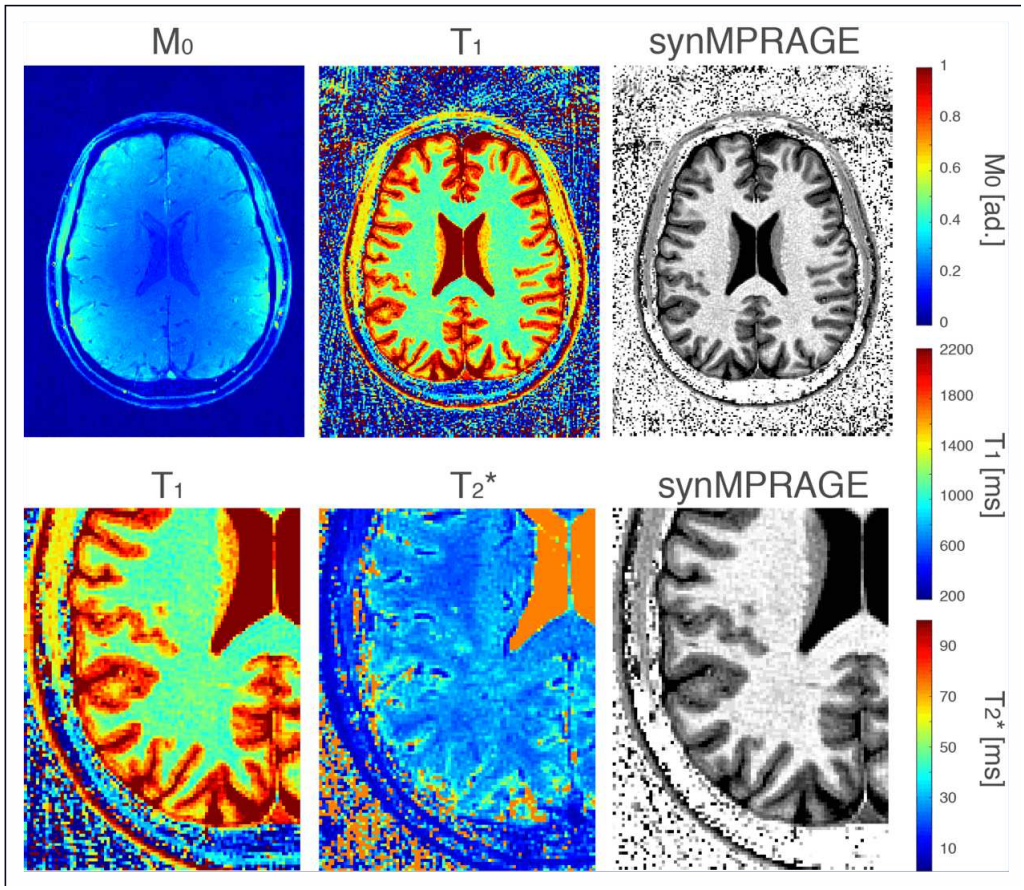

Figure 6.4.9: Effect of delay correction over MRF and synMPR. Quantification results and synthetic MPRAGE obtained with MRF-vTE after gradient delay correction showing whole-brain (top row) improvements in estimation accuracy as well as literature agreement while locally providing enhanced anatomical accuracy (bottom row) but still noisy T_2^* results out of brain.

tion for robust and whole-brain qMRI measurement. As we focused on cortical segmentation errors resulting from poorly segregated GM from dura structure, we first explored literature values for T_1 and T_2^* of dura to identify a suitable T_2^* sensitivity range. A previous 3D-MRF implementation was therefore extended to provide such T_2^* estimation capability along with T_1 relaxation and B_1^+ (that is the FA spatial distribution), encountering however, hardware-related hurdles as well as some local limitations in terms of tissue delineation accuracy with T_2^*.
Quantitative parametric consistency was confirmed in phantom and preliminarily evaluated on human brain data, demonstrating the contrast homogeneity potential and anatomical accuracy of synthetic MPRAGEs obtained from T_1 relaxation in comparison to the standard MPRAGE (acquired) still affected by coarse and scanner-dependent intensity and contrast performances.

We also portrayed the disrupting effect of hardware-related inaccuracies over qMRI measures, in this study possibly arising from the imaging gradient delays which caused significant k-space trajectory deviations from the expected one during reconstruction providing strong background modulations which disrupted any possible model-based consideration if unaccounted for with the radial readout scheme considered. T_2^* estimates were found to be particularly sensitive to these inaccuracies. Moreover, limited B_1^+ performances were connected to a locally poor SNR which as well resulted in inconsistent dictionary matching results and anatomically unreliable cortical delineations impeding its correct delineation.

Currently observed limitations are still limiting the effectiveness of T_2^* estimate to resolve accurately GM from dura while a first step was offered even using only T_1 relaxation to generate a synthetic MPRAGE which strongly contrast with +/- 1 voxel of spatial error the external GM limit, serving as primary confidence interval to be restricted when a more consistent T_2^* information is locally available. Realistically, refining the MRF reconstruction to make it less sensitive to hardware-related inaccuracies (within a radial readout design) while providing more homogeneous B_1^+,

for example shifting from 7T to 3T, is expected to significantly improve the MRF estimation results while promising direct inter-subject comparability improvements in any subsequent functional connectivity analysis.

One fundamental limitation to be addressed in future studies is the MRF optimisation process, currently mostly based upon empirical considerations without clear evidence for optimality of the prescribed FA, T_E, T_R pattern both in terms of actual scan time or sensitivity of simulated dynamics for example to T_2^* relaxation. Examples of the impact of such optimisation on the estimation accuracy were reported without however providing conclusive evidence toward a single sequence parameterisation. In practice, this optimisation tool will generalize the concept of MRF dictionary sensitivity to any model parameter in order to let the researcher choose which parameter, and within which parametric range, is to be emphasized by the MRF sequence parameters removing the need for manual tuning of T_E as currently done.

However, even guaranteeing optimal sensitivity to a defined T_2^* range, its estimation accuracy is still limited within the implemented framework. In fact, to have a significant T_2^* contribution over MRF signals, the T_E needs to be sufficiently long and possibly along a comparable temporal scale to the aimed T_2^*. Therefore, to measure brain-like T_2^* values the baseline T_E/T_R values adopted of 3/8 ms should be widely increased for example to 15/20 ms (GM is still not clearly distinguished from WM even considering T_E/T_R = 10/15 ms) making the actual scan time proportionally longer (five times more) to the point of being practically unfeasible even implementing additional under sampling strategies to accelerate the data collection. To overcome this limit the implemented framework could consider the T_2 relaxation instead of T_2^* benefiting of the MRF sequence flexibility to switch some FLASH-based kernels to correspondent FISP segments needed to introduce a proper T_2 weight without prohibitively long T_R, however still requiring an adequate MRF pattern optimisation method.

Dont cling to a mistake just because you spent a lot of time making it.

Aubrey De Graf

7 Conclusions

Describing the macroscopic brain communication structure based on inter-areal correlation provided crucial insights about the fundamental brain organization. It offered a powerful characterization tool to study the brains response to pathologies such as Alzheimers Disease to psychiatric conditions like Schizophrenia. Nevertheless, there is no general consensus about the best experimental approach to determine the brains fundamental organization. Different approaches provided, in fact, only partially overlapping evidence for example combining brain connectivity estimates derived from diffusion MRI data (i.e. structural connectivity) and functional MRI data (i.e. functional connectivity).
In particular, there is very limited biological support for many of the interesting topological features observed in estimated brain networks currently interpreted mostly from a high level cognitive perspective.

To solve this issue, we have drawn inspiration from the final sentence of the work by Raichle at al., (Raichle, 2006) proposing as major challenge for the neuroscience community the understanding of the association between brain functions and the underlying energy consumption.

With the aim of providing further, biologically-motivated, evidence to the obtained network structures while possibly discarding unlikely features, we have resorted to a multi-modal measure of brain connectivity (FC) and local glucose metabolism (18F-FDG-PET). Using literature available multi-modal data, the first study reported in this dissertation (Chapter 4) investigated whether group-level measures of FC can be associated to the local glucose metabolism in resting state condition.
The group-average FC topological organization of different subjects was summarized by means of interpretable local measures derived from graph theory.

Single functional connections (referred as links or edges) were not able to explain the local metabolic activity of linked areas (referred as network nodes). Instead, the entire set of connections interesting each functional area (defined as connectivity profile) shaped the local metabolic activity: nodes with similar connectivity profile were found to be more metabolically similar than randomly chosen ones suggesting a background modulation effect over glucose metabolism from by the FC structure. However, among all local topological features considered, the most effective in explaining the brain's metabolic activity was the total connectivity of each node (i.e. node strength) in agreement with similar analysis performed voxel-wise or at network level. Furthermore, this association was more clearly mediated by short-range and between-network connections.

However, the explanatory power of such metric was quite limited in quantitative terms and affected by significant departures from the eventually linear relationship. These departures highlight a possible network-related metabolic behavior in resting state involving dynamic adaptation mechanisms. The metabolic activity of high-rank network nodes, backbone of the brain network, was found to be consistently tuned by their connectivity and modulated according to their role in the network as compared to non-central nodes, casting light on the previously observed abrupt metabolic alteration paralleled by a functional connectivity loss observed in many of such nodes under pathologic conditions. Afterwards, macroscopic level communication structures did not clearly

support inter-areal connectivity if not in a specific subset of functionally central brain areas. The regional metabolism nonetheless was a valuable tool to comprehend and guide network structure selection, promoting physiologically plausible structures able to mimic relevant pathologic alterations.

This first study was limited by the need of considering group-level FC structures and experiments with limited explanatory power also from the metabolic perspective. Recent studies pointed out the benefits of single-subject evaluations of the FC structure as well as its energy metabolism to overcome spurious variability effects and avoid group-level considerations that can mask out relevant connectivity-metabolism effects impossible to study without the sensitivity offered by single subject investigations. However, if the brains FC structure is poorly understood at group level, at single-subject level the estimation is possibly also confounded by nuisance effects able to impair genuine FC estimations making it difficult to disentangle spurious FC structural variabilities from subject-specific brain architecture optimizations.

To provide consistent FC estimate at single subject level to be employed in future multi-modal studies that makes use of hybrid PET/MRI scanners, in the second part of the dissertation (Chapter 5) we performed a protocol optimization study aimed at detecting suitable experimental protocols. The optimization was based upon principles drawn from task-fMRI literature, which suggest to promote thermal noise regime in order to minimize spurious spatial correlations. We reframed the concept for resting state FC demonstrating the advantages of such a noise regime and proposing experimental protocols based also on the noise nature while indicating how the FC structure (based on linear correlation measures) can be amplitude-modulated by the actual noise regime and level, possibly masking interesting effects during between subjects comparisons.

The optimization study was purposely extended as a two-stage optimization to evaluate the impact of main experimental parameters over the estimated FC structures and the role of propagated noise using current state-of-the-art approaches. We observed a complex interplay be-

tween image accelerations (multi-band, MB; in-plane parallel imaging, iPAT) and prescribed slice orientations highlighting a non-trivial interplay among imaging hardware and reconstruction over the temporal noise propagated in fMRI measurements. We provided strong evidence toward the use of non-transversal slice orientations to make the most of MB acceleration within the available setup promoting three experimental settings that satisfied our request for spatio-temporal sampling rate. These three settings were further explored in a test/retest application (matched protocols) to obtain single-subject FC matrices and evaluate their sensitivity to a changing, although very similar experimental protocol. The FC matrices obtained exhibited structured differences over many middle and lower-brain areas, whose connectivity (along with inferred brain network features) was positively correlated to the tSNR loss experienced in these areas with increasing image accelerations particularly related to the iPAT usage, ultimately able to promote gross temporal signal-to-noise (tSNR) variations explaining most of the observed FC differences among settings.

Based on these observations we encourage the use of different slice orientations to exploit MB acceleration to enhance both fMRI scanning capabilities and BOLD sensitivity without ignoring the need for careful experimental optimization to provide tolerable noise levels as we pointed out that even consistently similar experimental protocols can indeed provide different FC estimates. A practical limitation encountered during the first multi-modal study performed on literature data regarded the definition of a suitable structural support for FC evaluation. Typical FC data preprocessing after suitable denoising requires the registration of such data over a structural support consisting of high-resolution structural images which can be automatically segmented for example to delimit brain areas to define functional network nodes.

However, structural images can be corrupted by artefacts (e.g. motion) as well as exhibit variable contrast across brain structures eventually resulting in poor segmentation outcomes. As described in Chapter 6, to avoid local FC confounds the manual correction of segmentation errors

for example involving cortical delineation inaccuracies is mandatory. In the last part of this dissertation (Chapter 6), we propose a novel structural imaging framework using experimental methods robust to motion effect combined with that allows for more flexible designs in order to minimize the manual interventions needed offering an approach less dependent over the used sequence and scanner. The collection of structural images was replaced by state-of-the-art quantitative MRI approaches based on Magnetic Resonance Fingerprint (MRF) to provide high-resolution relaxation maps subsequently used to generate images with arbitrary MRI contrasts (synthetic MRI) making the actual automatic segmentation more robust to artifacts (e.g. related to motion or gross intensity inhomogeneity) and virtually independent from the used sequence and scanner.

We formulated this framework as a proof of concept within an automatic pipeline. A dedicated 3D MRF sequence was developed to enable high-resolution relaxation mapping with feasible scan time allowing for enhanced motion robustness and experimental flexibility. We also demonstrated in-silico the feasibility of a parallel-imaging implementation based on view sharing, regular k-space under-sampling and conjugate-gradient sensitivity encoding reconstruction to further enhance the MRF scan time. The implemented sequence was able to determine within same imaging space T_1 and T_2^* relaxation without B_0 and B_1^+ effects. The usage of T_2^* was considered upon previous suggestions about its useful application to accurately distinguish brain cortex from meninges. We demonstrated the parametric accuracy of obtained relaxation estimates over phantom data and preliminarily evaluated its application in-vivo. However, we encountered a disruptive effect from hardware-related inaccuracies over qMRI measures (particularly T_2^*) which required further development of more flexible image reconstructions for example to cope with inaccurate k-space trajectories. As the implementation and preliminary evaluation was carried out on healthy subjects with a 7T scanner, another limiting effect was due to locally poor B_1^+ performances resulting in poor SNR underlying to inconsistent relaxation estimates

mostly involving frontal and temporal brain areas. More homogeneous B_1^+ conditions as well as correction for imaging errors provided consistently higher quality relaxation maps in good qualitative and quantitative agreement to reference relaxation methods and literature. Further refinements of the MRF reconstruction as well as shifting from 7T to 3T is expected to significantly improve the MRF estimation results, promising to achieve performances at least comparable with current standard structural images while offering enhanced robustness to motion and flexibility in contrast generation.

In conclusion, this dissertation showed that the use of consistent biological information can help to study the brains functional connectivity architecture uncovering its main organizational features to support a more extensive clinical application. Moreover, this work demonstrates the benefit and limitations of current FC approaches at single-subject level as well as its eventual dependence over the noise level demanding for more clear guidelines to the researcher interested in resting state FC assessment. The evaluated FC protocols will soon be applied in a multimodal PET/fMRI study aimed at extensive sampling of single-subject features (healthy subjects) carried out within a joint collaboration between the University hospital of Padova (Nuclear Medicine unit, Department of Medicine, Padova, Italy), the Padova Neuroscience center (University of Padova, Italy) and the Department of information engineering of the University of Padova (Padua, Italy).

Finally, a generalized structural imaging framework was proposed to offer more robust structural support to functional analyses while providing quantitative tissue characterization requiring less manual tuning. This approach is applicable on different scanners within in a completely automatic pipeline also aimed at maintaining a convenient separation layer between the experimental scanning sequence, image generation and processing useful for a better system maintenance but still requiring methodological improvements from the relaxation mapping method side.

Bibliography

Achard, S. and Bullmore, E. (2007). Efficiency and cost of economical brain functional networks. *PLoS computational biology*, 3(2):e17.

Aiello, M., Salvatore, E., Cachia, A., Pappatà, S., Cavaliere, C., Prinster, A., Nicolai, E., Salvatore, M., Baron, J. C., and Quarantelli, M. (2015). Relationship between simultaneously acquired resting-state regional cerebral glucose metabolism and functional MRI: A PET/MR hybrid scanner study. *NeuroImage*, 113:111–121.

Anderson, J., Ferguson, M., Lopez-Larson, M., and Yurgelun-Todd, D. (2011). Reproducibility of Single-Subject Functional Connectivity Measurements. *American Journal of Neuroradiology*, 32(3):548–555.

Arbabshirani, M. R., Damaraju, E., Phlypo, R., Plis, S., Allen, E., Ma, S., Mathalon, D., Preda, A., Vaidya, J. G., Adali, T., and Calhoun, V. D. (2014). Impact of autocorrelation on functional connectivity. *NeuroImage*, 102:294–308.

Avants, B. B., Tustison, N. J., Song, G., Cook, P. A., Klein, A., and Gee, J. C. (2011). A reproducible evaluation of ANTs similarity metric performance in brain image registration. *NeuroImage*, 54(3):2033–44.

Badea, L., Onu, M., Wu, T., Roceanu, A., and Bajenaru, O. (2017). Exploring the reproducibility of functional connectivity alterations in Parkinson's disease. *PLOS ONE*, 12(11):e0188196.

Bandettini, P. A., Jesmanowicz, A., Wong, E. C., and Hyde, J. S. (1993). Processing strategies for time-course data sets in functional MRI of the human brain. *Magnetic resonance in medicine*, 30(2):161–73.

Beckmann, C. F., DeLuca, M., Devlin, J. T., and Smith, S. M. (2005). Investigations into resting-state connectivity using independent component analysis. *Philosophical Transactions of the Royal Society B: Biological Sciences*, 360(1457):1001–1013.

Behzadi, Y., Restom, K., Liau, J., and Liu, T. T. (2007). A component based noise correction method (CompCor) for BOLD and perfusion based fMRI. *NeuroImage*, 37(1):90–101.

Benjamini, Y. and Hochberg, Y. (1995). Controlling the False Discovery

Rate: A Practical and Powerful Approach to Multiple Testing.

Bernstein, M., King, K., and Zhou, X. (2004). *Handbook of MRI Pulse Sequences*. Elsevier Science.

Bertoldo, A., Vicini, P., Sambuceti, G., Lammertsma, A. A., Parodi, O., and Cobelli, C. (1998). Evaluation of compartmental and spectral analysis models of [18F]FDG kinetics for heart and brain studies with PET. *IEEE Transactions on Biomedical Engineering*, 45(12):1429–1448.

Biswal, B., Yetkin, F. Z., Haughton, V. M., and Hyde, J. S. (1995a). Functional connectivity in the motor cortex of resting human brain using echo-planar MRI. *Magnetic resonance in medicine*, 34(4):537–41.

Biswal, B., Zerrin Yetkin, F., Haughton, V. M., and Hyde, J. S. (1995b). Functional connectivity in the motor cortex of resting human brain using echo-planar mri. *Magnetic Resonance in Medicine*, 34(4):537–541.

Biswal, B. B., Mennes, M., Zuo, X.-N., Gohel, S., Kelly, C., Smith, S. M., Beckmann, C. F., Adelstein, J. S., Buckner, R. L., Colcombe, S., Dogonowski, A.-M., Ernst, M., Fair, D., Hampson, M., Hoptman, M. J., Hyde, J. S., Kiviniemi, V. J., Kotter, R., Li, S.-J., Lin, C.-P., Lowe, M. J., Mackay, C., Madden, D. J., Madsen, K. H., Margulies, D. S., Mayberg, H. S., McMahon, K., Monk, C. S., Mostofsky, S. H., Nagel, B. J., Pekar, J. J., Peltier, S. J., Petersen, S. E., Riedl, V., Rombouts, S. A. R. B., Rypma, B., Schlaggar, B. L., Schmidt, S., Seidler, R. D., Siegle, G. J., Sorg, C., Teng, G.-J., Veijola, J., Villringer, A., Walter, M., Wang, L., Weng, X.-C., Whitfield-Gabrieli, S., Williamson, P., Windischberger, C., Zang, Y.-F., Zhang, H.-Y., Castellanos, F. X., and Milham, M. P. (2010). Toward discovery science of human brain function. *Proceedings of the National Academy of Sciences*, 107(10):4734–4739.

Bloch, F., Hansen, W. W., and Packard, M. (1946). The Nuclear Induction Experiment. *Physical Review*, 70(7-8):474–485.

Block, K. T., Chandarana, H., Milla, S., Bruno, M., Mulholland, T., Fatterpekar, G., Hagiwara, M., Grimm, R., Geppert, C., Kiefer, B., and Sodickson, D. K. (2014). Towards Routine Clinical Use of Radial Stack-of-Stars 3D Gradient-Echo Sequences for Reducing Motion Sensitivity. *Journal of the Korean Society of Magnetic Resonance in Medicine*, 18(2):87.

Blondel, V. D., Guillaume, J.-L., Lambiotte, R., and Lefebvre, E. (2008). Fast unfolding of communities in large networks. *Journal of Statistical Mechanics: Theory and Experiment*, 2008(10):P10008.

Blystad, I., Warntjes, J., Smedby, O., Landtblom, A.-M., Lundberg, P., and Larsson, E.-M. (2012). Synthetic Mri of the Brain in a Clinical Setting. *Acta Radiologica*, 53(10):1158–1163.

Bobman, S. A., Riederer, S. J., Lee, J. N., Suddarth, S. A., Wang, H. Z.,

Drayer, B. P., and MacFall, J. R. (1985). Cerebral magnetic resonance image synthesis. *AJNR. American journal of neuroradiology*, 6(2):265–9.

Breuer, F. A., Kannengiesser, S. A., Blaimer, M., Seiberlich, N., Jakob, P. M., and Griswold, M. A. (2009). General formulation for quantitative G-factor calculation in GRAPPA reconstructions. *Magnetic Resonance in Medicine*, 62(3):739–746.

Bright, M. G., Tench, C. R., and Murphy, K. (2017). Potential pitfalls when denoising resting state fMRI data using nuisance regression. *NeuroImage*, 154:159–168.

Buckner, R. L., Sepulcre, J., Talukdar, T., Krienen, F. M., Liu, H., Hedden, T., Andrews-Hanna, J. R., Sperling, R. A., and Johnson, K. A. (2009). Cortical Hubs Revealed by Intrinsic Functional Connectivity: Mapping, Assessment of Stability, and Relation to Alzheimer's Disease. *Journal of Neuroscience*, 29(6):1860–1873.

Bullmore, E. and Sporns, O. (2009). Complex brain networks: graph theoretical analysis of structural and functional systems. *Nature Reviews Neuroscience*, 10(3):186–198.

Bullmore, E. and Sporns, O. (2012). The economy of brain network organization. *Nature Reviews Neuroscience*.

Buonincontri, G. and Sawiak, S. J. (2016). MR fingerprinting with simultaneous B1 estimation. *Magnetic Resonance in Medicine*, 76(4):1127–1135.

Byrnes, K. R., Wilson, C. M., Brabazon, F., von Leden, R., Jurgens, J. S., Oakes, T. R., and Selwyn, R. G. (2014). FDG-PET imaging in mild traumatic brain injury: a critical review. *Frontiers in Neuroenergetics*, 5.

Callaghan, M. F., Mohammadi, S., and Weiskopf, N. (2016). Synthetic quantitative MRI through relaxometry modelling. *NMR in Biomedicine*, 29(12):1729–1738.

Catana, C. (2017). Principles of Simultaneous PET/MR Imaging. *Magnetic Resonance Imaging Clinics of North America*, 25(2):231–243.

Cauley, S. F., Polimeni, J. R., Bhat, H., Wald, L. L., and Setsompop, K. (2014). Interslice leakage artifact reduction technique for simultaneous multislice acquisitions. *Magnetic Resonance in Medicine*, 72(1):93–102.

Cecchin, D., Palombit, A., Castellaro, M., Silvestri, E., Bui, F., Barthel, H., Sabri, O., Corbetta, M., and Bertoldo, A. (2017). Brain PET and functional MRI: Why simultaneously using hybrid PET/MR systems? *Quarterly Journal of Nuclear Medicine and Molecular Imaging*, 61(4):345–359.

Chen, B., Xu, T., Zhou, C., Wang, L., Yang, N., Wang, Z., Dong, H.-M., Yang, Z., Zang, Y.-F., Zuo, X.-N., and Weng, X.-C. (2015). Individual Variability and Test-Retest Reliability Revealed by Ten Re-

peated Resting-State Brain Scans over One Month. *PLOS ONE*, 10(12):e0144963.

Chiang, S., Stern, J. M., Engel, J., and Haneef, Z. (2015). Structural-functional coupling changes in temporal lobe epilepsy. *Brain Research*, 1616:45–57.

Choe, A. S., Jones, C. K., Joel, S. E., Muschelli, J., Belegu, V., Caffo, B. S., Lindquist, M. A., Van Zijl, P. C. M., and Pekar, J. J. (2015). Reproducibility and Temporal Structure in Weekly Resting-State fMRI over a Period of 3.5 Years.

Cloos, M. A., Knoll, F., Zhao, T., Block, K. T., Bruno, M., Wiggins, G. C., and Sodickson, D. K. (2016). Multiparametric imaging with heterogeneous radiofrequency fields. *Nature Communications*, 7:12445.

Cole, M. W., Bassett, D. S., Power, J. D., Braver, T. S., and Petersen, S. E. (2014). Intrinsic and Task-Evoked Network Architectures of the Human Brain. *Neuron*, 83(1):238–251.

Dale, A. M., Fischl, B., Sereno, M. I., Dale, A. M., Fischl, B., and Sereno, M. I. (1999). Cortical Surface-Based Analysis. *NeuroImage*, 9(2):179–194.

Deco, G., Tononi, G., Boly, M., and Kringelbach, M. L. (2015). Rethinking segregation and integration: contributions of whole-brain modelling. *Nature Reviews Neuroscience*, 16(7):430–439.

Dennis, E. L. and Thompson, P. M. (2014). Functional Brain Connectivity Using fMRI in Aging and Alzheimer's Disease. *Neuropsychology Review*, 24(1):49–62.

Deshpande, G. and Hu, X. (2012). Investigating Effective Brain Connectivity from fMRI Data: Past Findings and Current Issues with Reference to Granger Causality Analysis. *Brain Connectivity*, 2(5):235–245.

Desikan, R. S., Ségonne, F., Fischl, B., Quinn, B. T., Dickerson, B. C., Blacker, D., Buckner, R. L., Dale, A. M., Maguire, R. P., Hyman, B. T., Albert, M. S., and Killiany, R. J. (2006). An automated labeling system for subdividing the human cerebral cortex on MRI scans into gyral based regions of interest. *NeuroImage*, 31(3):968–980.

Di, X. and Biswal, and Alzheimer's Disease Neu, B. B. (2012). Metabolic Brain Covariant Networks as Revealed by FDG-PET with Reference to Resting-State fMRI Networks. *Brain Connectivity*, 2(5):275–283.

Dobromyslin, V. I., Salat, D. H., Fortier, C. B., Leritz, E. C., Beckmann, C. F., Milberg, W. P., and McGlinchey, R. E. (2012). Distinct functional networks within the cerebellum and their relation to cortical systems assessed with independent component analysis. *NeuroImage*, 60(4):2073–2085.

Doucet, G., Naveau, M., Petit, L., Delcroix, N., Zago, L., Crivello, F., Jo-

bard, G., Tzourio-Mazoyer, N., Mazoyer, B., Mellet, E., and Joliot, M. (2011). Brain activity at rest: a multiscale hierarchical functional organization. *Journal of Neurophysiology*, 105(6):2753–2763.

Ehrhardt, M. J., Markiewicz, P., Liljeroth, M., Barnes, A., Kolehmainen, V., Duncan, J. S., Pizarro, L., Atkinson, D., Hutton, B. F., Ourselin, S., Thielemans, K., and Arridge, S. R. (2016). PET Reconstruction With an Anatomical MRI Prior Using Parallel Level Sets. *IEEE Transactions on Medical Imaging*, 35(9):2189–2199.

Ernst, R. R. and Anderson, W. A. (1966). Application of Fourier Transform Spectroscopy to Magnetic Resonance. *Review of Scientific Instruments*, 37(1):93–102.

ESR (2015). Magnetic Resonance Fingerprinting - a promising new approach to obtain standardized imaging biomarkers from MRI. *Insights into Imaging*, 6(2):163–165.

Evans, A. C. (2013). Networks of anatomical covariance. *NeuroImage*, 80:489–504.

Feng, L., Grimm, R., Block, K. T., Chandarana, H., Kim, S., Xu, J., Axel, L., Sodickson, D. K., and Otazo, R. (2014). Golden-angle radial sparse parallel MRI: Combination of compressed sensing, parallel imaging, and golden-angle radial sampling for fast and flexible dynamic volumetric MRI. *Magnetic Resonance in Medicine*, 72(3):707–717.

Fiederer, L., Vorwerk, J., Lucka, F., Dannhauer, M., Yang, S., Dümpelmann, M., Schulze-Bonhage, A., Aertsen, A., Speck, O., Wolters, C., and Ball, T. (2016). The role of blood vessels in high-resolution volume conductor head modeling of EEG. *NeuroImage*, 128:193–208.

Fischl, B., Salat, D. H., Busa, E., Albert, M., Dieterich, M., Haselgrove, C., van der Kouwe, A., Killiany, R., Kennedy, D., Klaveness, S., Montillo, A., Makris, N., Rosen, B., and Dale, A. M. (2002). Whole brain segmentation: automated labeling of neuroanatomical structures in the human brain. *Neuron*, 33(3):341–55.

Fischl, B., Sereno, M. I., and Dale, A. M. (1999). Cortical Surface-Based Analysis. *NeuroImage*, 9(2):195–207.

Fornito, A., Zalesky, A., and Breakspear, M. (2013). Graph analysis of the human connectome: Promise, progress, and pitfalls. *NeuroImage*, 80:426–444.

Forstmann, B. U., Keuken, M. C., Schafer, A., Bazin, P. L., Alkemade, A., and Turner, R. (2014). Multi-modal ultra-high resolution structural 7-Tesla MRI data repository. *Scientific Data*, 1:1–8.

Fox, M. D. (2010). Clinical applications of resting state functional connectivity. *Frontiers in Systems Neuroscience*.

Fox, M. D., Halko, M. A., Eldaief, M. C., and Pascual-Leone, A. (2012). Measuring and manipulating brain connectivity with resting state functional connectivity magnetic resonance imaging (fcMRI) and transcranial magnetic stimulation (TMS). *NeuroImage*, 62(4):2232–43.

Fox, M. D., Snyder, A. Z., Vincent, J. L., Corbetta, M., Van Essen, D. C., and Raichle, M. E. (2005). From The Cover: The human brain is intrinsically organized into dynamic, anticorrelated functional networks. *Proceedings of the National Academy of Sciences*, 102(27):9673–9678.

Freeman, L. C. (1977). A Set of Measures of Centrality Based on Betweenness. *Sociometry*, 40(1):35.

Friston, K. J. (2011). Functional and Effective Connectivity: A Review. *Brain Connectivity*, 1(1):13–36.

Friston, K. J., Poline, J.-B., Holmes, A. P., Frith, C. D., and Frackowiak, R. S. (1996). A multivariate analysis of PET activation studies. *Human Brain Mapping*, 4(2):140–151.

Girvan, M. and Newman, M. E. J. (2002). Community structure in social and biological networks. *Proceedings of the National Academy of Sciences of the United States of America*, 99(12):7821–6.

Glasser, M. F., Sotiropoulos, S. N., Wilson, J. A., Coalson, T. S., Fischl, B., Andersson, J. L., Xu, J., Jbabdi, S., Webster, M., Polimeni, J. R., Van Essen, D. C., and Jenkinson, M. (2013). The minimal preprocessing pipelines for the Human Connectome Project. *NeuroImage*, 80:105–124.

Glover, G. H. (2011). Overview of Functional Magnetic Resonance Imaging. *Neurosurgery Clinics of North America*, 22(2):133–139.

Golland, Y., Golland, P., Bentin, S., and Malach, R. (2008). Data-driven clustering reveals a fundamental subdivision of the human cortex into two global systems. *Neuropsychologia*, 46(2):540–553.

Gordon, E. M., Laumann, T. O., Adeyemo, B., Huckins, J. F., Kelley, W. M., and Petersen, S. E. (2016). Generation and Evaluation of a Cortical Area Parcellation from Resting-State Correlations. *Cerebral Cortex*, 26(1):288–303.

Gordon, E. M., Laumann, T. O., Gilmore, A. W., Newbold, D. J., Greene, D. J., Berg, J. J., Ortega, M., Hoyt-Drazen, C., Gratton, C., Sun, H., Hampton, J. M., Coalson, R. S., Nguyen, A. L., McDermott, K. B., Shimony, J. S., Snyder, A. Z., Schlaggar, B. L., Petersen, S. E., Nelson, S. M., and Dosenbach, N. U. (2017). Precision Functional Mapping of Individual Human Brains. *Neuron*, 95(4):791–807.e7.

Gratton, C., Laumann, T. O., Nielsen, A. N., Greene, D. J., Gordon, E. M., Gilmore, A. W., Nelson, S. M., Coalson, R. S., Snyder, A. Z., Schlaggar, B. L., Dosenbach, N. U., and Petersen, S. E. (2018). Functional Brain

Networks Are Dominated by Stable Group and Individual Factors, Not Cognitive or Daily Variation. *Neuron*, pages 439–452.

Greicius, M. D., Krasnow, B., Reiss, A. L., and Menon, V. (2003). Functional connectivity in the resting brain: A network analysis of the default mode hypothesis. *Proceedings of the National Academy of Sciences*, 100(1):253–258.

Griffanti, L., Dipasquale, O., Laganà, M. M., Nemni, R., Clerici, M., Smith, S. M., Baselli, G., and Baglio, F. (2015). Effective artifact removal in resting state fMRI data improves detection of DMN functional connectivity alteration in Alzheimer's disease. *Frontiers in Human Neuroscience*, 9.

Griffanti, L., Douaud, G., Bijsterbosch, J., Evangelisti, S., Alfaro-Almagro, F., Glasser, M. F., Duff, E. P., Fitzgibbon, S., Westphal, R., Carone, D., Beckmann, C. F., and Smith, S. M. (2017). Hand classification of fMRI ICA noise components. *NeuroImage*, 154:188–205.

Griswold, M. A., Jakob, P. M., Heidemann, R. M., Nittka, M., Jellus, V., Wang, J., Kiefer, B., and Haase, A. (2002). Generalized autocalibrating partially parallel acquisitions (GRAPPA). *Magnetic Resonance in Medicine*, 47(6):1202–1210.

Grothe, M. J., Barthel, H., Sepulcre, J., Dyrba, M., Sabri, O., Teipel, S. J., and Neuroimaging, D. (2017). In vivo staging of regional amyloid deposition. 0.

Gu, S., Cieslak, M., Baird, B., Muldoon, S. F., Grafton, S. T., Pasqualetti, F., and Bassett, D. S. (2018). The Energy Landscape of Neurophysiological Activity Implicit in Brain Network Structure. *Scientific Reports*, 8(1):1–15.

Guimerà, R. and Nunes Amaral, L. A. (2005). Functional cartography of complex metabolic networks. *Nature*, 433(7028):895–900.

Gulani, V., Schmitt, P., Griswold, M. A., Webb, A. G., and Jakob, P. M. (2004). Towards a single-sequence neurologic magnetic resonance imaging examination: multiple-contrast images from an IR TrueFISP experiment. *Investigative radiology*, 39(12):767–74.

Guo, S., Palaniyappan, L., Yang, B., Liu, Z., Xue, Z., and Feng, J. (2014). Anatomical Distance Affects Functional Connectivity in Patients With Schizophrenia and Their Siblings. *Schizophrenia Bulletin*, 40(2):449–459.

Haacke, E., Brown, R., Thompson, M., and Venkatesan, R. (1999). *Magnetic Resonance Imaging:Imaging: Physical Principles and Sequence Design*. John Wiley and Sons New York.

Haast, R. A. M., Ivanov, D., Formisano, E., and Uluda, K. (2016). Reproducibility and Reliability of Quantitative and Weighted T1 and T2

Mapping for Myelin-Based Cortical Parcellation at 7 Tesla. *Frontiers in Neuroanatomy*, 10(November):1–17.

Hacker, C. D., Laumann, T. O., Szrama, N. P., Baldassarre, A., Snyder, A. Z., Leuthardt, E. C., and Corbetta, M. (2013). Resting State Network Estimation in Individual Subjects. *NeuroImage*, 82:616.

Hämäläinen, M. S. and Ilmoniemi, R. J. (1994). Interpreting magnetic fields of the brain: minimum norm estimates. *Medical & Biological Engineering & Computing*, 32(1):35–42.

Hamberg, L. M., Hunter, G. J., Alpert, N. M., Choi, N. C., Babich, J. W., and Fischman, A. J. (1994). The dose uptake ratio as an index of glucose metabolism: useful parameter or oversimplification? *Journal of nuclear medicine : official publication, Society of Nuclear Medicine*, 35(8):1308–12.

Hennig, J. (1991). Echoes -How to Generate, Recognize,Use or Avoid Them in MR-Imaging Sequences. *Concepts in Magnetic Resonance*, 3:125–143.

Hermundstad, A. M., Bassett, D. S., Brown, K. S., Aminoff, E. M., Clewett, D., Freeman, S., Frithsen, A., Johnson, A., Tipper, C. M., Miller, M. B., Grafton, S. T., and Carlson, J. M. (2013). Structural foundations of resting-state and task-based functional connectivity in the human brain. *Proceedings of the National Academy of Sciences*, 110(15):6169–6174.

Honey, C. J., Kö, R., Breakspear, M., Sporns, O., and Vogt, O. (2007). Network structure of cerebral cortex shapes functional connectivity on multiple time scales.

Hongzhi Wang, Suh, J. W., Das, S. R., Pluta, J. B., Craige, C., and Yushkevich, P. A. (2013). Multi-Atlas Segmentation with Joint Label Fusion. *IEEE Transactions on Pattern Analysis and Machine Intelligence*, 35(3):611–623.

Hwang, D., Kim, K. Y., Kang, S. K., Seo, S., Paeng, J. C., Lee, D. S., and Lee, J. S. (2018). Improving accuracy of simultaneously reconstructed activity and attenuation maps using deep learning. *Journal of Nuclear Medicine*, page jnumed.117.202317.

Hwang, K., Bertolero, M. A., Liu, W. B., and D'Esposito, M. (2017). The Human Thalamus Is an Integrative Hub for Functional Brain Networks. *The Journal of Neuroscience*, 37(23):5594–5607.

Hyvärinen, A. and Smith, S. M. (2013). Pairwise Likelihood Ratios for Estimation of Non-Gaussian Structural Equation Models. *Journal of Machine Learning Research*, 14:111–152.

Jenkinson, M., Beckmann, C. F., Behrens, T. E., Woolrich, M. W., and Smith, S. M. (2012). FSL. *NeuroImage*, 62(2):782–790.

Jeong, J., Gore, J. C., and Peterson, B. S. (2001). Mutual information anal-

ysis of the EEG in patients with Alzheimer's disease. *Clinical neurophysiology : official journal of the International Federation of Clinical Neurophysiology*, 112(5):827–35.

Jo, H. J., Lee, J.-M., Kim, J.-H., Shin, Y.-W., Kim, I.-Y., Kwon, J. S., and Kim, S. I. (2007). Spatial accuracy of fMRI activation influenced by volume- and surface-based spatial smoothing techniques. *NeuroImage*, 34(2):550–564.

Jung, J. H., Choi, Y., and Im, K. C. (2016). PET/MRI: Technical Challenges and Recent Advances. *Nuclear Medicine and Molecular Imaging*, 50(1):3–12.

Junker, B. H., Koschützki, D., and Schreiber, F. (2006). Exploration of biological network centralities with CentiBiN. *BMC bioinformatics*, 7:219.

Kaiser, M. and Hilgetag, C. C. (2006). Nonoptimal Component Placement, but Short Processing Paths, due to Long-Distance Projections in Neural Systems. *PLoS Computational Biology*, 2(7):e95.

Kaiser, M., Hilgetag, C. C., and van Ooyen, A. (2009). A Simple Rule for Axon Outgrowth and Synaptic Competition Generates Realistic Connection Lengths and Filling Fractions. *Cerebral Cortex*, 19(12):3001–3010.

Kang, J., Gao, Y., Shi, F., Lalush, D. S., Lin, W., and Shen, D. (2015). Prediction of standard-dose brain PET image by using MRI and low-dose brain [18 F]FDG PET images. *Medical Physics*, 42(9):5301–5309.

Kendall, M. G. (1938). A NEW MEASURE OF RANK CORRELATION. *Biometrika*, 30(1-2):81–93.

Keyes, J. W. (1995). SUV: standard uptake or silly useless value? *Journal of nuclear medicine : official publication, Society of Nuclear Medicine*, 36(10):1836–1839.

Koji, F., Martijn, A. C., Yuta, U., and Tomohisa, O. (2017). Cortical t1 mapping with 3d mr fingerprinting at 7t using a single transmit channel. In *ISMRM 2018*.

Krüger, G. and Glover, G. H. (2001). Physiological noise in oxygenation-sensitive magnetic resonance imaging. *Magnetic Resonance in Medicine*, 46(4):631–637.

Ladefoged, C. N., Law, I., Anazodo, U., St. Lawrence, K., Izquierdo-Garcia, D., Catana, C., Burgos, N., Cardoso, M. J., Ourselin, S., Hutton, B., Mérida, I., Costes, N., Hammers, A., Benoit, D., Holm, S., Juttukonda, M., An, H., Cabello, J., Lukas, M., Nekolla, S., Ziegler, S., Fenchel, M., Jakoby, B., Casey, M. E., Benzinger, T., Højgaard, L., Hansen, A. E., and Andersen, F. L. (2017). A multi-centre evaluation of eleven clinically feasible brain PET/MRI attenuation correction tech-

niques using a large cohort of patients. *NeuroImage*, 147:346–359.

Lattanzi, R., Zhang, B., Knoll, F., Assländer, J., and Cloos, M. A. (2018). Phase unwinding for dictionary compression with multiple channel transmission in magnetic resonance fingerprinting. *Magnetic Resonance Imaging*, 49(December 2017):32–38.

Lauterbur, P. C. (1973). Image Formation by Induced Local Interactions: Examples Employing Nuclear Magnetic Resonance. *Nature*, 242(5394):190–191.

Lee, M. H., Hacker, C. D., Snyder, A. Z., Corbetta, M., Zhang, D., Leuthardt, E. C., and Shimony, J. S. (2012). Clustering of resting state networks. *PloS one*, 7(7):e40370.

Legéndy, C. R. (1975). Three principles of brain function and structure. *The International journal of neuroscience*, 6(5):237–54.

Liang, X., Wang, J., Yan, C., Shu, N., Xu, K., Gong, G., and He, Y. (2012). Effects of Different Correlation Metrics and Preprocessing Factors on Small-World Brain Functional Networks: A Resting-State Functional MRI Study. *PLoS ONE*, 7(3):e32766.

Lindquist, M. A., Meng Loh, J., Atlas, L. Y., and Wager, T. D. (2009). Modeling the hemodynamic response function in fMRI: Efficiency, bias and mis-modeling. *NeuroImage*, 45(1):S187–S198.

Liu, F., Jang, H., Kijowski, R., Bradshaw, T., and McMillan, A. B. (2018a). Deep Learning MR Imagingbased Attenuation Correction for PET/MR Imaging. *Radiology*, 286(2):676–684.

Liu, Q., Ganzetti, M., Wenderoth, N., and Mantini, D. (2018b). Detecting Large-Scale Brain Networks Using EEG: Impact of Electrode Density, Head Modeling and Source Localization. *Frontiers in Neuroinformatics*, 12.

Liu, T. T. (2017). Reprint of Noise contributions to the fMRI signal: An Overview'. *NeuroImage*, 154:4–14.

Logothetis, N. K. (2002). The neural basis of the blood-oxygen-level-dependent functional magnetic resonance imaging signal. *Philosophical Transactions of the Royal Society B: Biological Sciences*, 357(1424):1003–1037.

Logothetis, N. K., Pauls, J., Augath, M., Trinath, T., and Oeltermann, A. (2001). Neurophysiological investigation of the basis of the fMRI signal. *Nature*, 412(6843):150–157.

Lohmann, G., Margulies, D. S., Horstmann, A., Pleger, B., Lepsien, J., Goldhahn, D., Schloegl, H., Stumvoll, M., Villringer, A., and Turner, R. (2010). Eigenvector Centrality Mapping for Analyzing Connectivity Patterns in fMRI Data of the Human Brain. *PLoS ONE*, 5(4):e10232.

Lucignani, G., Schmidt, K. C., Moresco, R. M., Striano, G., Colombo, F., Sokoloff, L., and Fazio, F. (1993). Measurement of regional cerebral glucose utilization with fluorine-18-FDG and PET in heterogeneous tissues: theoretical considerations and practical procedure. *Journal of nuclear medicine : official publication, Society of Nuclear Medicine*, 34(3):360–369.

Lund, T. E., Madsen, K. H., Sidaros, K., Luo, W.-L., and Nichols, T. E. (2006). Non-white noise in fMRI: Does modelling have an impact? *NeuroImage*, 29(1):54–66.

Lv, H., Wang, Z., Tong, E., Williams, L. M., Zaharchuk, G., Zeineh, M., Goldstein-Piekarski, A. N., Ball, T. M., Liao, C., and Wintermark, M. (2018). Resting-State Functional MRI: Everything That Nonexperts Have Always Wanted to Know. *AJNR. American journal of neuroradiology*.

Ma, D., Gulani, V., Seiberlich, N., Liu, K., Sunshine, J. L., Duerk, J. L., and Griswold, M. A. (2013). Magnetic resonance fingerprinting. *Nature*, 495(7440):187–92.

Magistretti, P. J. and Allaman, I. (2015). A Cellular Perspective on Brain Energy Metabolism and Functional Imaging. *Neuron*, 86(4):883–901.

Mansfield, P. and Grannell, P. K. (1973). NMR 'diffraction' in solids? *Journal of Physics C: Solid State Physics*, 6(22):L422–L426.

Maquet, P., Dive, D., Salmon, E., von Frenckel, R., and Franck, G. (1990). Reproducibility of cerebral glucose utilization measured by PET and the [18F]-2-fluoro-2-deoxy-d-glucose method in resting, healthy human subjects. *European journal of nuclear medicine*, 16(4-6):267–73.

Marblestone, A. H., Wayne, G., and Kording, K. P. (2016). Toward an Integration of Deep Learning and Neuroscience. *Frontiers in Computational Neuroscience*, 10:94.

Marcus, D. S., Harwell, J., Olsen, T., Hodge, M., Glasser, M. F., Prior, F., Jenkinson, M., Laumann, T., Curtiss, S. W., and Van Essen, D. C. (2011). Informatics and Data Mining Tools and Strategies for the Human Connectome Project. *Frontiers in Neuroinformatics*, 5.

Markov, N. T., Ercsey-Ravasz, M. M., Ribeiro Gomes, A. R., Lamy, C., Magrou, L., Vezoli, J., Misery, P., Falchier, A., Quilodran, R., Gariel, M. A., Sallet, J., Gamanut, R., Huissoud, C., Clavagnier, S., Giroud, P., Sappey-Marinier, D., Barone, P., Dehay, C., Toroczkai, Z., Knoblauch, K., Van Essen, D. C., and Kennedy, H. (2014a). A Weighted and Directed Interareal Connectivity Matrix for Macaque Cerebral Cortex. *Cerebral Cortex*, 24(1):17–36.

Markov, N. T., Vezoli, J., Chameau, P., Falchier, A., Quilodran, R., Huis-

soud, C., Lamy, C., Misery, P., Giroud, P., Ullman, S., Barone, P., Dehay, C., Knoblauch, K., and Kennedy, H. (2014b). Anatomy of hierarchy: Feedforward and feedback pathways in macaque visual cortex. *Journal of Comparative Neurology*, 522(1):225–259.

Martinez-Moller, A., Souvatzoglou, M., Delso, G., Bundschuh, R. A., Chefd'hotel, C., Ziegler, S. I., Navab, N., Schwaiger, M., and Nekolla, S. G. (2009). Tissue Classification as a Potential Approach for Attenuation Correction in Whole-Body PET/MRI: Evaluation with PET/CT Data. *Journal of Nuclear Medicine*, 50(4):520–526.

Matsui, T., Omuro, H., Liu, Y.-F., Soya, M., Shima, T., McEwen, B. S., and Soya, H. (2017). Astrocytic glycogen-derived lactate fuels the brain during exhaustive exercise to maintain endurance capacity. *Proceedings of the National Academy of Sciences of the United States of America*, 114(24):6358–6363.

McConnell, H. L., Kersch, C. N., Woltjer, R. L., and Neuwelt, E. A. (2017). The Translational Significance of the Neurovascular Unit. *Journal of Biological Chemistry*, 292(3):762–770.

McGivney, D. F., Pierre, E., Ma, D., Jiang, Y., Saybasili, H., Gulani, V., and Griswold, M. A. (2014). SVD Compression for Magnetic Resonance Fingerprinting in the Time Domain. *IEEE Transactions on Medical Imaging*, 33(12):2311–2322.

McIntosh, A. R. and Gonzalez-Lima, F. (1994). Structural equation modeling and its application to network analysis in functional brain imaging. *Human Brain Mapping*, 2(1-2):2–22.

Meier, J., Tewarie, P., Hillebrand, A., Douw, L., van Dijk, B. W., Stufflebeam, S. M., and Van Mieghem, P. (2016). A Mapping Between Structural and Functional Brain Networks. *Brain connectivity*, 6(4):298–311.

Mennes, M., Kelly, C., Colcombe, S., Castellanos, F. X., and Milham, M. P. (2013). The Extrinsic and Intrinsic Functional Architectures of the Human Brain Are Not Equivalent. *Cerebral Cortex*, 23(1):223–229.

Mergenthaler, P., Lindauer, U., Dienel, G. A., and Meisel, A. (2013). Sugar for the brain: the role of glucose in physiological and pathological brain function. *Trends in Neurosciences*, 36(10):587–597.

Meunier, D., Lambiotte, R., and Bullmore, E. T. (2010). Modular and Hierarchically Modular Organization of Brain Networks. *Frontiers in Neuroscience*, 4.

Mišić, B. and Sporns, O. (2016). From regions to connections and networks: new bridges between brain and behavior. *Current Opinion in Neurobiology*, 40:1–7.

Moeller, S., Yacoub, E., Olman, C. A., Auerbach, E., Strupp, J., Harel, N.,

and Uurbil, K. (2010). Multiband multislice GE-EPI at 7 tesla, with 16-fold acceleration using partial parallel imaging with application to high spatial and temporal whole-brain fMRI. *Magnetic Resonance in Medicine*, 63(5):1144–1153.

Murphy, K., Birn, R. M., and Bandettini, P. A. (2013). Resting-state fMRI confounds and cleanup. *NeuroImage*, 80:349–359.

Muzic, R. F. and DiFilippo, F. P. (2014). Positron Emission Tomography-Magnetic Resonance Imaging: Technical Review. *Seminars in Roentgenology*, 49(3):242–254.

Newman, M. E. J. (2006). Modularity and community structure in networks.

Nugent, A. C., Martinez, A., D'Alfonso, A., Zarate, C. A., and Theodore, W. H. (2015). The Relationship between Glucose Metabolism, Resting-State fMRI BOLD Signal, and GABA _A -Binding Potential: A Preliminary Study in Healthy Subjects and Those with Temporal Lobe Epilepsy. *Journal of Cerebral Blood Flow & Metabolism*, 35(4):583–591.

Ogawa, S., Lee, T. M., Kay, A. R., and Tank, D. W. (1990). Brain magnetic resonance imaging with contrast dependent on blood oxygenation. *Proceedings of the National Academy of Sciences of the United States of America*, 87(24):9868–72.

Ohliger, M. A. and Sodickson, D. K. (2006). An introduction to coil array design for parallel MRI. *NMR in Biomedicine*, 19(3):300–315.

Ordidge, R. J., Wylezinska, M., Hugg, J. W., Butterworth, E., and Franconi, F. (1996). Frequency offset corrected inversion (FOCI) pulses for use in localized spectroscopy. *Magnetic resonance in medicine*, 36(4):562–6.

Panzeri, S., Macke, J. H., Gross, J., and Kayser, C. (2015). Neural population coding: combining insights from microscopic and mass signals. *Trends in Cognitive Sciences*, 19(3):162–172.

Passow, S., Specht, K., Adamsen, T. C., Biermann, M., Brekke, N., Craven, A. R., Ersland, L., Grüner, R., Kleven-Madsen, N., Kvernenes, O.-H., Schwarzlmüller, T., Olesen, R. A., and Hugdahl, K. (2015). Default-mode network functional connectivity is closely related to metabolic activity. *Human Brain Mapping*, 36(6):2027–2038.

Peraza, L. R., Kaiser, M., Firbank, M., Graziadio, S., Bonanni, L., Onofrj, M., Colloby, S. J., Blamire, A., O'Brien, J., and Taylor, J.-P. (2014). fMRI resting state networks and their association with cognitive fluctuations in dementia with Lewy bodies. *NeuroImage: Clinical*, 4:558–565.

Phelps, M. E. (2004). *PET*. Springer New York, New York, NY.

Power, J. D., Mitra, A., Laumann, T. O., Snyder, A. Z., Schlaggar, B. L., and Petersen, S. E. (2014). Methods to detect, characterize, and remove motion artifact in resting state fMRI. *NeuroImage*, 84:320–341.

Power, J. D., Schlaggar, B. L., Lessov-Schlaggar, C. N., and Petersen, S. E. (2013). Evidence for hubs in human functional brain networks. *Neuron*, 79(4):798–813.

Preti, M. G., Bolton, T. A., and Van De Ville, D. (2017). The dynamic functional connectome: State-of-the-art and perspectives. *NeuroImage*, 160:41–54.

Pruessmann, K. P., Weiger, M., Scheidegger, M. B., and Boesiger, P. (1999). SENSE: sensitivity encoding for fast MRI. *Magnetic resonance in medicine*, 42(5):952–62.

Purcell, E. M., Torrey, H. C., and Pound, R. V. (1946). Resonance Absorption by Nuclear Magnetic Moments in a Solid. *Physical Review*, 69(1-2):37–38.

Raichle, M. E. (2006). Neuroscience. The brain's dark energy. *Science (New York, N.Y.)*, 314(5803):1249–50.

Raichle, M. E. and Gusnard, D. A. (2002). Appraising the brain's energy budget. *Proceedings of the National Academy of Sciences*, 99(16):10237–10239.

Raichle, M. E., MacLeod, A. M., Snyder, A. Z., Powers, W. J., Gusnard, D. A., and Shulman, G. L. (2001). A default mode of brain function. *Proceedings of the National Academy of Sciences of the United States of America*, 98(2):676–82.

Ramsey, J., Hanson, S., Hanson, C., Halchenko, Y., Poldrack, R., and Glymour, C. (2010). Six problems for causal inference from fMRI. *NeuroImage*, 49(2):1545–1558.

Rangaprakash, D., Wu, G.-R., Marinazzo, D., Hu, X., and Deshpande, G. (2018). Hemodynamic response function (HRF) variability confounds resting-state fMRI functional connectivity. *Magnetic Resonance in Medicine*.

Riedl, V., Bienkowska, K., Strobel, C., Tahmasian, M., Grimmer, T., Forster, S., Friston, K. J., Sorg, C., and Drzezga, A. (2014). Local Activity Determines Functional Connectivity in the Resting Human Brain: A Simultaneous FDG-PET/fMRI Study. *Journal of Neuroscience*, 34(18):6260–6266.

Riedl, V., Utz, L., Castrillón, G., Grimmer, T., Rauschecker, J. P., Ploner, M., Friston, K. J., Drzezga, A., and Sorg, C. (2016). Metabolic connectivity mapping reveals effective connectivity in the resting human brain. *Proceedings of the National Academy of Sciences*, 113(2):428–433.

Rieger, B., Akçakaya, M., Pariente, J. C., Llufriu, S., Martinez-Heras, E., Weingärtner, S., and Schad, L. R. (2018). Time efficient whole-brain coverage with MR Fingerprinting using slice-interleaved echo-planar-imaging. *Scientific Reports*, 8(1):6667.

Risk, B. B., Kociuba, M. C., and Rowe, D. B. (2018). Impacts of simultaneous multislice acquisition on sensitivity and specificity in fMRI. *NeuroImage*, 172:538–553.

Rubinov, M. and Sporns, O. (2010). Complex network measures of brain connectivity: Uses and interpretations. *NeuroImage*, 52(3):1059–1069.

Salimi-Khorshidi, G., Douaud, G., Beckmann, C. F., Glasser, M. F., Griffanti, L., and Smith, S. M. (2014). Automatic denoising of functional MRI data: Combining independent component analysis and hierarchical fusion of classifiers. *NeuroImage*, 90:449–468.

Scherr, M., Pasquini, L., Benson, G., Nuttall, R., Gruber, M., Neitzel, J., Brandl, F., and Sorg, C. (2018). Decoupling of Local Metabolic Activity and Functional Connectivity Links to Amyloid in Alzheimer's Disease. *Journal of Alzheimer's Disease*, xx.

Schmitt, P., Griswold, M. A., Jakob, P. M., Kotas, M., Gulani, V., Flentje, M., and Haase, A. (2004). Inversion recovery TrueFISP: Quantification ofT1,T2, and spin density. *Magnetic Resonance in Medicine*, 51(4):661–667.

Setsompop, K., Gagoski, B. A., Polimeni, J. R., Witzel, T., Wedeen, V. J., and Wald, L. L. (2012). Blipped-controlled aliasing in parallel imaging for simultaneous multislice echo planar imaging with reduced g-factor penalty. *Magnetic Resonance in Medicine*, 67(5):1210–1224.

Shah, L. M., Cramer, J. A., Ferguson, M. A., Birn, R. M., and Anderson, J. S. (2016). Reliability and reproducibility of individual differences in functional connectivity acquired during task and resting state. *Brain and Behavior*, 6(5).

Sheffield, J. M. and Barch, D. M. (2016). Cognition and resting-state functional connectivity in schizophrenia. *Neuroscience & Biobehavioral Reviews*, 61:108–120.

Shen, K., Bezgin, G., Hutchison, R. M., Gati, J. S., Menon, R. S., Everling, S., and McIntosh, A. R. (2012). Information Processing Architecture of Functionally Defined Clusters in the Macaque Cortex. *Journal of Neuroscience*, 32(48):17465–17476.

Shinn, M., Romero-Garcia, R., Seidlitz, J., Váša, F., Vértes, P. E., and Bullmore, E. (2017). Versatility of nodal affiliation to communities.

Shulman, R. G., Rothman, D. L., Behar, K. L., and Hyder, F. (2004). Energetic basis of brain activity: implications for neuroimaging. *Trends in*

Neurosciences, 27(8):489–495.

Smith, S. M., Beckmann, C. F., Andersson, J., Auerbach, E. J., Bijsterbosch, J., Douaud, G., Duff, E., Feinberg, D. A., Griffanti, L., Harms, M. P., Kelly, M., Laumann, T., Miller, K. L., Moeller, S., Petersen, S., Power, J., Salimi-Khorshidi, G., Snyder, A. Z., Vu, A. T., Woolrich, M. W., Xu, J., Yacoub, E., Uurbil, K., Van Essen, D. C., and Glasser, M. F. (2013a). Resting-state fMRI in the Human Connectome Project. *NeuroImage*, 80:144–168.

Smith, S. M., Jenkinson, M., Woolrich, M. W., Beckmann, C. F., Behrens, T. E., Johansen-Berg, H., Bannister, P. R., De Luca, M., Drobnjak, I., Flitney, D. E., Niazy, R. K., Saunders, J., Vickers, J., Zhang, Y., De Stefano, N., Brady, J. M., and Matthews, P. M. (2004). Advances in functional and structural MR image analysis and implementation as FSL. *NeuroImage*, 23:S208–S219.

Smith, S. M., Miller, K. L., Salimi-Khorshidi, G., Webster, M., Beckmann, C. F., Nichols, T. E., Ramsey, J. D., and Woolrich, M. W. (2011). Network modelling methods for FMRI. *NeuroImage*, 54(2):875–891.

Smith, S. M., Vidaurre, D., Beckmann, C. F., Glasser, M. F., Jenkinson, M., Miller, K. L., Nichols, T. E., Robinson, E. C., Salimi-Khorshidi, G., Woolrich, M. W., Barch, D. M., Uurbil, K., and Van Essen, D. C. (2013b). Functional connectomics from resting-state fMRI. *Trends in Cognitive Sciences*, 17(12):666–682.

Sokoloff, L. (1999). Energetics of functional activation in neural tissues. *Neurochemical research*, 24(2):321–9.

Sokoloff, L., Reivich, M., Kennedy, C., Des Rosiers, M. H., Patlak, C. S., Pettigrew, K. D., Sakurada, O., and Shinohara, M. (1977a). The [14C]deoxyglucose method for the measurement of local cerebral glucose utilization: theory, procedure, and normal values in the conscious and anesthetized albino rat. *Journal of neurochemistry*, 28(5):897–916.

Sokoloff, L., Reivich, M., Kennedy, C., Des Rosiers, M. H., Patlak, C. S., Pettigrew, K. D., Sakurada, O., and Shinohara, M. (1977b). The [14C]deoxyglucose method for the measurement of local cerebral glucose utilization: theory, procedure, and normal values in the conscious and anesthetized albino rat. *Journal of neurochemistry*, 28(5):897–916.

Song, X.-W., Dong, Z.-Y., Long, X.-Y., Li, S.-F., Zuo, X.-N., Zhu, C.-Z., He, Y., Yan, C.-G., and Zang, Y.-F. (2011). REST: A Toolkit for Resting-State Functional Magnetic Resonance Imaging Data Processing. *PLoS ONE*, 6(9):e25031.

Sporns, O. (2013). Structure and function of complex brain networks. *Dialogues in Clinical Neuroscience*, 15(3):247–262.

Sporns, O. and Betzel, R. F. (2016). Modular Brain Networks. *Annual review of psychology*, 67:613–40.

Sporns, O., Honey, C. J., and Kötter, R. (2007). Identification and Classification of Hubs in Brain Networks. *PLoS ONE*, 2(10):e1049.

Stam, C. J. and Reijneveld, J. C. (2007). Graph theoretical analysis of complex networks in the brain. *Nonlinear biomedical physics*, 1(1):3.

Steketee, R. M. E., Mutsaerts, H. J. M. M., Bron, E. E., van Osch, M. J. P., Majoie, C. B. L. M., van der Lugt, A., Nederveen, A. J., and Smits, M. (2015). Quantitative Functional Arterial Spin Labeling (fASL) MRI–Sensitivity and Reproducibility of Regional CBF Changes Using Pseudo-Continuous ASL Product Sequences. *PloS one*, 10(7):e0132929.

Sun, F. T., Miller, L. M., and D'Esposito, M. (2004). Measuring interregional functional connectivity using coherence and partial coherence analyses of fMRI data. *NeuroImage*, 21(2):647–658.

Supekar, K., Musen, M., and Menon, V. (2009). Development of Large-Scale Functional Brain Networks in Children. *PLoS Biology*, 7(7):e1000157.

Tahmasian, M., Shao, J., Meng, C., Grimmer, T., Diehl-Schmid, J., Yousefi, B. H., Forster, S., Riedl, V., Drzezga, A., and Sorg, C. (2016). Based on the Network Degeneration Hypothesis: Separating Individual Patients with Different Neurodegenerative Syndromes in a Preliminary Hybrid PET/MR Study. *Journal of Nuclear Medicine*, 57(3):410–415.

Thomas Yeo, B. T., Krienen, F. M., Sepulcre, J., Sabuncu, M. R., Lashkari, D., Hollinshead, M., Roffman, J. L., Smoller, J. W., Zollei, L., Polimeni, J. R., Fischl, B., Liu, H., and Buckner, R. L. (2011). The organization of the human cerebral cortex estimated by intrinsic functional connectivity. *Journal of Neurophysiology*, 106(3):1125–1165.

Todd, N., Josephs, O., Zeidman, P., Flandin, G., Moeller, S., and Weiskopf, N. (2017). Functional Sensitivity of 2D Simultaneous Multi-Slice Echo-Planar Imaging: Effects of Acceleration on g-factor and Physiological Noise. *Frontiers in Neuroscience*, 11:158.

Todd, N., Moeller, S., Auerbach, E. J., Yacoub, E., Flandin, G., and Weiskopf, N. (2016). Evaluation of 2D multiband EPI imaging for high-resolution, whole-brain, task-based fMRI studies at 3T: Sensitivity and slice leakage artifacts. *NeuroImage*, 124:32–42.

Tofts, P. (2003). *Quantitative MRI of the brain*. John Wiley and Sons New York.

Tomasi, D., Wang, G.-J., and Volkow, N. D. (2013). Energetic cost of brain functional connectivity. *Proceedings of the National Academy of Sciences*, 110(33):13642–13647.

Triantafyllou, C., Hoge, R., Krueger, G., Wiggins, C., Potthast, A., Wiggins, G., and Wald, L. (2005). Comparison of physiological noise at 1.5 T, 3 T and 7 T and optimization of fMRI acquisition parameters. *NeuroImage*, 26(1):243–250.

Triantafyllou, C., Hoge, R. D., and Wald, L. L. (2006). Effect of spatial smoothing on physiological noise in high-resolution fMRI. *NeuroImage*, 32(2):551–557.

Triantafyllou, C., Polimeni, J. R., and Wald, L. L. (2011). Physiological noise and signal-to-noise ratio in fMRI with multi-channel array coils. *NeuroImage*, 55(2):597–606.

Tsai, Y.-H., Yuan, R., Huang, Y.-C., Yeh, M.-Y., Lin, C.-P., and Biswal, B. B. (2014). Disruption of brain connectivity in acute stroke patients with early impairment in consciousness. *Frontiers in Psychology*, 4.

Turner, R. (2016). Uses, misuses, new uses and fundamental limitations of magnetic resonance imaging in cognitive science. *Philosophical transactions of the Royal Society of London. Series B, Biological sciences*, 371(1705).

Tustison, N. J., Avants, B. B., Cook, P. A., Song, G., Das, S., van Strien, N., Stone, J. R., and Gee, J. C. (2013). The ANTs cortical thickness processing pipeline. page 86720K.

Tustison, N. J., Avants, B. B., Cook, P. A., Zheng, Y., Egan, A., Yushkevich, P. A., Gee, J. C., Yuanjie Zheng, Egan, A., Yushkevich, P. A., and Gee, J. C. (2010). N4ITK: Improved N3 Bias Correction. *IEEE transactions on medical imaging*, 29(6):1310–1320.

Vaishnavi, S. N., Vlassenko, A. G., Rundle, M. M., Snyder, A. Z., Mintun, M. A., and Raichle, M. E. (2010). Regional aerobic glycolysis in the human brain. *Proceedings of the National Academy of Sciences*, 107(41):17757–17762.

Valk, P. E. (2004). Positron Emission Tomography: Basic Science and Clinical Practice. *Radiology*, 232(3):910–910.

van den Heuvel, M., Stam, C., Boersma, M., and Hulshoff Pol, H. (2008). Small-world and scale-free organization of voxel-based resting-state functional connectivity in the human brain. *NeuroImage*, 43(3):528–539.

van den Heuvel, M. P., Mandl, R. C., Kahn, R. S., and Hulshoff Pol, H. E. (2009). Functionally linked resting-state networks reflect the underlying structural connectivity architecture of the human brain. *Human Brain Mapping*, 30(10):3127–3141.

van den Heuvel, M. P. and Sporns, O. (2013a). An anatomical substrate for integration among functional networks in human cortex. *The Journal of neuroscience : the official journal of the Society for Neuroscience*, 33(36):14489–500.

van den Heuvel, M. P. and Sporns, O. (2013b). Network hubs in the human brain. *Trends in Cognitive Sciences*, 17(12):683–696.

van der Kouwe, A. J., Benner, T., Salat, D. H., and Fischl, B. (2008). Brain morphometry with multiecho MPRAGE. *NeuroImage*, 40(2):559–569.

van Wijk, B. C. M., Stam, C. J., and Daffertshofer, A. (2010). Comparing Brain Networks of Different Size and Connectivity Density Using Graph Theory. *PLoS ONE*, 5(10):e13701.

Vidal-Piñeiro, D., Valls-Pedret, C., Fernández-Cabello, S., Arenaza-Urquijo, E. M., Sala-Llonch, R., Solana, E., Bargalló, N., Junqué, C., Ros, E., and Bartrés-Faz, D. (2014). Decreased Default Mode Network connectivity correlates with age-associated structural and cognitive changes. *Frontiers in aging neuroscience*, 6:256.

Vlassenko, A. G. and Mintun, M. A. (2012). *Neural Metabolism In Vivo*, volume 4.

Vlassenko, A. G., Rundle, M. M., and Mintun, M. A. (2006). Human brain glucose metabolism may evolve during activation: Findings from a modified FDG PET paradigm. *NeuroImage*, 33(4):1036–1041.

Wald, L. L. and Polimeni, J. R. (2017). Impacting the effect of fMRI noise through hardware and acquisition choices Implications for controlling false positive rates. *NeuroImage*, 154:15–22.

Walsh, D. O., Gmitro, A. F., and Marcellin, M. W. (2000). Adaptive reconstruction of phased array MR imagery. *Magnetic resonance in medicine*, 43(5):682–90.

Wang, J., He, L., Zheng, H., and Lu, Z.-L. (2014). Optimizing the Magnetization-Prepared Rapid Gradient-Echo (MP-RAGE) Sequence. *PLoS ONE*, 9(5):e96899.

Wang, J., Zuo, X., and He, Y. (2010). Graph-based network analysis of resting-state functional MRI. *Frontiers in Systems Neuroscience*, 4:16.

Watts, D. J. and Strogatz, S. H. (1998). Collective dynamics of small-world' networks. *Nature*, 393(6684):440–442.

Wehrl, H. F., Hossain, M., Lankes, K., Liu, C.-C., Bezrukov, I., Martirosian, P., Schick, F., Reischl, G., and Pichler, B. J. (2013). Simultaneous PET-MRI reveals brain function in activated and resting state on metabolic, hemodynamic and multiple temporal scales. *Nature Medicine*, 19(9):1184–1189.

Weigel, M. (2015). Extended phase graphs: Dephasing, RF pulses, and echoes - Pure and simple. *Journal of Magnetic Resonance Imaging*, 41(2):266–295.

Whitfield-Gabrieli, S., Thermenos, H. W., Milanovic, S., Tsuang, M. T., Faraone, S. V., McCarley, R. W., Shenton, M. E., Green, A. I., Nieto-

Castanon, A., LaViolette, P., Wojcik, J., Gabrieli, J. D. E., and Seidman, L. J. (2009). Hyperactivity and hyperconnectivity of the default network in schizophrenia and in first-degree relatives of persons with schizophrenia. *Proceedings of the National Academy of Sciences*, 106(4):1279–1284.

Woodward, N. D. and Cascio, C. J. (2015). Resting-State Functional Connectivity in Psychiatric Disorders. *JAMA Psychiatry*, 72(8):743.

Xu, J., Moeller, S., Auerbach, E. J., Strupp, J., Smith, S. M., Feinberg, D. A., Yacoub, E., and Uurbil, K. (2013). Evaluation of slice accelerations using multiband echo planar imaging at 3T. *NeuroImage*, 83:991–1001.

Yu, Z. and Cloos, M. A. (2017). Exploring the sensitivity of magnetic resonance fingerprinting to different types of motion and possible correction mechanisms. In *ISMRM 2017*.

Zalesky, A., Fornito, A., and Bullmore, E. T. (2010). Network-based statistic: Identifying differences in brain networks. *NeuroImage*, 53(4):1197–1207.

Zhou, D., Thompson, W. K., and Siegle, G. (2009). MATLAB toolbox for functional connectivity. *NeuroImage*, 47(4):1590–1607.

Zhu, J., Zhuo, C., Xu, L., Liu, F., Qin, W., and Yu, C. (2017). Altered Coupling between Resting-State Cerebral Blood Flow and Functional Connectivity in Schizophrenia. *Schizophrenia Bulletin*, 43(6):1363–1374.

Zuo, X.-N., Ehmke, R., Mennes, M., Imperati, D., Castellanos, F. X., Sporns, O., and Milham, M. P. (2012). Network Centrality in the Human Functional Connectome. *Cerebral Cortex*, 22(8):1862–1875.

Acknowledgments

During my PhD I had the privilege to work with many inspiring and strongly committed people, I'd like to thank them all for all the direct or indirect support. Without their contribution this thesis wouldn't even have a title.

Above all, I'm grateful to my advisor Prof. Alessandra Bertoldo for teaching me "how to research" as well as for the continuous support during these intense years.

Thanks also to Prof. Maurizio Corbetta for the support and many interesting discussion we had together.

A special thanks to my families, not only the home one which always supported me for the best but also the work one where the support of Agnese, Erica, Ilaria, Marco, Marta among many others was possibly the only reason why I've finished my studies.

A special thank also to Prof. Riccardo Lattanzi, Martijn Cloos and Zidan Yu, the work we have done in NY brought me so much more but I survived there thanks also to Ioannis, Jing and Paula.

Thanks to everyone else contributed to this thesis.

Padova, September 2018.